Title
LNA and Mixer Designs for Multi-Band Receiver Front-Ends

Author
Poobuapheun, Nuntachai

Publication Date
2009

Peer reviewed|Thesis/dissertation

LNA and Mixer Designs for Multi-Band Receiver Front-Ends

By

Nuntachai Poobuapheun

B.Eng. (Chulalongkorn University, Thailand) 2002
M.S. (University of California, Berkeley) 2005

A dissertation submitted in partial satisfaction of the

requirements for the degree of

Doctor of Philosophy

in

Engineering – Electrical Engineering and Computer Sciences

in the

Graduate Division

of the

University of California, Berkeley

Committee in charge:

Professor Ali M. Niknejad, Chair
Professor Robert G. Meyer
Professor Philip B. Stark

Fall 2009

LNA and Mixer Designs for Multi-Band Receiver Front-Ends

By

Nuntachai Poobuapheun

Abstract

LNA and Mixer Designs for Multi-Band Receiver Front-Ends

by

Nuntachai Poobuapheun

Doctor of Philosophy in Engineering – Electrical Engineering and Computer Sciences

University of California, Berkeley

Professor Ali Niknejad, Chair

With the proliferation of wireless standards and frequency bands, the manufacturers of consumer electronics have tried to integrate many features in a single hand-held device. This has given rise to a need for receivers that are compatible with as many standards and frequency bands as possible. Most current integrated multi-band receivers rely on multiple receiver front-ends to process signals at different bands. The major drawback of this approach is that each front-end must be individually optimized, resulting in longer design-time and higher silicon die areas. This is due to the number of circuit blocks and interface complexity. In addition, this type of implementation is highly standard-specific: thus, it is likely that a major redesign would be required if the same topology were used for different standards.

The primary objective of this research is to investigate efficient ways of implementing such a receiver front-end with minimal cost, power consumption, and design complexity. CMOS will be the targeted process technology for this design, due to the opportunities for analog-digital system integration and cost-reduction. Despite its attractiveness, designing a front-end for multi-band operations in deep-submicron

CMOS technology is non-trivial. The main challenge lies in maintaining moderate gain, noise figure, and linearity at minimum current consumption across a wide frequency spectrum with the abating supply voltage.

In this work, we investigate and discuss several receiver front-end building blocks and system designs, with a focus on the issues that arise when designing a multi-band receiver front-end. In addition, we propose several circuit building blocks and systems, and implement design prototypes to validate the possibilities. The results suggest that by exploiting high-speed CMOS transistors and innovative low-voltage design techniques, it is possible to design a low-voltage, low-power, wideband receiver front-end path that is capable of processing signals using the proposed architectures.

_____

Professor Ali M Niknejad, Chair Date

Acknowledgements

I would like to express my sincere gratitude to my advisor, Professor Ali M. Niknejad, without whom this work would not have been possible. His vast knowledge of several subjects enabled me to be able to advance my work during the years we worked together. Also, he was always supportive of all phases of my work, from the beginning to the end.

I would like to thank Professor Robert G. Meyer, Professor Seth Sanders, and Professor Philip Stark for valuable guidance during the qualifying exam. I also would like to express further gratitude to Professor Meyer and Professor Stark for agreeing to be on the dissertation committee and for providing numerous reviews of and suggestions for my work.

I would like to thank Wei-Hung Chen and Zhimming Deng, my great friends and colleagues, for their time and help with my research during my years at UC Berkeley. I also would like to think Tim Wongkomet, Yuen-Hui Chee, and Stanly Wang for their valuable input into the project and qualifying exam preparation. I would like to thank Ashkan Borna for his time reviewing the dissertation draft. I also would like to thank my all colleagues at BWRC for their supports during the years.

I would like to acknowledge the help of Zdravko Boos for his valuable input and help with the project. Even though we only met once, I have learned many things from our phone conference meetings and discussions, many of which provided me with direction for my work. I also would like to thank Infineon Technologies and IBM for chip fabrications for my research, and all BWRC industrial members for their support

and assistance. I especially thank Joel Dunsmore from Agilent Technologies for this time and suggestions for several measurement setups and procedures.

My years at Berkeley not have been as enjoyable without all my friends outside the Department or the University. I would like to thank all the members of the Thai student group for their support, and countless enjoyable moments throughout the years. Also, I have been lucky to have wonderful roommates, Thaisiri Watewai, Pichaya Viwatrujirapong, and Chayut Thanapirom, during my stay at Berkeley.

I would like to thank all my teachers and advisors in Thailand, from my elementary school to college, who gave me such good foundations through giving me knowledge and experience. My project with Professor Wanchalerm Pora brought about my interest in wireless communications, and my courses with Professor Naiyavudhi Wongkoment inspired me to pursue a career in IC design.

My greatest appreciation and my heart go to my wife, Suvimol Ming Sangkatumvong, whom I respect greatly for her love and supports. She has always stood by me in both bad and good times throughout the years, and never questioned my abilities.

Most importantly, I would like to thank my family for their support and their unconditional love. My only brother, Saran, always believes in me and takes care of my parents when I am away from home. My parents, Udom and Chalao Poobuapheun, had to endure many challenges in order for me come to the United States for my graduate studies. My father always supports me and is always there when I need help. My mother always reminds me about the importance of responsibility and integrity, both of which I will always remember.

Dedicated to my parents

Table of Contents

1

Introduction

1.1 CMOS Technology and Wireless Systems

Until the late 1980s, radios were implemented using discrete components such as transistors, capacitors, and inductors. The transistors used in these radios were manufactured using expensive process technologies that were optimized for high-frequency applications [1.1]. As sales of wireless communication handsets have risen, the wireless transceiver market has become increasingly attractive to electronics hardware vendors. This has led to a highly competitive consumer market space, with tremendous pressures in the industry for lowest-cost solutions.

In the early 1990s, the adoption of standards such as GSM, and advances in digital signal processing increased the demand for digital circuits in radio systems. CMOS has been the technology of choice for implementing digital signal processors, since CMOS devices consume less power than competing technologies. This has spurred research efforts to reduce the cost of CMOS transistors and implementations. Given sufficient production volume, the cost of a CMOS chip decreases as the size of a unit transistor decreases, because the same functionality can be provided in a smaller silicon die area. In 1965, Gordon Moore predicted that the number of transistors that could be put in a given space would double approximately every two years [1.2]. His

prediction has proved true: transistor unit size has decreased exponentially for decades [1.3].

As CMOS transistor size shrinks, device parasitic capacitances also become smaller, and the transistor becomes faster [1.4]. Eventually, CMOS transistors become sufficiently fast to be used in radio frequency integrated circuit implementations. From that point, CMOS provides the highest analog-digital on-chip integration and yields the lowest-cost solutions for implementing wireless transceivers. For these reasons, much research on CMOS wireless transceivers has been published, describing increasing levels of digital and analog integration [1.5][1.6][1.7]. Although competing technologies exist, the cost benefits of mixed-signal CMOS technology make it the process of choice for transceivers used in high-volume applications.

1.2 Need for Multi-Standard Receivers

The limited available frequency spectrums have become overcrowded as wireless network deployments have proliferated. This crowding has stimulated research efforts to increase spectral efficiency through better modulation schemes or advanced system-level techniques (e.g., power control in CDMA systems). In the last 20 years, several new standards have been proposed and implemented; Table 1.1 shows the wireless standards currently in use [1.8]. From the table, it is clear that each standard specifies its own frequency band, modulation scheme, signal power, and data rates. The differences in the defined standards translate into different requirements for receiver front-ends – when a new standard is created, a new receiver front-end must be designed, which is time-consuming. One approach to reducing the system design time is to

optimize an existing receiver front-end for a different application. However, this methodology results in inferior performance.

Range	**Long**		**Medium**	**Short**	
System	GSM/DCS	UMTS	802.11a	Bluetooth	DECT
Frequency	0.9/1.8GHz	2GHz	5GHz	2.4GHz	1.9GHz
Channel spacing	200KHz	5MHz	20MHz	1MHz	1.728MHz
Access	TDMA	CDMA	CSMA/CA	CDMA	TDMA
Modulation	GMSK	QPSK	BPSK/QPSK/QAM	GFSK	GFSK
Bit rate	270K	3.84M	5.5~54M	1M	1.152M
Rx sensitivity	-100dBm	-117dBm	-65dBm	-70dBm	-83dBm
Signal S/N+I	9dB	5.2dB	28dB	21dB	10.3dB
Rx NF	9dB	9dB	7.5dB	23dB	18dB
Rx IIP_3	-18dBm	-4dBm	-20dBm	-15dBm	-22dBm
Phase noise	-141dBc@3M	-150dBc@135M	-102dBc@1M	-105dBc@1M	-99dBc@2.2M
Frequency	0.9/1.8GHz	2GHz	5GHz	2.4GHz	1.9GHz

Table 1.1 Comparison of wireless standards (table from [1.8])

Over the past decade, consumer electronics manufacturers have tried to integrate many features in a single hand-held device (e.g., multi-band multi-standards compatibility). This has given rise to a need for receivers that are compatible with as many standards and frequency bands as possible. Most current multi-band receivers rely on multiple receiver front-ends to process signals at different bands [1.6][1.9]. The major drawback of this approach is that each front-end must be individually optimized, resulting in longer design and simulation times, due to the number of circuit blocks, and

interface complexity. In addition, this approach can require very large front-end silicon die areas, especially if inductors are used in each receiving path. Finally, this type of implementation is highly standard-specific; thus, a major redesign would likely be required if the same topology were used for different standards – when, for example, there is an immediate need for a front-end that is compatible with the system, but with different requirements from previous front-ends.

1.3 Research Goals and Contributions

As indicated in the previous section, there is strong motivation to design a multi-band or wideband receiver front-end that is compatible with multiple standards. The primary objective of this research is to investigate efficient ways to implement such a receiver front-end with minimal cost, power consumption, and design complexity. In addition, for the reasons discussed in section 1.1, CMOS will be the targeted process technology for the design, due to the opportunities for system integration and cost-reduction.

The contributions of this research include the investigation and discussion of several building blocks and system designs, including an analysis of issues in designing a multi-band receiver front-end, and a comparison of various receiver building blocks and system architectures. In addition, we will propose several circuit building blocks and systems, and implement design prototypes to validate the possibilities. The results suggest that by exploiting high-speed CMOS transistors and innovative low-voltage design techniques it is possible to design a low-voltage, low-power, wideband receiver front-end path that is capable of processing signals using the proposed architectures.

1.4 Thesis Organization

This thesis is organized as follows: Chapter 2 offers a review of receiver fundamentals, including receiver sensitivity, receiver selectivity, and basic receiver architectures. Also provided are discussions of the universal multi-band receiver front-end in terms of specifications, limitations, and suitable topologies.

Chapter 3 reviews the fundamentals of CMOS low-noise amplifiers (LNA), including topics ranging from noise sources in MOS transistors to basic CMOS LNA design. Chapter 4 presents the analysis, design, and experimental results of a broadband LNA in a 0.18 μm CMOS process. Chapter 5 reviews mixer fundamentals, with emphasis on CMOS mixers, and covers mixer operations, mixer performance metrics, basic CMOS mixer architectures. Chapter 6 presents analysis, design, and implementation results of a wideband demodulator implemented in a 0.13 μm CMOS technology.

Chapter 7 presents a design for a wideband front-end for a multi-band receiver in 0.13μm CMOS technology, and implementation results.

Chapter 8 presents conclusions and future research possibilities.

1.5 References

[1.1] A. Abidi, "CMOS wireless transceivers: the new wave," *IEEE Communications Magazine*, vol. 37, no. 8, pp. 119-122, Aug. 1999.

[1.2] Moore, Gordon E., "Cramming more components onto integrated circuits," *Electronics*, Volume 38, Number 8, April 19, 1965.

[1.3] J. Rabaey, A. Chandrakasan, and B. Nikolic´. *Digital Integrated Circuits: A Design Perspective*, Second Edition, Prentice-Hall, New Jersey, 2002.

[1.4] P. R. Gray, R.G. Meyer, P. J. Hurst and S. H. Lewis, *Analysis and Design of Analog Integrated Circuits,* Fourth Edition, Wiley, New York, 2001.

[1.5] J. C. Rudell, J. Ou, T. B. Cho, G. Chien, F. Brainti, J. A. Weldon, and P. R. Gray, "A 1.9-GHz wide-band IF double conversion CMOS receiver for cordless telephone applications," *IEEE J. Solid-State Circuits*, vol. 32, no. 12, pp. 2071-2088, Dec. 1997.

[1.6] O. E. Erdogan, et al., "A Single-Chip Quad-Band GSM/GPRS Transceiver in 0.18 μm Standard CMOS," in *IEEE Int. Solid-State Circuits Conf. Dig. Tech. Papers*, San Francisco, CA, Feb. 2005, pp. 318-319.

[1.7] S.S. Mehta, et al., "An 802.11g WLAN SoC," *IEEE J. Solid-State Circuits*, vol. 40, no. 12, pp. 2483-2491, Dec. 2005.

[1.8] W. Chen, N. Poobuapheun, and A. Niknejad, "A Broadband High Dynamic Range CMOS Front-End," BWRC Summer Retreat, 2006.

[1.9] T. Manku, et al., "A single chip direct conversion CMOS transceiver for quad-band GSM/GPRS/EDGE and WLAN with integrated VCO's and fractional-N synthesizer," in Proc. *IEEE Radio Frequency Integrated Circuits (RFIC) Symp.*, Jun. 2004, pp. 423-426.

2

Wireless Receiver Basics

2.1 Introduction

This chapter covers two important receiver concepts: selectivity and sensitivity. These parameters are the most comprehensive figures of merit in receiver performance and are influenced by many sub-figures of merit, such as noise performance of the individual building blocks, linearity, gain distribution, and image rejection ratio. The relationships between these sub-figures of merit and selectivity and sensitivity are discussed in sections 2.2, 2.3, and 2.4.

Section 2.5 offers a review of basic receiver architectures characterized by various frequency planning methodologies, including super-heterodyne, zero-IF (direct conversion), and low-IF receivers. Comparisons between several receiver architectures for multi-band receivers are given in section 2.6, along with a discussion on the requirements and estimated performance of a broadband front-end.

2.2 Sensitivity

Sensitivity is defined as the minimum signal level at the receiver input such that there is a sufficient signal-to-noise ratio (SNR) at the receiver output for a given application. It can be specified in units of dBm (decibels relative to one milliwatt), along with reference impedance (50 Ω for most systems), and is typically measured in an

interference-free environment. Usually, the input of the receiver is matched to a certain source impedance, simplified as the real impedance $R_{in} = R_s$, as shown in figure 2.1.

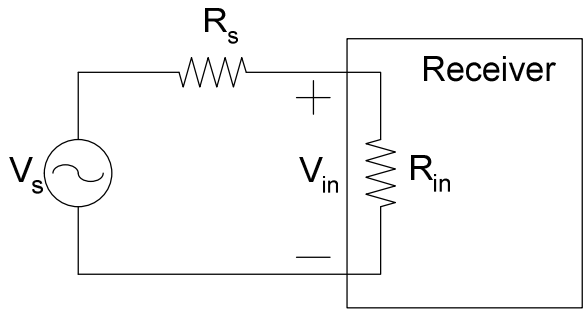

Figure 2.1 Impedance matching in a receiver

2.2.1 Noise Figure Definitions

The overall sensitivity is directly related to the noise figure of the receiver, which is impacted by noise from individual blocks in the receiver as well as the gain distribution of the receiver chain. The noise figure is defined as a ratio between the SNR at the input and the SNR at the output of the circuit:

$$F \equiv \frac{Input\ SNR}{Output\ SNR} \tag{2.1}$$

$$NF \equiv 10\log(F)\ \ (\mathrm{dB}) \tag{2.2}$$

where F is noise factor and NF is the noise figure of the system. Noise figure is calculated in reference to the specified source impedance and the temperature (T). In standard communication systems, the typical values are $R_s = 50\ \Omega$ and $T = 293$ K. For a

circuit building block such as an amplifier, the total noise figure can be calculated in terms of added output noise and the gain of the system. An amplifier with power gain G, input signal power P_{in}, and input noise power N_{in} will have the output signal power GP_{in} and the output noise power $GN_{in}+N_{add}$. The noise figure of the amplifier can then be calculated using the definitions in (2.1).

$$F = \frac{\left(P_{in}/N_{in}\right)}{\frac{GP_{in}}{GN_{in}+N_{add}}} \tag{2.3}$$

$$F = 1 + \frac{N_{add}}{GN_{in}} = 1 + \frac{N_{add,in}}{N_{in}} \tag{2.4}$$

where $N_{add,in}$ is the input-referred added noise from the amplifier, defined as $N_{add,in} = N_{add}/G$.

2.2.2 Noise Figure Calculations for Cascaded Blocks

The previous section discussed the definition of the noise figure for a single circuit block. However, for a receiver, we need to calculate the noise figure of cascaded circuit blocks in order to determine the overall system sensitivity. The cascaded noise figure depends strongly on the noise figures of individual blocks, as well as the gain distribution of the receiver chain. If two blocks are cascaded with each other, as shown in figure 2.2, and the impedance matching is done properly (input and output are matched), the total output noise is then given by:

$$P_{noise,out} = F_1 P_{noise,in} G_1 G_2 + \left(F_2 - 1\right) P_{noise,in} G_2 \tag{2.5}$$

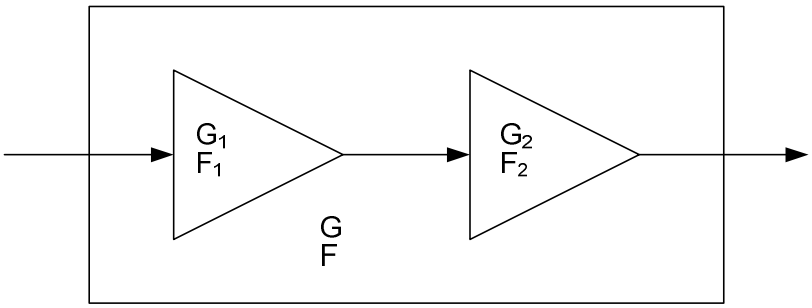

Figure 2.2 Cascaded blocks

G_1 and G_2 are the power gains for each block in the given matching condition. F_1 and F_2 are the noise figures for each block. The output SNR of the cascaded blocks is then given by:

$$SNR_{out} = \frac{S_{out}}{P_{noise,out}} = \frac{S_{in}G_1G_2}{F_1P_{noise,in}G_1G_2 + (F_2 - 1)P_{noise,in}G_2} = SNR_{in}\left(\frac{1}{F_1 + \frac{F_2 - 1}{G_1}}\right) \quad (2.6)$$

Finally, the total cascaded noise figure can be calculated as:

$$F = \frac{SNR_{in}}{SNR_{out}} = F_1 + \frac{(F_2 - 1)}{G_1} \quad (2.7)$$

From (2.7), the overall noise figure depends on the noise figures of both stages and on the gain of the first stage. If G_1 is large, noise from the later stage will have less effect on the overall noise figure. As a result, the first block in the receiver must exhibit low noise and must have at least moderate gain. An amplifier with those characteristics is usually called a low-noise amplifier.

2.2.3 Relationship between Noise Figure and Sensitivity

A direct relationship exists between the noise figure of the amplifier and the sensitivity of the receiver. Sensitivity can be calculated in terms of noise floor and the required SNR at the input. Since the required SNR at the output of the receiver is set by top-level specifications such as modulation techniques and bit-error-rate (BER), it is usually fixed for a given application. These numbers determine carrier-to-noise ratio (CNR), which is the ratio between the carrier power and the integrated noise power in the frequency band. Once the CNR is known, the required receiver input SNR can be calculated as:

$$SNR_{in}(dB) = CNR_{out}(dB) + NF(dB) \tag{2.8}$$

Finally, the expression for the sensitivity is given by:

$$Sensitivity(dBm) = SNR_{in}(dB) + NoiseFloor(dBm) + 10\log(BW)\ (dB) \tag{2.9}$$

where BW is the bandwidth of the communication channel.

2.3 Selectivity

In the last section, we discussed receiver performance, measured by sensitivity to the desired signal. We did not consider interference from other undesired signals. Receiver selectivity is a performance measure of the ability to separate the desired signal from these unwanted interfering signals. It usually becomes important in the

near-far situation where the desired signal is weak and there is a strong adjacent-band/channel interfering signal at the receiver input.

There is no clear quantitative measure of selectivity, especially at the circuit level. It is usually specified in the physical layer, such as in blocking masks, which can be used to obtain the filtering, nonlinearity, and phase noise requirements in the circuit. The other test related to selectivity of the receiver is the third-order intermodulation or two-tone test. In this case, a pair of undesired signals is applied to the receiver in such a way that their third-order intermodulation will line up in the same band as the desired signal. We will discuss these specifications and tests in detail in the next sections.

2.3.1 Blocking Performance

Blocking performance is usually specified with a desired signal being applied to the receiver at a specified power level above the required sensitivity. Simultaneously, an additional signal, called a blocker (sometimes called a jammer) is applied to the receiver at a defined power level and offset from the carrier. Under these conditions, the receiver must maintain the required bit error rate (BER) in the presence of the blocking signal.

A strong blocker can degrade receiver performance in several ways. First, it can cause gain compression, as well as degradation of the noise figure of the receiver. This directly reduces the sensitivity of the receiver for the desired signal [2.1]. The second problem comes from the nonlinearity of the system. When the large blocker goes through second-order nonlinearity in the receiver chain, it can mix with itself down to a very low frequency and so create problems, especially in direct-conversion or low-IF receivers. A detailed analysis of nonlinearity will be given in the next section. Finally,

the strong blocker can mix with the local oscillator sidebands resulting from its phase noise, a process known as reciprocal mixing. The mixed signal can be in the same frequency band as the desired signal, effectively decreasing the signal-to-noise ratio. More details about the reciprocal mixing can be found in [2.2].

An example of the blocking definition is shown in figure 2.3 for the GSM 900 standard [2.3]. The blocking test is performed by applying a Gaussian Minimum-Shift Keying (GMSK) modulated signal at 3 dB above the required sensitivity, along with the single-tone blocker at the input of the receiver. The blockers are located at increments of 200 kHz away from the desired signal, with the amplitudes shown in figure 2.3. To pass the test, the receiver must maintain the bit-error–rate within a defined limit.

There are two types of blockers: in-band and out-of-band. Usually, the band-selecting filter in front of the receiver will filter out the out-of-band blockers. As a result, those blockers will be highly attenuated before arriving at the real receiver input. However, this is not the case for in-band blockers, where all the signals are in the passband of the filter.

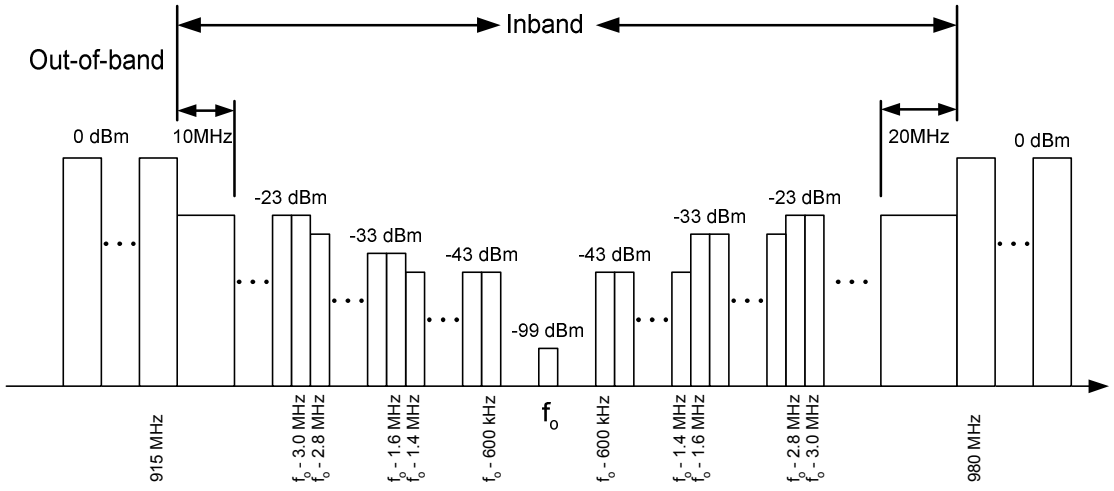

Figure 2.3 GSM 900 blocking definition

2.3.2 Second-Order Nonlinearity

Second-order nonlinearity in the receiver blocks causes many problems, especially in direct-conversion or low-IF receivers. This can be understood by examining an expression that relates the input and output signals of the block. First, assuming we have a relationship given by:

$$S_{out}(t) = a_1 S_{in}(t) + a_2 S_{in}^2(t) + a_3 S_{in}^3(t) + \ldots \tag{2.10}$$

where $S_{in}(t)$ is the input signal and $S_{out}(t)$ is the output signal. If the input signal (the blocker) is a sine wave, we then have:

$$S_i(t) = S_i \cos(\omega_b t) \tag{2.11}$$

where ω_b is the frequency of the blocker. Applying (2.11) to (2.10), the output term created by the second-order nonlinearity is given by:

$$S_{out}(t) = a_2 (S_i \cos(\omega_b t))^2 = a_2 S_i^2 \left(\frac{1}{2} + \frac{\cos(2\omega_b t)}{2} \right) \tag{2.12}$$

There are two components on the right-hand side of (2.12), one located at DC and the other at the frequency of $2\omega_b$. The DC component can superimpose onto the baseband signal at DC and degrade the receiver performance. This becomes problematic in direct conversion receivers with the presence of a strong blocking signal.

Defining second-order harmonic distortion and second-order intermodulation as in [2.4], the expressions for HD_2 and IM_2 are given by:

$$HD_2 = \frac{\frac{a_2}{2} S_i^2}{a_1 S_i} = \frac{1}{2} \frac{a_2}{a_1} S_i \tag{2.13}$$

$$IM_2 \cong HD_2 + 6dB \tag{2.14}$$

Since IM2 increases linearly with input signal level, there will be a point where the extrapolated IM2 is equal to the extrapolated first-order output signal (figure 2.4). The second-order input intercept point (IIP_2) is an important figure of merit in receiver designs and is given by:

$$IIP_2 = \frac{a_1}{a_2} \tag{2.15}$$

Given the IIP_2, one can calculate the output IM_2 for a given input blocker power by the equation:

$$IM_2(dB) = P_{blocker}(dB) - IIP_2(dB) \tag{2.16}$$

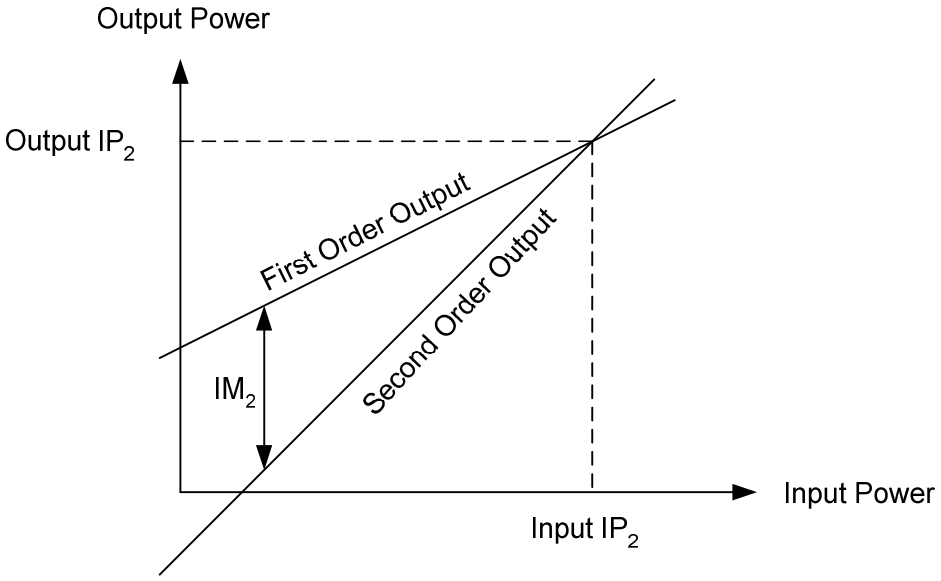

Figure 2.4 IM_2 plot and IIP_2 intercept point

2.3.4 Third-Order Nonlinearity

Another important type of nonlinearity in receiver systems is third-order nonlinearity. Problems associated with third-order nonlinearity arise from two out-of-channel signals passing though the nonlinear blocks. Assuming that these two signals are sinusoidal, we can write them in combination as an input signal:

$$S_i(t) = S_1 \cos(\omega_1 t) + S_2 \cos(\omega_2 t) \tag{2.17}$$

After $S_i(t)$ passes through the third-order nonlinearity term in (2.10), several unwanted frequencies are generated. After simplification, we get:

$$a_3 S_i^3 = \frac{a_3 S_1^3}{4}\left(\cos(3\omega_1 t) + 3\cos(\omega_1 t)\right) + \frac{a_3 S_2^3}{4}\left(\cos(3\omega_2 t) + 3\cos(\omega_2 t)\right) + \frac{3}{4} a_3 S_1 S_2^2 \left[2\cos(\omega_1 t) + \cos\left((2\omega_2 - \omega_1)t\right) + \cos\left((2\omega_2 + \omega_1)t\right)\right] + \frac{3}{4} a_3 S_1^2 S_2 \left[2\cos(\omega_2 t) + \cos\left((2\omega_1 - \omega_2)t\right) + \cos\left((2\omega_1 + \omega_2)t\right)\right] \quad (2.18)$$

The graphical presentation of (2.18) is shown in figure 2.5. There are linear terms (ω_1, ω_2), third-order harmonics ($3\omega_1$ and $3\omega_2$), and third-order intermodulation terms ($2\omega_2$-ω_1, $2\omega_1$-ω_2, $2\omega_2$+ω_1, $2\omega_1$+ω_2).

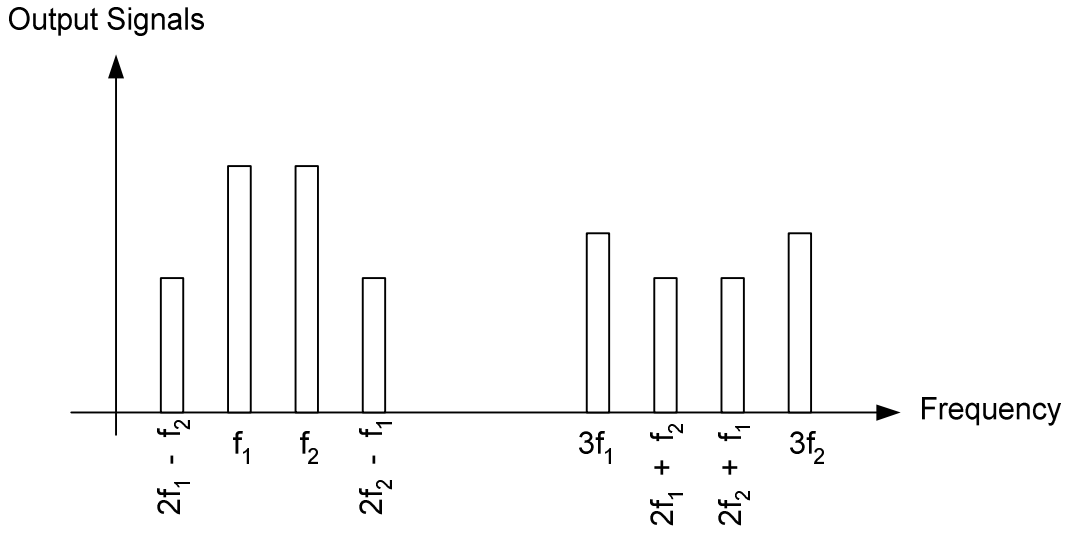

Figure 2.5 Third–order products in frequency domain

If the two-tones are placed adjacent to each other, some of the IM_3 products will lie just next to ω_1 and ω_2. If the desired channel is located at either $2\omega_2$-ω_1 or $2\omega_1$-ω_2, it will experience interference due to these components. This is often the most troubling case for receiver applications where there might be alternate channel users present very close in frequency to the receiver's desired channel.

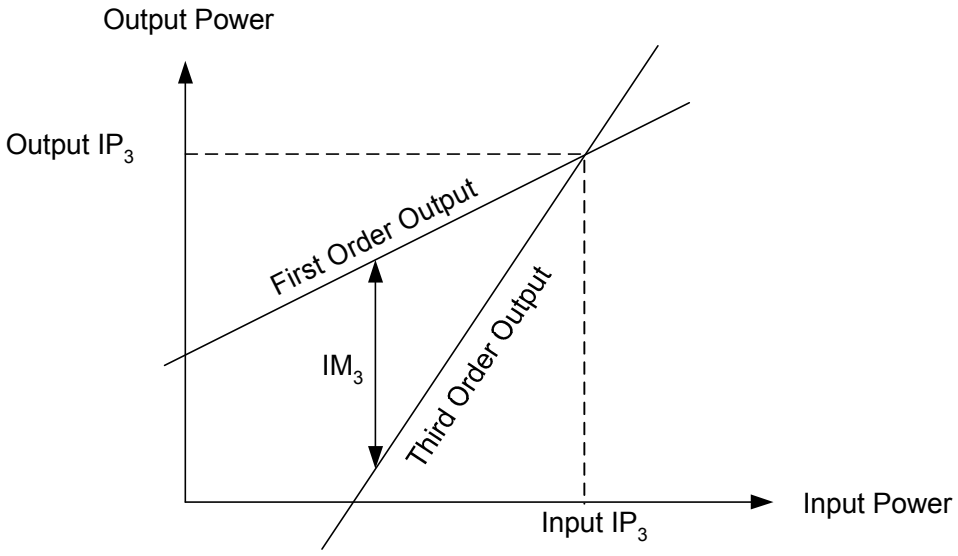

Figure 2.6 Third-order intercept points

Figure 2.6 shows the logarithmic plot between the output and input signals assuming the same power of the two-tones. The third-order intermodulation grows with the input power at three times the rate at which the linear components increase. The third-order intercept point (IP_3) is defined as the intersection of the two lines. The horizontal coordinate of this point is called the input IP_3 (IIP_3), and the vertical coordinate is called the output IP_3 (OIP_3). The IIP_3 can be calculated by equating the linear term and the IM_3 term and is given by:

$$IIP_3 = \sqrt{\frac{4}{3}\left|\frac{a_1}{a_3}\right|} \tag{2.19}$$

Alternately, if the IIP_3 and the power of corresponding two-tone signals are given, the input referred IM_3 can be expressed as (all units are in dB):

$$IM_{3,in} = 2\left(P_{in} - IIP_3\right) \tag{2.20}$$

For cascaded nonlinear stages such as the one in figure 2.2, the overall IIP_3 is affected by the nonlinearity of each block and gain distribution. As shown in [2.5], the overall IIP_3 is given (neglecting second-order interaction) by:

$$\frac{1}{IIP_{3,overall}^2} \approx \frac{1}{IIP_{3,1}^2} + \frac{G_1^2}{IIP_{3,2}^2} + \frac{G_1^2 G_2^2}{IIP_{3,3}^2} + \ldots \tag{2.21}$$

where $IIP_{3,k}$ and G_k are the voltage IIP_3 and voltage gain for the block k. If one block dominates the overall third-order nonlinearity of the system, the IIP_3 can be estimated as [2.6]:

$$IIP_{3,overall} \approx \min\left[IIP_{3,1}, \left(\frac{IIP_{3,2}}{G_1}\right), \left(\frac{IIP_{3,3}}{G_1 G_2}\right), \ldots\right] \tag{2.22}$$

2.4 Receiver Dynamic Range

The dynamic Range (DR) of a receiver is defined as the ratio of the maximum input level that the circuit can tolerate, to the minimum input level that is still detectable. The quantitative definitions differ from application to application. In analog circuits such as A/D converters, it can be defined as a ratio between the "full-scale" (FS) input level and the input level for which SNR=1. In RF receivers, however, it is very hard to define FS input level. The commonly used method is to define the upper limit of the input power as the maximum two-tone input level at which the produced output IM_3 is

still below the noise floor. Such a definition is called the "spurious-free dynamic range" (SFDR) [2.5].

By rewriting (2.20), we have:

$$P_{in} = \frac{2IIP_3 + IM_{3,in}}{2} \tag{2.23}$$

The integrated noise floor over the bandwidth (N_{in}) at the input of a receiver is given by:

$$N_{in}(dBm) = NoiseFloor(dBm) + 10\log(BW)(\text{dB}) \tag{2.24}$$

The *input referred* integrated noise floor at the *output* of the receiver is then given by:

$$N_{out,in}(dBm) = N_{in}(dBm) + NF(dB) \tag{2.25}$$

The input referred third-order intermodulation product must be equal or less than $N_{out,in}$. This gives us:

$$P_{in,\max} = \frac{2IIP_3 + N_{out,in}}{2} \tag{2.26}$$

Since the lower bound of the input power is the sensitivity or minimum detectable signal (MDS) of the receiver, the spurious-free dynamic range is:

$$DR = P_{in,\max} - Sensitivity \tag{2.27}$$

2.5 Receiver Architecture Reviews

The previous sections presented the basic requirements of receiver functionalities and figures of merit. We now move our focus to methods for designing receiver systems that meet both selectivity and sensitivity requirements. This section will review the two most popular receiver architectures, heterodyne receivers and homodyne receivers. The contents of this section follow the reviews in [2.7].

2.5.1 Heterodyne Receiver

The heterodyne architecture has been used in wireless receivers for almost a century and provides superior sensitivity and selectivity compared to other architectures [2.8]. The basic block diagram of the receiver is shown in figure 2.7. Immediately after the antenna, there is an RF bandpass filter, used to filter out-of-band signals, followed by a low-noise amplifier (LNA), an image-reject filter, an RF mixer, a channel select filter, an IF mixer, and finally a low-pass filter and baseband processor.

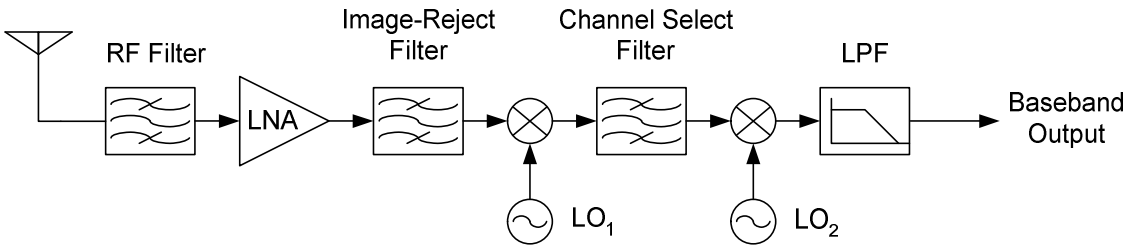

Figure 2.7 Heterodyne receiver architecture

The main concept of this architecture is that the frequency translation process is divided into two steps. The first is the transition of a signal from radio-frequency (RF) to the intermediate frequency (IF). The second is the frequency translation from IF to baseband. The channel filtering takes place at the IF frequency by a bandpass filter with *fixed* center frequency at the IF. This means that the channel selection takes place at the first mixing process by selecting the local oscillator (LO) frequency, such that the RF signal is shifted down by different amounts to locate the desired channel at the fixed IF. Performing channel filtering at the fixed IF frequency greatly relaxes the requirements on the channel-select filter. Channel filtering at the RF frequency would require a tunable RF filter with prohibitively high quality factor (Q).

The RF bandpass filter is a fixed-frequency filter that attenuates out-of-band signals. The low-noise amplifier then provides primary gain for the receiver front-end. As shown in section 2.2, this first block in the receiver chain (besides the bandpass filter) has significant impact on the overall noise in the system. Thus, the main objective of the LNA design is to provide large gain with minimal noise. The other constraint in the LNA design is that its input impedance must match the output impedance of the RF filter, which is usually 50 Ω.

Since the same frequency components at IF frequencies can be created by RF signals on both sides of the LO, an undesired image signal will be superimposed on the desired signal after the first mixing (figure 2.8). This image signal can be comparable in magnitude to the desired signal, and may obscure all the information if not treated properly. In this case, an image reject filter is used before the first mixing to attenuate the image of the desired RF signal.

Although the RF bandpass filter suppresses the image signal to some extent, it will be amplified by the LNA before mixing. This is why the image-reject mixer is placed immediately before the mixer. This filter also suppresses noise in the image band.

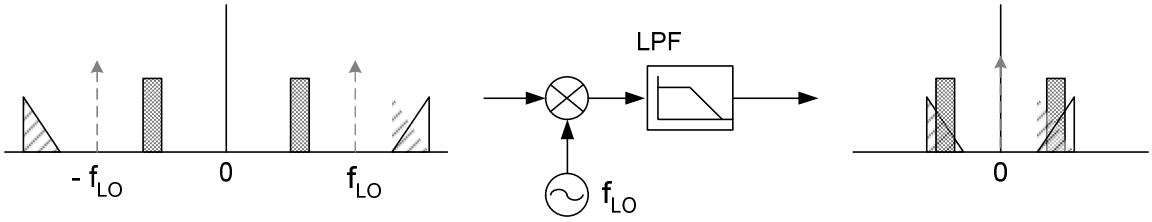

Figure 2.8 Image problem

The heterodyne architecture provides superior selectivity performance due to the benefits from including the IF stage. However, it requires many functional blocks in the system, and many of the blocks are very hard to integrate on-chip. For example, the image-reject and channel-select filters are difficult to implement on-chip due to the relatively low quality factor (Q) of the on-chip inductors. The need for additional off-chip components results in higher passive component costs, chip pin count, and extra board areas.

2.5.2 Homodyne Receiver

For a homodyne receiver (figure 2.9), the RF signal is downconverted directly to DC (or near-DC) by matching the LO frequency to the center frequency of the RF

passband. In the direct-conversion case, where the signal at RF is converted to baseband directly, the signal is placed on both sides of the LO frequency, as shown in figure 2.10. If complex modulation is used, which is more bandwidth-efficient, there will be garbling due to negative frequency components going to positive frequencies and vice versa, and an image-rejection mechanism will still be required. However, since the image is the mirror of the signal itself, the power level of the image is the same as the level of the desired signal. As a result, the image-rejection requirements can be relaxed and could be achieved with simple image-reject mixer architectures. In addition, since the channel filtering is now done at baseband, it is possible to implement it as a high-order on-chip low-pass filter.

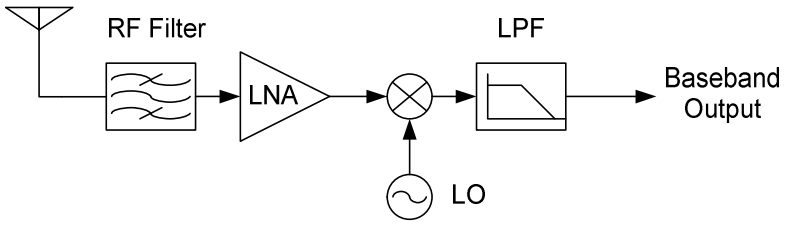

Figure 2.9 Homodyne Receiver

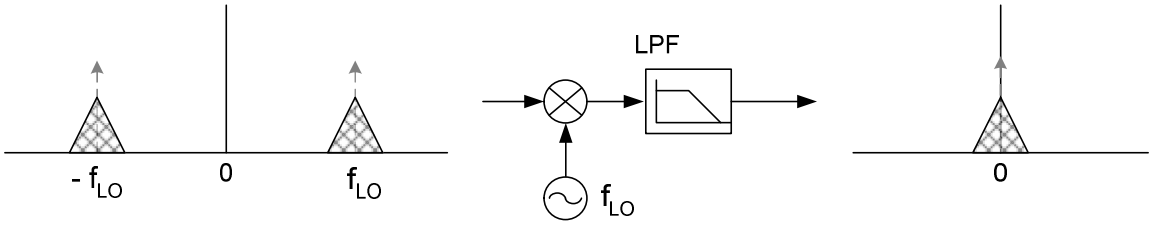

Figure 2.10 Direct-conversion frequency plan

Direct-conversion systems, however, do have some serious problems not present in heterodyne systems. Because the signal is now mixed directly to DC, any DC offset in the receiver path can corrupt the desired signal or saturate the signal path. The unwanted DC offsets can be removed by placing an AC coupling capacitor at the mixer output. However, this may adversely impact the bit-error-rate, since the signal energy at DC will be removed as well. In high-bandwidth systems such as wireless LANs, the use of an on-chip AC coupling capacitor might be acceptable without significant penalties [2.9]. However, in a system with narrower channel bandwidths, the AC coupling capacitors, if used, are of such a size such that they must be placed off-chip [2.10]. Techniques used to reduce the DC content of the signal through coding or redefinition of the baseband signal can be used to alleviate this problem. Another approach to removing the offset is to use the training signal to estimate the existing DC offset. Based on this estimation, the offset can be removed or omitted from the mixer output [2.11]. However, this method does not address dynamic DC offset or $1/f$ noise problems.

An alternative technique for addressing the DC offset problem in the direct-conversion receiver is the use of low-IF architecture [2.12]. In this case, the RF signal is down-converted to a very low IF, instead of baseband. In this case, the DC offset problem is relaxed, since the power at DC can be removed by using an on-chip AC coupling capacitor without significantly affecting the desired signal. However, the image becomes a larger problem; in this case, the image power is set by the blocking profile and usually grows stronger as the frequency moves away from the carrier. To minimize the image rejection requirement, the IF frequency is usually not more than one or two channels away from the DC, where the blocker levels are still relatively low. All

of the image rejection must be performed with a Weaver-like structure or polyphase filter (see next section) and this strongly depends on the matching between I and Q paths of the receiver. The other drawback of this architecture is that it requires higher-bandwidth baseband blocks because the signal is now moved to a higher frequency.

2.5.3 Image-Reject Mixers and Complex Filters

Several systems have been proposed to solve image problems in receivers without using an off-chip image-reject filter. These systems are called image-rejected architectures. The most common are Hartley image-reject mixers, Weaver image-reject mixers complex filters are reviewed in this section. More complete descriptions and analysis of these architectures can be found in [2.5], [2.13].

2.5.3.1 Hartley Architecture

The Hartley architecture is shown in figure 2.11. Note that the 90° phase-shifter is a Hilbert transformer with the transfer function:

$$H(j\omega) = -j\,\mathrm{sgn}(n) \tag{2.27}$$

The multiplication of the RF signal with the 90° phase-shifted LO followed by the 90° degree phase-shift inverts the signal on one side of the LO, thus distinguishing the signal from the image. Adding this to the signal that is downconverted with non-phase-shifted LO leads to image-rejection. A disadvantage of this architecture is the

need for a wideband phase-shifter that provides 90° phase shifts for the entire signal bandwidth.

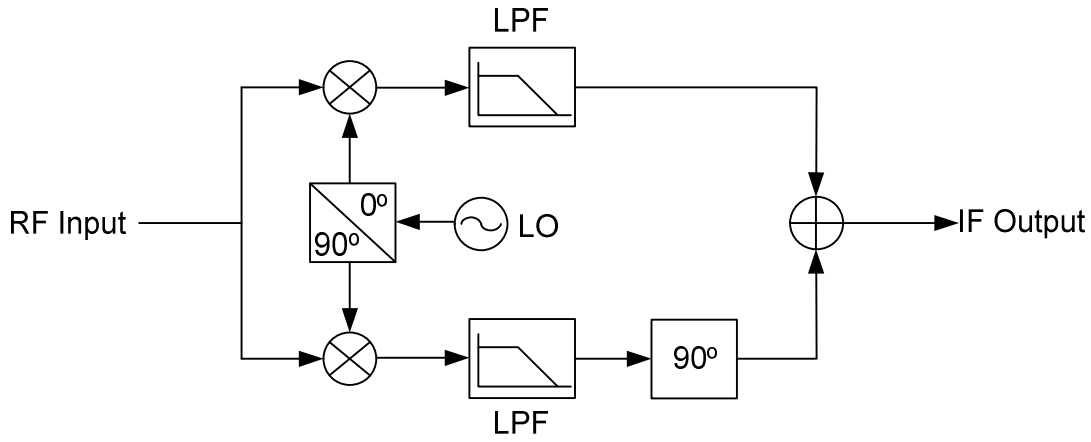

Figure 2.11 Hartley Architecture

2.5.3.2 Weaver Architecture

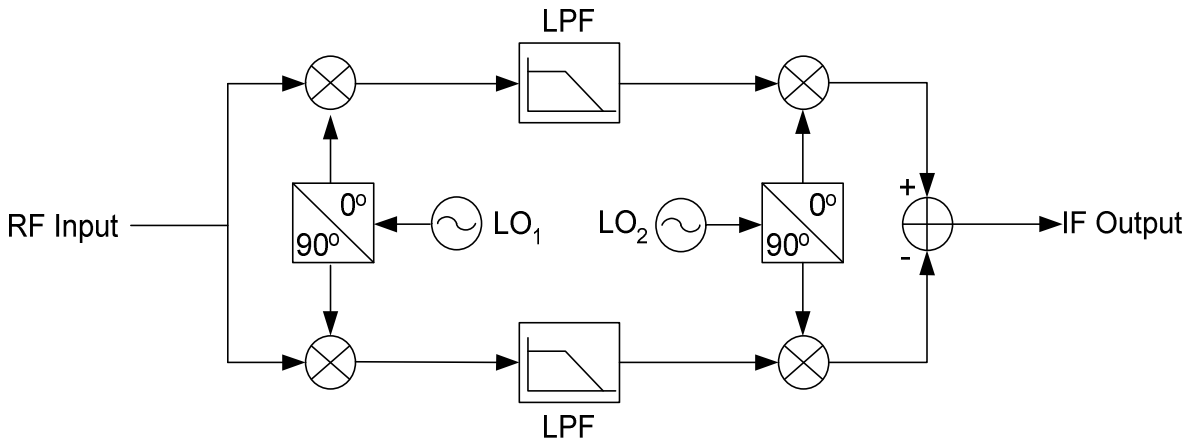

Figurer 2.12 Weaver Architecture

Unlike the Hartley architecture, the Weaver architecture uses two additional mixers placed after the low-pass filters to perform the phase-shifting instead of using a

wideband phase shifter. The RF signal is first downconverted to an intermediate frequency, then downconverted once again to the "final" IF. After the first down conversion, one path is multiplied by the sine wave, which is simply the phase-shifted cosine wave, equivalently downconverting the signal to the output frequency and phase-shifting it by 90° at the same time. The other path, which is multiplied by the cosine wave, is downconverted without the phase shift. As in the Hartley architecture, summing these two paths results in image rejection.

An advantage of using the Weaver architecture is that the wideband phase shifter is no longer needed. Although the 90° phase shifters for the LO quadrature signals are still needed, they are narrowband and easier to design.

2.5.3.3 Complex Filters

Besides image-reject mixers, complex filters are important and are widely used in receiver designs, especially in low-IF architectures [2.14][2.15]. Complex filters use cross-coupling between the real and imaginary signal paths in order to realize filters with transfer functions that do not have the conjugate symmetry (in the frequency domain) of real filters. This implies that their transfer functions have complex coefficients. The filters can be realized using basic operations, i.e., addition, multiplication, and delay operations for discrete-time digital filters, or the integrator operator for continuous-time analog filters. More information on complex mixers is given in [2.13].

2.6 Multi-Band Receivers Using Broadband Front-End

A recent trend in the electronics industry has been to integrate many features, including multi-band multi-standards compatibility, in a single handheld device. This has created a need for receivers that are compatible with as many standards as possible. In this section, we will focus on preliminary architectures and issues in designing universal radio front-ends. We will begin by discussing the challenges in designing a broadband receiver. An important issue is that most existing receiver topologies are designed for a fixed single band, or only a few bands [2.16][2.17]. Next, we will investigate the possible implementations for a universal radio receiver using architectures modified from those presented earlier in this chapter. We will compare topologies in terms of their suitability for integration and multi-band capabilities. Finally, we will give a performance estimation of a broadband receiver based on the selected topology.

2.6.1 Possible Front-end Implementations

Unlike conventional narrow-band receivers, universal receiver front-ends must be able to detect and process signals at different frequency bands. Since the operations are still narrow-band, one way to implement the receiver is to use a high-Q tunable RF bandpass filter for frequency band selection, in conjunction with a broadband LNA and mixer, as shown in figure 2.13. The RF filter is required in order to attenuate any out-of-band jammers and relax the front-end linearity requirements. For example, the out-of-band jammers could be as high as 0 dBm for the GSM standard, as shown in figure 2.3.

Such a high-Q tunable RF bandpass filter is difficult if not impossible to implement on a silicon substrate (such as CMOS IC) using current technology [2.5]. However, RF MEMS technology has shown promising results [2.18] and could become a commercially available option in the future.

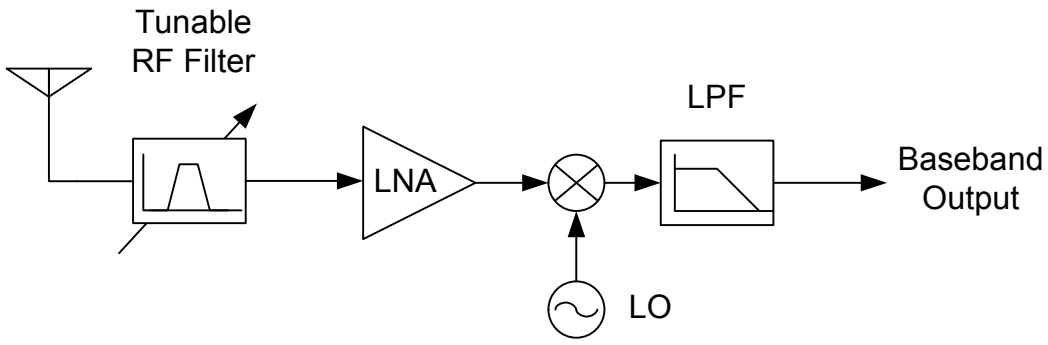

Figure 2.13 A multi-band multi-mode receiver utilizing a tunable RF bandpass filter

The need for a RF tunable filter can be avoided by implementing the "effective" tunable RF filter with several high-Q RF bandpass filters placed in parallel, each covering a frequency band for the intended application. Switches are needed to select which frequency band to use at a given time, as shown in figure 2.14. Although this method is acceptable for implementing a few narrow frequency bands, it would become impractical for generic universal radio or configurable radio, where the receiver must be able to operate in any band in the required frequency range. Moreover, these switches need to have low loss and high linearity at high frequency, both of which are not achievable by CMOS devices.

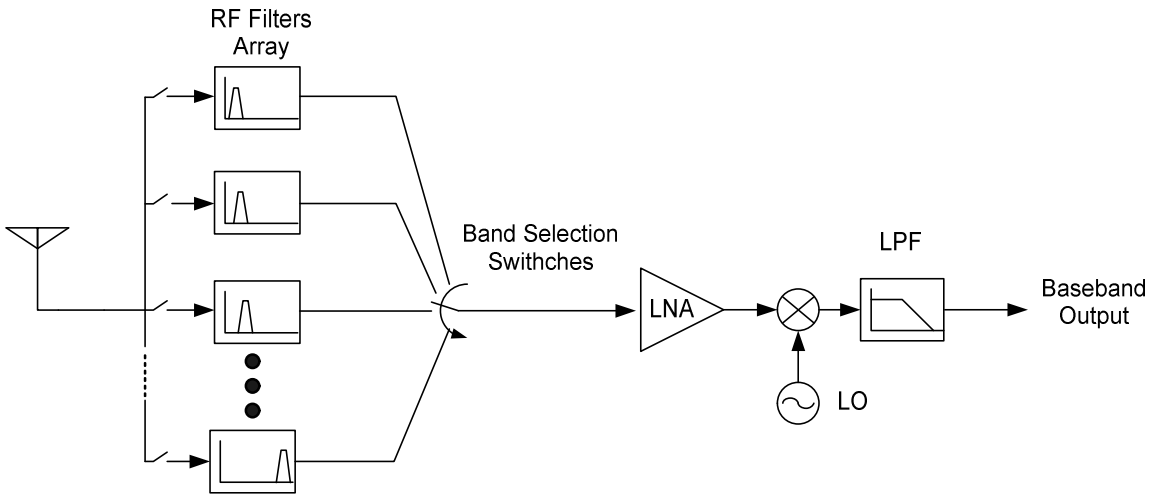

Figure 2.14 A receiver using multiple RF filters and switches

One straightforward solution for the problem of having too many RF bandpass filters is to not to perform any filtering at all. This leaves the broadband receiver with no bandpass filters in the front-ends, as shown in figure 2.15. Because there is no bandpass filtering, any large interfering signals can saturate the signal path or create intermodulation products that overtake the desired signal. For standards with stringent out-of-band jammer requirements (GSM, for example), having no out-of-band attenuation requires an extremely linear receiver front-end, which is very difficult, if not impossible, to implement in modern CMOS technologies. For some standards such as wireless LANs, there is no out-of-band blocking requirement for the standard, and the front-end linearity specifications can be relaxed. However, a high-linearity front-end is still desirable in this case due to possible jamming situations in real-world applications.

Active research has been done on implementing a receiver that can tolerate large out-of-band jammers without using filters. For example, an active filtering technique has

been proposed for removing an out-of band blocker without using an extra SAW filter in [2.19]. The circuit employs a feed-forward filter path, and the high-Q characteristic of the filter is realized by using a translinear loop.

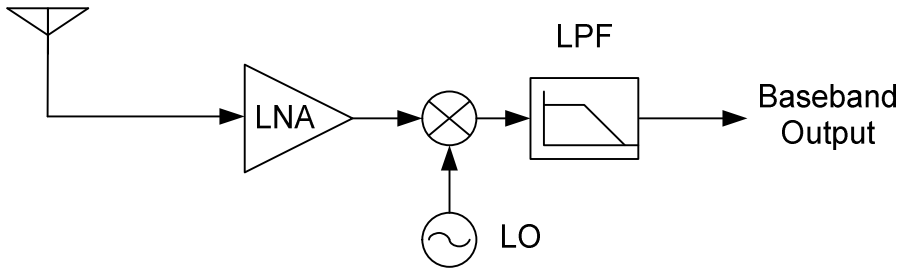

Figure 2.15 A broadband receiver with no RF bandpass filtering

If the receiver is broadband, there will be problems with harmonic distortion and harmonic mixing, as well as intermodulation distortion problems that also exist in narrow-band receiver front-ends. For example, if the intended receiving frequency can be anywhere from 0.5 MHz to 5 GHz, a strong signal at 0.8 GHz will create a third-order harmonic distortion at 2.4 GHz and will interrupt any desired signals at that frequency. Likewise, if the desired signal and LO are at 0.8 GHz (narrow channel bandwidth), a strong signal at 2.4 GHz will mix with LO harmonics locating at $3f_{LO}$ and may corrupt the desired signal. Moreover, signals at 0.9 GHz and 2.4 GHz could mix and create an IM_2 that corrupts any desired signals at 1.5 GHz. The problems of harmonic mixing and wideband harmonic distortion could be alleviated by:

(1) Using harmonic reject mixers that suppress harmonic mixing at near-LO harmonics such as at $3f_{LO}$ at $5f_{LO}$. An example of such a mixer can be found in [2.20] and has been used in [2.21].

(2) Employing differential circuits in the RF front-end paths to suppress even-order harmonics or intermodulation.

(3) Limiting the ratio between the highest and lowest frequency of the intended receiving signals to less than two by using a band-pass filter. In this case, harmonic distortions of an incoming signal will fall out-of-band and will not interfere with the intended receiving signal. In addition, any IM_2 from two strong in-band signals will fall out of band since their channel separation will always be less than the minimum intended receiving frequency. This relaxes the harmonic mixing problems as well.

Option (3) could be modified for wider frequency band coverage by using multiple RF bandpass filters, each of which covers a "group" of bands, as shown in figure 2.16. For example, one might use a filter with 0.8 GHz to 1.5 GHz passband responses to avoid any mixing between 0.9 GHz and 2.4 GHz signals falling in-band, and use another filter covering 1.4 GHz to 2.7 GHz to process the signal at 2.4 GHz. Although this might appear similar to the architecture in figure 2.14, the number of required RF bandpass filters could be vastly different. For example, to cover the frequency bands from 0.5 GHz to 5 GHz, the number of filters needed in this topology would be only 4-6, no matter how many standards exist in the range. (The 4-6 variation is due to the amount of overlapping and the chosen frequency ratio.) However, this architecture would likely require out-of-band blocking and linearity requirements similar to those without any bandpass filter. If needed, multiple broadband LNAs can be used for signals from multiple frequency groups as well.

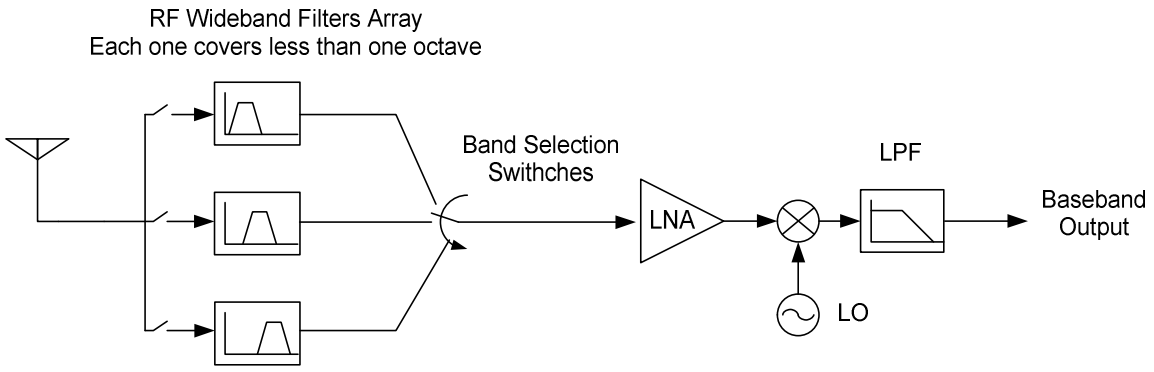

Figure 2.16 A receiver with multiple "wideband" RF bandpass filter

2.6.2 Broadband Receiver Prototype Example

From the previous section, we can see that the key components are broadband front-end building blocks regardless of receiver topologies. In this section, we will examine the basic relationships between the receiver and building block specifications in a prototype receiver. As a derivative example, the specification requirements of the prototype will be based on multiple standards presented in Table 1.1. Starting with the architecture of the receiver prototype, we will then discuss system parameters such as noise figure, linearity, and dynamic range, as well as block-level specifications.

2.6.2.1 Prototype Receiver Architecture

The conceptual diagram of the receiver can be simplified as shown in figure 2.17. In the figure, the major receiver building blocks include low-noise amplifiers (LNA), downconversion mixers, a frequency synthesizer (for LO signal generation), low-pass filters, variable-gain amplifiers (VGA), and analog-to-digital data converters (A/D).

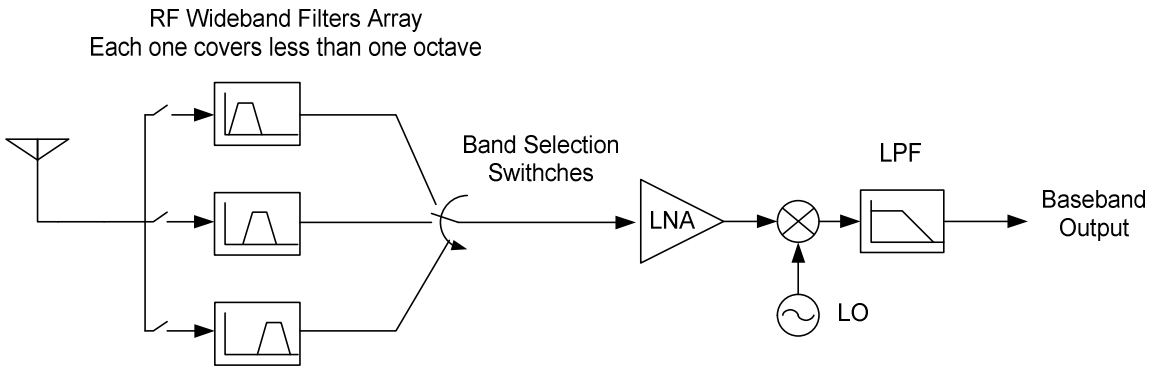

Figure 2.17 Conceptual diagram of the receiver

In this lineup, the LNA is broadband, but it could be designed as one broadband LNA or several narrow band LNAs in parallel. The I/Q image-rejection mixers downconvert the incoming signal from RF to IF frequency.(1) The LO signal is supplied by the frequency synthesizer. The synthesizer needs a voltage-controlled oscillator (VCO) that has a wide frequency tuning range in order to work with multiple bands and standards [2.22]. Also, it is necessary to have a channel bandwidth adjustment scheme that accommodates different channel bandwidths for different standards. Channel bandwidth adjustments can be implemented using the direct conversion frequency plan with a tunable low-pass IF filter, or a low-IF architecture with a tunable bandpass IF filter. The first approach is simpler but may suffer from the problems with DC offset and *1/f* noise, especially if the channel bandwidth is low, as in GSM standards [2.3]. The second approach, on the other hand, does not have low-frequency problems, but the filter design is more complicated and requires good image rejection. If needed, a low-pass filter with DC offset cancellation or AC blocking capacitors could also be used in a low-IF architecture. However, this would result in higher dynamic range requirements for the

(1) It should be noted that the above conceptual diagram shows only one mixer.

VGA and the A/D, since the adjacent channel blocker (located near DC at IF) will not be filtered out.

2.6.2.2 Basic System and Building Block Requirements

As an example, the targeted receiver requirements will be based on multiple standards shown in Table 1.1, and repeated below in Table 2.1 for important receiver requirements.

Table 2.1 Receiver requirements for different wireless standards

Range	**WAN**		**LAN**	**PAN**	**MAN**
System	GSM/DCS	UMTS	802.11a	Bluetooth	DECT
Frequency	0.9/1.8GHz	2GHz	5GHz	2.4GHz	1.9GHz
Channel spacing	200KHz	5MHz	20MHz	1MHz	1.728MHz
Rx NF	9dB	9dB	7.5dB	23dB	18dB
Rx IIP_3	-18dBm	-4dBm	-20dBm	-15dBm	-22dBm
Phase noise	-141dBc@3M	-150dBc@135M	-102dBc@1M	-105dBc@1M	-99dBc@2.2M

To meet the requirements of all the standards in Table 2.1, the receiver (not just the front-end) needs to have the following specifications:

Frequency range: 0.9 GHz – 5 GHz

RF Channel bandwidth: 200 kHz – 20 MHz

Noise Figure: 7.5 dB

IIP_3 -4 dBm

Phase Noise -141 dBc at 3 MHz

Aside from the parameters shown in Table 2.1, receiver designs have many other requirements. Some examples of these specifications include: IIP_2, image rejection, input compression and desensitization, DC offset corrections, turn-on and turn-around time, input impedance matching, and filter ripple and group delay requirements. In addition, several issues that arise specifically with wideband receivers need to be considered, and will be discussed in section 2.6.1.

In the following analysis, however, we focus only on the requirements for noise figure, IIP_3, signal level plan, and output range, since these performance metrics have the greatest impact LNA and mixer designs, and these two blocks are the focus of this dissertation.

The specifications in Table 2.1 are for a receiving path that includes everything from an antenna to the A/D outputs. In practical applications, any losses due to PCB traces or passive components at the receiver input will directly increase the overall system noise figure. Assuming that the total loss between the antenna and the chip pins is 3 dB, the total noise figure at the receiver chip input needs to be 7.5 dB - 3 dB = 4.5 dB. The system IIP_3, on the other hand, could be relaxed by the amount of loss before the input. In this case, the IIP_3 specifications can be reduced to (-4 dBm - 3 dBm) = -7 dBm at the chip input. However, since the amount of loss varies as frequency changes, and the exact amount of loss could be higher or lower than 3 dB as a design margin, the IIP_3 target should be kept at -4 dBm.

If we allocate 1 dB of noise figure degradation from blocks following the LNA, the LNA itself needs to have noise figures of 4.5 dB - 1 dB = 3.5 dB or better. For IIP_3, if the IF filter provides sufficient stop-band rejection, any subsequence blocks (such as

VGA and A/D) will have minimal impact on the system IIP_3 since any interference will be highly attenuated at the filter output. As a result, the total front-end IIP_3 can be estimated using (2.21) along with the gain and linearity profiles of the LNA, mixers, and IF filters. An example of an RF front-end building block specification that meets the noise figure and IIP_3 requirements (NF < 4.5 dB, IIP_3 > -4 dBm) is given below:

Table 2.2 Example of LNA, mixer, and filter specifications

Blocks	Gain (dB)	NF (dB)	IIP_3 (dBm)
LNA	16	3.5	0
Mixer	15	10	15
Filter and subsequence blocks (filter input referred, max gain)	50	20	30
Cascaded (LNA+Mixer)	81	4.1	-3.1

Another important design consideration is the signal level plan, or how the signal level is adjusted along the receiver path. More specifically, the receiver gain control and A/D interface need to be chosen so that:

(1) There is enough gain to meet the signal level requirement when the incoming signal level is low.

(2) The receiver has enough dynamic range to handle significant interference in the event that the desired signal is weak (near-far problem). Even with channel filtering, the incoming blockers can be substantially larger than the desired

signal at the receiver output. This dictates the receiver linearity requirement, channel filter out-of-band rejection, and A/D dynamic range.

(3) Finally, in the event that the desired receiving signal is very strong, the minimum receiver gain (from LNA to VGA) needs to be low enough so that the output signal level will not be compressed along the signal path (likely at the VGA output or A/D input). This requirement is different from that in (2) above because the desired signal will not be attenuated by the filter as in the previous case.

For example, if a 10-bit A/D with $1V_{p\text{-}p}$ input full-scale voltage swing is used at the receiver output, the A/D dynamic range will be approximately 60 dB (around 6 dB per bit) with 1 mV LSB. The required maximum gain of the receiver can be calculated from the LSB of the A/D and the required signal level above the A/D quantization noise. For example, if the system requires the rms signal level to be 30 dB above the A/D LSB, and the required sensitivity is -100 dBm (-113 dBVrms), the required maximum receiver gain is then:

$$RxGain_{\max} = (30 + 20\log(1\text{m})\ \text{dBVrms}) - (\text{-}113\ \text{dBVrms}) = 83\ \text{dB} \tag{2.28}$$

The required minimum gain of the receiver, on the other hand, can be calculated from the A/D full-scale range and the largest possible receiving or interfering signal. Because an unwanted signal will be heavily attenuated by the IF filter, the minimum gain of the receiver can be determined by the maximum input level of the desired signal and

the A/D full-scale range (which is 60 dB above LSB). If the maximum desired input level is -15 dBm (-28 dBVrms), the required minimum receiver gain is then:

$$RxGain_{\min} = (60 + 20\log(1\text{m})\ \text{dBVrms}) - (-28\ \text{dBVrms}) = 28\ \text{dB} \qquad (2.29)$$

Usually, we can attenuate the desired signal at the LNA input, since noise figure is not a concern in this situation (the signal level is already high, so the SNR degradation is not a concern). If a large interference is present when the desired signal is low (near-far situation), the LNA gain must be kept high in order to maintain the low noise figure of the system, and the filter rejection needs to be large enough to prevent any signal compression at the receiver output (A/D input). For example, if the interference can be as high as -20 dBm (-38 dBVrms) while the desired signal is at -100 dBm (-113 dBVrms), the receiver gain needs to be 83 dB according to (2.28), while the rejection needs to be high enough to keep the inference level below the A/D range. This can be written as:

$$(60 + 20\log(1\text{m})\ \text{dBVrms}) > (-38\ \text{dBVrms}) + (83\ \text{dB}) - \text{Rejection}$$

$$\text{Rejection} > 45\ \text{dB} \qquad (2.30)$$

Another requirement in this situation is that the blocks preceding the IF filter are linear enough to handle the -25 dBm interference.

2.7 References

[2.1] A. K. Wong, and R. G. Meyer "Blocking and Desensitization in RF Amplifiers," *IEEE Journal of Solid-State Circuits,* Vol. 30, No. 8, August 1995, pp. 944-946.

[2.2] J. C. Rudell, "Frequency translation techniques for high-integration high-selectivity multi-standard wireless communication systems", Ph.D. Dissertation, UC Berkeley, 2000

[2.3] ETSI, "Global System for Mobile Communications", Digital cellular telecommunications system (Phase 2+); Radio transmission and reception, GSM 5.05, Version 5.2.0, Copyright 1996.

[2.4] R. G. Meyer, EE242 Lecture Notes, University of California, Berkeley, 2004

[2.5] B. Razavi. *RF microelectronics*. Prentice-Hall, Upper Saddle River, New Jersey, 1997.

[2.6] A. Behzad, "The implementation of high-speed experimental transceiver module with an emphasis on CDMA applications" Master Thesis, ERL Memorandum No. UCB/ERL M95/40, June 1995.

[2.7] B. Limketkai, "The Design and Implementation of A Downconversion Mixer For a wideband CDMA Receiver". MS Thesis, UC Berkeley, 1999.

[2.8] T. Lee. *The Design of CMOS Radio-Frequency Integrated Circuits*. Cambridge University Press, Cambridge, UK, 1998.

[2.9] D.Yee, et al., "A 2-GHz Low-Power Single-Chip CMOS Receiver for WCDMA Applications," Proceedings of *ESSCIRC 2000*, September 2000, Stockholm, Sweden.

[2.10] C. Hull, et al., "A Direct-Conversion Receiver for 900MHz (ISM Band) Spread-Spectrum Digital Cordless Telephone," *ISSCC Dig. Tech. Papers*, pp. 344-345, February 1996.

[2.11] J. Cavers and M. Liao, "Adaptive Compensation for Imbalance and Offset Losses in Direct Conversion Transceivers." *IEEE Transactions on Vehicular Technology*, vol. 42, pp. 581-588, November 1993.

[2.12] M. Steyaert, et al., "A Single-Chip CMOS Transceiver for DCS-1800 Wireless Communications," *Proceedings of the 1998 ISSCC*, pp. 48-49.

[2.13] K. W. Martin, "Complex Signal Processing is not Complex", *IEEE Trans. Circuits Syst. I*, Vol. 51, No. 9, September 2004.

[2.14] J. C. Rudell, J. Ou, T. B. Cho, G. Chien, F. Brainti, J. A. Weldon, and P. R. Gray, " A 1.9-GHz Wide-Band IF Double Conversion CMOS Receiver for Cordless Telephone Applications", *IEEE J. Solid-State Circuits*, vol. 32, pp. 2071-2088, December 1997.

[2.15] J. Crols and M. Steyaert, "Low-IF Topologies for High-Performance Analog Front Ends of Fully Integrated Receivers", *IEEE Trans. Circuits Syst. II*, vol.45, pp. 269-282, March 1998.

[2.16] M. Zargari, et al., "A Single-Chip Dual-Band Tri-Mode CMOS Transceiver for IEEE 802.11a/b/g WLAN*", ISSCC Dig. Tech. Papers*, pp96-97, February 2004.

[2.17] O. E. Erdogan, et al., "A Single-Chip Quad-Band GSM/GPRS Transceiver in 0.18⌠m Standard CMOS". *ISSCC Dig. Tech. Papers*, pp 318-319, February 2005.

[2.18] C. Nguyen, "Vibrating RF MEMS for next generation wireless applications," in *Proc. IEEE 2004 Custom Integrated Circuits Conf.*, Piscataway, NJ, IEEE Press, 2004, pp. 257-264.

[2.19] H. Darabi, "A Blocker Filtering Technique for SAW-Less Wireless Receivers," *IEEE J. Solid-State Circuits*, vol. 42, no. 12, pp. 2766-2773, December 2007.

[2.20] J. Weldon, et al., "A 1.75-GHz highly integrated narrow-band CMOS transmitter with harmonic-rejection mixers," *IEEE J. Solid-State Circuits*, vol. 36, no. 12, pp. 2003-2015, December 2001.

[2.21] R. Bagheri, A. Mirzaei, S. Chehrazi, M. Heidari, M. Lee, M. Mikhemar, W. Tang, and A. A. Abidi, "An 800-MHz-6-GHz software-defined wireless receiver in 90-nm CMOS," *IEEE J. Solid-State Circuits*, vol. 41, no. 12, pp. 2860-2876, December 2006.

[2.22] A. Berny, A. M. Niknejad, R. G. Meyer "A 1.8-GHz LC VCO with 1.3-GHz Tuning Range and Digital Amplitude Calibration," *IEEE J. Solid-State Circuits*, vol. 40, no. 4, pp. 909-917, April 2005.

3

CMOS LNA Fundamentals

3.1 Introduction

In a receiver, the low-noise amplifier (LNA) serves as the first amplification block along the receiving path. As explained in chapter 2, it is one of the most critical building blocks of the receiver, since its performance greatly affects both the sensitivity and selectivity of the system. In this chapter, we will review the basic properties of a CMOS LNA. Starting with a discussion of noise sources in CMOS transistors in section 3.2, in section 3.3 we will proceed through a classic two-port noise theory. Finally, we will present a review of input matching and low-noise amplifier topologies.

3.2 Noise Sources in MOS Transistors

Before initiating an analysis of how to design a low-noise amplifier, we must identify and understand the origins of noise. This section provides insights into the most important noise sources in MOS transistors, such as drain current noise, induced gate noise, and flicker noise.

3.2.1 Drain Current Noise

Since the channel material in MOS transistors is resistive, it exhibits thermal noise. This noise source can be represented by a current noise generator connecting from drain to source in the small signal model, as shown in figure 3.1, and is called "drain current noise." The expression for this noise is given by [3.3]:

$$\overline{i_{nd}^2} = 4kT\gamma g_{d0}\Delta f \tag{3.1}$$

where g_{d0} is the drain to source conductance at zero V_{ds}. The parameter γ has a value of unity at zero V_{ds} and moves toward 2/3 in saturation for long-channel devices. In the short-channel device, however, the value of γ can be considerably larger (typically 1.4-2) due to velocity saturation in short-channel devices [3.4].

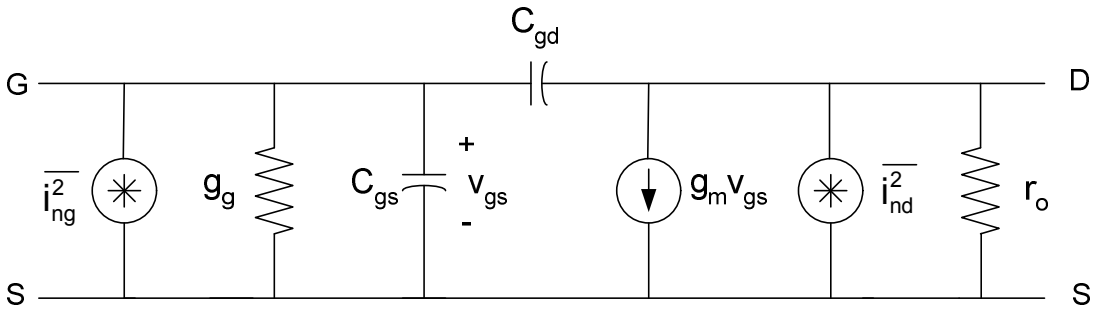

Figure 3.1 Drain current and gate noise models

3.2.2 Induced Gate Noise

The other consequence from the thermal agitation of channel charge, besides drain current noise, is induced gate noise [3.5]. The fluctuating channel potential couples

capacitively into the gate terminal, leading to a noisy gate current. This noise is negligible at low frequencies because the coupling effect is small. However, it can be problematic at radio or microwave frequencies. This noise is modeled as a current noise generator connecting from gate to source in the small signal model (see figure 3.1), and may be expressed as [3.3]:

$$\overline{i_{ng}^2} = 4kT\delta g_g \Delta f \tag{3.2}$$

where the parameter g_g is:

$$g_g = \frac{\omega^2 C_{gs}^2}{5 g_{d0}} \tag{3.3}$$

The parameter δ is a gate noise coefficient and equals 4/3 for long-channel devices [3.3], which is twice as large as γ. For short channel devices, however, this value is still not accurately known. A reasonable approximation is that δ should continue to be about twice as large as γ. Since γ is around 1.4-2 for the short-channel device, δ should be around 3-4 [3.5].

As mentioned earlier, the gate noise is related to the drain noise. In fact, it is partially correlated to the drain noise with a correlation coefficient c, as stated in equation 3.5 below.

$$c = \frac{\overline{i_{ng} i_d^*}}{\sqrt{\overline{i_{ng}^2}\,\overline{i_d^2}}} \tag{3.4}$$

The value for c is given in [3.2] as 0.395j for long-channel devices. Since the coupling between the gate noise and drain noise is through the gate capacitance, the correlation coefficient is purely capacitive.

One drawback of the induced gate-noise expressions in (3.2) and (3.3) is that the noise model is frequency dependent. For designers who prefer to analyze circuits using only noise source models that are frequency independent, it is possible to modify the gate noise model to a form with a noise voltage source that has a flat spectrum density. To derive this alternative model, we must first transform the parallel RC network represented by g_g and C_{gs} into an equivalent series RC network as shown in figure 3.2. If the network has a reasonably high Q, the capacitance stays approximately constant during the transformation. The parallel conductance g_g becomes a series resistance whose value is:

$$r_g = \frac{1}{g_g}\frac{1}{Q^2+1} \approx \frac{1}{g_g Q^2} = \frac{1}{5g_{d0}} \tag{3.5}$$

If we equate the short-circuit elements of the original network and the transformed version with the assumption of high Q, the equivalent series noise voltage source is then found to be [3.5]:

$$\overline{v_{ng}^2} = 4kT\delta r_g \Delta f = \overline{i_{ng}^2}\left(\frac{r_g}{g_g}\right) = \overline{i_{ng}^2}\left(\frac{1}{\omega^2 C^2}\right) \tag{3.6}$$

which has a constant spectral density. Finally, using (3.6) and (3.4), we can find the correlation coefficient between the voltage noise to drain current noise as:

$$c_v = \frac{\overline{v_g i_d}^*}{\sqrt{\overline{v_g}^2 \overline{i_d}^2}} = \frac{\overline{i_{ng} i_d * \left(\frac{1}{\omega C}\right)}}{\sqrt{\overline{i_{ng}}^2 \overline{i_d}^2 \left(\frac{1}{\omega^2 C^2}\right)}} = c \tag{3.7}$$

which is the same as the correlation coefficient provided by (3.4)

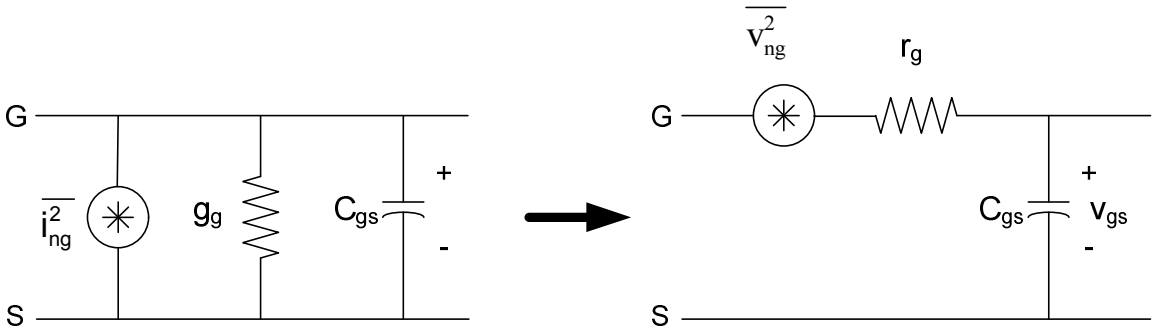

Figure 3.2 MOS input RC network model transformation

3.2.3 Flicker Noise

The other important noise source in MOS transistors is flicker noise. The origin of this noise varies, but it is mainly attributed to traps associated with contamination and crystal defects. Since MOS transistors conduct current near the surface of the silicon, where traps created by defects and impurities are most plentiful, their flicker noise components can be large. These traps capture and release carriers in random fashion, and the trapping times are distributed in a way that leads to a *1/f* noise spectrum.

Flicker noise can be modeled as a current noise generator connecting from drain to source in the small signal model and can be expressed by [3.5]:

$$\overline{i_{nf}^2} = \frac{K_f}{f}\frac{g_m^2}{WLC_{ox}^2}\Delta f \tag{3.8}$$

where K_f is a constant that depends on the technology process. C_{ox} is the gate oxide capacitance per unit area. Note that the flicker noise is inversely proportional to the area of the gate (WL) because the larger gate capacitance smoothens the fluctuation in channel charges. Also, it is worth mentioning that flicker noise is always associated with a flow of direct currents. If there is no direct current flowing in the device, this noise should be minimal [3.6].

3.2.4 Other Noise Sources

The distributed gate resistance of the CMOS transistor also contributes to the noise in low-noise amplifiers. This noise source is usually modeled as a series resistance at the gate and the noise power is given by:

$$\frac{\overline{v_g^{\,2}}}{\Delta f} = 4kTR_g \tag{3.9}$$

$$R_g = \frac{R_{sq}W}{3n^2L} \tag{3.10}$$

where R_g is the gate resistance, R_{sq} is the sheet resistance of polysilicon, and n is the number of fingers. The factor 3 comes from the distributed nature of the gate resistance assuming that each finger is only contacted at one end. If both ends are contacted, the

factor became 12. Increasing the number of fingers for a given overall transistor width decreases the transistor width per finger, and reduces gate resistance noise.

Another noise source mentioned in [3.7] is from resistance due to the lightly doped drain diffusion regions. Because no distinction is made between the source and drain, this resistance is also present at the source, and cannot be mitigated by proper layout. This resistance is given in equation by:

$$R_{source\ ,drain} = \frac{R_{LDS}}{W} \tag{3.11}$$

where R_{LDS} is the resistance per unit transistor width.

3.3 Two-Port Noise Theory

In this section, we will look at noise from a macroscopic point of view in a two-port network. Using the system model greatly simplifies the noise problems, as will be shown later in this chapter.

Starting with the model in figure 3.3a, the linear noisy two-port network is driven by a source with admittance Y_s. If we are interested in only the input-output behavior, it is not necessary to keep track of all the internal nodes and noise sources of the circuits. In this case, the noisy two-port network can be replaced by a noiseless two-port network with external current and voltage noise generators at the input as shown in figure 3.3b.

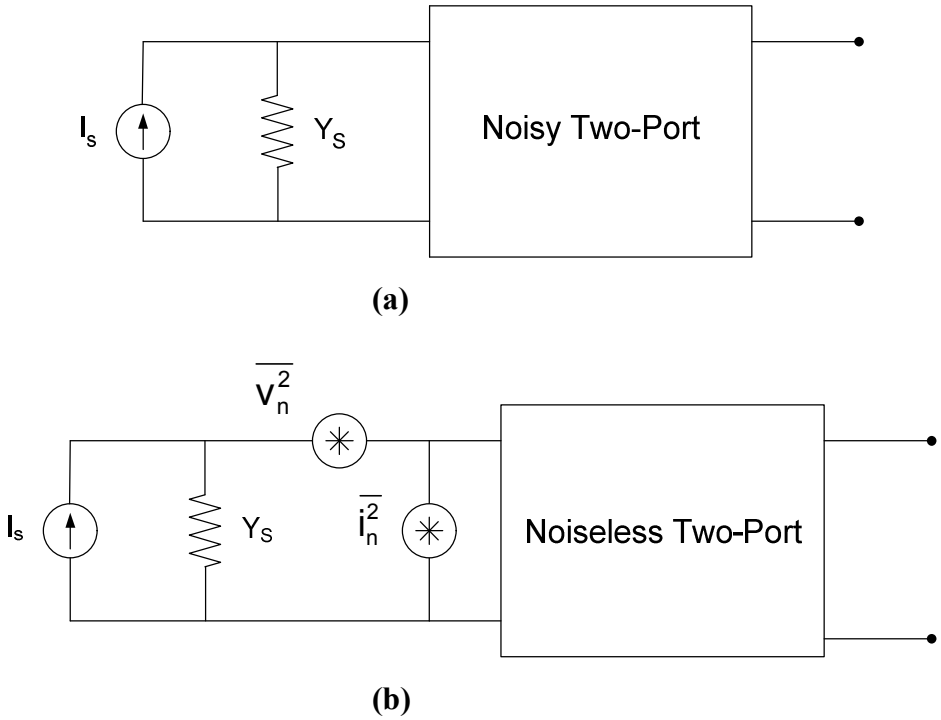

Figure 3.3 (a) Noisy two-ports driven by noise source, (b) equivalent noise model

Recall from chapter 2 that the noise factor is defined as:

$$F \equiv \frac{\text{total output noise power}}{\text{output noise due to inpout source}} \tag{3.12}$$

All the noise sources are now input-referred, as in figure 3.3b, and the output power contribution from each term is proportional to its short-circuit current at the input. As a result, we can now derive the noise factor by calculating the total short-circuit mean-square input noise current, and divide that total by the short-circuit mean-square noise current generated from the input source. The expression then becomes:

$$F = \frac{\overline{i_s^2} + \overline{\left| i_n^2 + Y_s v_n^2 \right|^2}}{\overline{i_s^2}} \tag{3.13}$$

In the equation above, we have assumed that the noise from the source and the equivalent noise generators are not correlated. However, there is a correlation between the current noise generator and the voltage noise generator. We can write i_n as:

$$i_n = i_c + i_u \tag{3.14}$$

Where i_c is the part of i_n that is correlated with v_n, and i_u is the part of i_n that is uncorrelated with i_n. Since i_c is correlated with v_n, it can be written as:

$$i_c = Y_c v_n \tag{3.15}$$

The constant Y_c is known as the correlation admittance [3.5].

Putting (3.14) and (3.15) into the equation (3.13), we get a modified expression for the noise factor:

$$F = \frac{\overline{i_s^2} + \overline{\left| i_u^2 + \left(Y_c + Y\right)_s v_n^2 \right|^2}}{\overline{i_s^2}} = 1 + \frac{\overline{i_u^2} + \left| Y_c + Y_s \right|^2 \overline{v_n^2}}{\overline{i_s^2}} \tag{3.16}$$

The expression above contains three independent noise sources. We can then define:

$$R_n = \frac{v_n^2}{4kT\Delta f} \tag{3.17}$$

$$G_u = \frac{i_u^2}{4kT\Delta f} \tag{3.18}$$

$$G_s = \frac{i_s^2}{4kT\Delta f} \tag{3.19}$$

Using equations (3.16)-(3.19), we can then write the noise factor in terms of noise admittances and impedances as:

$$F = 1 + \frac{G_u + \left|Y_c + Y_s\right|^2 R_n}{G_s} = 1 + \frac{G_u + \left[\left(G_c + G_s\right)^2 + \left(B_c + B_s\right)^2\right] R_n}{G_s} \tag{3.20}$$

At this point, the optimal admittance can be found by taking the first derivatives of the equation above with respect to the source conductance and source susceptance and turning it into zero. This yields:

$$B_s = -B_c = B_{opt} \tag{3.21}$$

$$G_s = \sqrt{\frac{G_u}{R_n} + G_c^2} = G_{opt} \tag{3.22}$$

Substituting (3.21) and (3.22) into (3.20) gives the following result for the minimum noise figure:

$$F_{\min} = 1 + 2R_n\left(G_{opt} + G_c\right) \tag{3.23}$$

Using equation 3.21, we get the general expression for noise figure:

$$F = F_{\min} + \frac{R_n}{G_s}\left[\left(G_s - G_{opt}\right)^2 + \left(B_s - B_{opt}\right)^2\right] \tag{3.24}$$

From equation 3.24, it can be seen that the contours of constant noise factor (and noise figure) are circles centered about (G_{opt}, B_{opt}) in the admittance plane.

3.4 Impedance Matching in LNA Designs

Impedance matching is important in an LNA design because the system performance is often strongly affected by the quality of the termination [3.7]. For instance, the frequency response of the antenna filter that precedes the LNA will deviate from its normal operation if there are reflections from the LNA back to the filter. Furthermore, undesirable reflections from the LNA back to the antenna must also be avoided. An impedance is matched when $Z_S = Z_L$ as in figure 3.4.

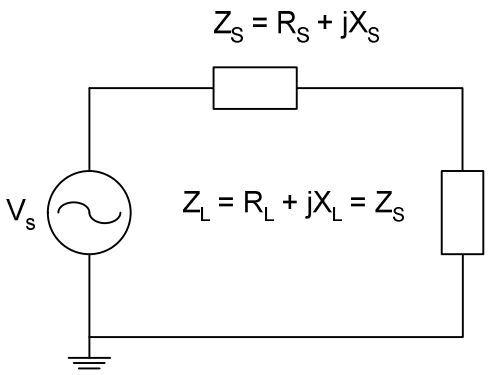

Figure 3.4 Condition for an impedance match

There is a subtle difference between impedance matching and power matching. As stated in the previous paragraph, the condition for impedance matching occurs when the load impedance is equal to the characteristic impedance. However, the condition for power matching occurs when the load impedance is the complex conjugate of the characteristic impedance. When the impedances are real, the conditions for power matching and impedance matching are the same.

3.5 LNA Input Matching Topologies

As mentioned in the previous section, impedance matching is very important in LNA designs. In most cases, the source impedance of the LNA is 50 Ω in a wireless system. Since the input impedance of the MOS transistor is almost purely capacitive, providing a good match to the source without degrading noise performance is a challenge. In this section, we will investigate a number of circuit topologies that can be used for the tasks and discuss their properties.

3.5.1 Resistive Termination

This is the most straightforward approach to achieve broadband 50 Ω matching at the input, as shown in figure 3.5. The 50-Ω resistor (R_1) is placed across the input terminal of the LNA thus providing a broadband input matching if R_1 equals R_S.

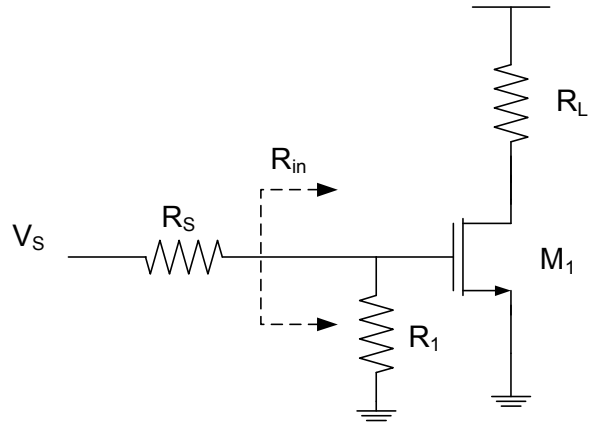

Figure 3.5 Resistive termination matching

The matching bandwidth of this matching topology is determined by the input capacitance of the transistor M_1 and is given by:

$$f_{-3dB} = \frac{1}{2\pi C_g \left(R_1 // R_S \right)} \tag{3.25}$$

where C_g is the equivalent capacitance looking into the gate of M_1. For deep-submicron CMOS technology, C_g could be in the range of 1-2 pF for devices with moderate transconductance. This leads to several gigahertz of bandwidth in a 50-Ω system.

However, the resistor R_1 adds its own thermal noise to the circuit and attenuates the incoming signal by a factor of two before it hits the gate of the transistor. These two effects result in a high noise factor of the circuit, hence the method is not practical in low-noise applications. Ignoring all the noises from the transistors and subsequence circuits, the lower bound of the noise factor is 2 in an ideal match condition.

3.5.2 Shunt-Series Feedback

Another method used to obtain good input matching is the shunt-series feedback amplifier, as shown in figure 3.6. Unlike the resistive termination case, it does not attenuate the signal by a noisy attenuator before reaching the gate of the amplifying device, so the noise figure can be much better. However, the feedback resistor continues to generate thermal noise of its own and could contribute significantly to the overall output noise.

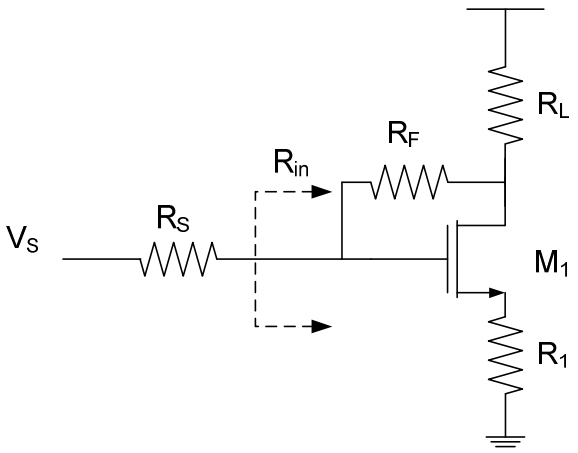

Figure 3.6 Shunt-series feedback matching

If R_1=0, the input resistance of the amplifier shown above is (detailed analysis will be given in chapter 7):

$$R_{in} = \frac{R_L + R_F}{1 + g_m R_L} \tag{3.26}$$

Since R_{in} is determined by R_L, R_F, and g_m, it is possible to design the matching stage with M_1 having high g_m and low input referred noise. This input match design flexibility, in addition to its simplicity and compactness, makes a shunt-feedback LNA topology an attractive choice for multi-band LNA designs. Chapter 7 provides a detailed analysis and a design example of a low-power differential shunt resistive LNA as part of a wideband receiver front-end.

Several works on broadband CMOS LNAs have been published using resistive shunt-feedback architecture or its variations [3.8][3.9][3.10]. For example, in [3.8], a resistive feedback LNA with 3-dB bandwidth higher than 8 GHz and noise figure below

3 dB is reported. The LNA, which is single-ended, has been implemented in 90-nm CMOS technology with active area of 0.025 μm^2, and consumes 42 mW from a 2.7 V supply.

3.5.3 Common-Gate Input

Another method for realizing resistive input matching is to use a common-gate configuration. As shown in figure 3.7, the source terminal is used as an input terminal. As the figure also shows, the source terminal is used as an input terminal. Since the impedance looking into the source of a common gate amplifier is $1/g_m$, it can be set by proper device sizing and by adjusting the bias current of the circuit. This creates a drawback of this configuration, in that g_m is fixed once the source resistance is known.

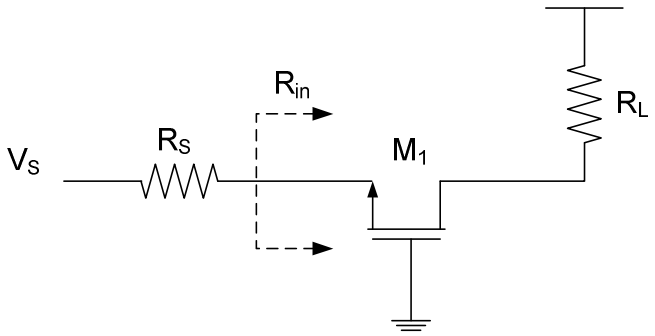

Figure 3.7 Common-gate input matching

Since the input resistance is the reciprocal of transistor g_m and the dominant capacitor at the input terminal is the device C_{gs}, we can expect that the matching bandwidth is close to the transition frequency (f_t) of the device.

Neglecting gate and flicker noises and assuming a perfect match, we can express the lower bound of the noise figure for the amplifier that uses this matching technique as:

$$F \geq 1 + \frac{\gamma g_m}{g_{d0}} \tag{3.27}$$

The numerical value for the lower bound expressed above is about 2.2dB for long-channel devices and 4.8dB for short-channel devices [3.5].

The $R_{in}=1/g_m$ restriction can be avoided by applying a modified version of the input signal at the gate of M_1 in order to manipulate the effective g_m of the device, as shown in figure 3.8.

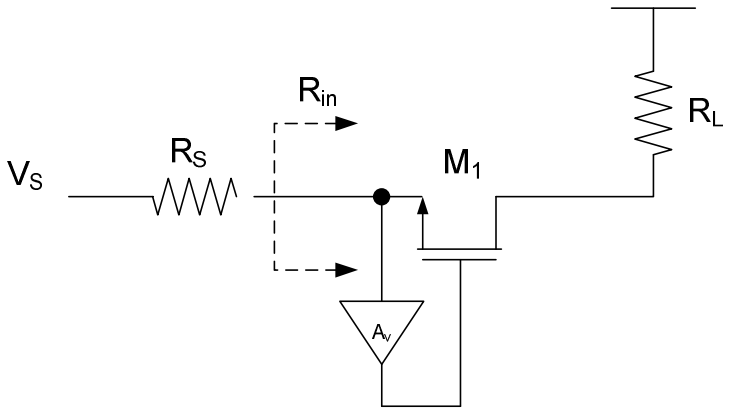

Figure 3.8 Common-gate input matching with gain boosting

In this case, the effective transconductance of M_1 can be described by

$$G_{m,M1} = g_m(1 - A_V) \tag{3.28}$$

If A_v is negative, the effective transconductance increases by a factor of $1+|A_V|$, and the input resistance decreases by the same factor. For low-power applications, the method can be used to reduce the required g_m and bias current for a given input impedance requirement. In addition, the gain stage with A_v of -1 can be easily realized in a differential input structure when an inverted version of the input signal is available on the other side of the input. This technique has been used in [3.11] in conjunction with a complementary PMOS-NMOS current reuse architecture to achieve four times higher g_m without additional device bias currents.

The signal applied at the gate M_1 (as in figure 3.8) can also be implemented by using a feedback network that feeds back the signal from the LNA output. The work presented in [3.12] uses a negative feedback around a common base stage of the BJT input device to reduce the noise, and correlates the input impedance to the output load using a capacitive divider as a feedback network. Since the feedback is capacitive, the architecture allows easy reconfigurability of the amplifier with very little noise degradation. However, this architecture requires a device with high current gain and low output capacitances in order to achieve sufficient loop gain; thus it becomes less attractive when CMOS is the process technology to be used instead of BiCMOS, where fast BJT devices with low collector capacitances are available.

Another way to use a feedback network to change the input impedance of a common-gate stage is shown in figure 3.9 [3.13]. In this circuit, a positive current feedback network via M_2 is used to add an extra degree of freedom between the value of R_s and g_{m1}. The input impedance in this circuit topology is given by [3.13].

$$R_{in} = \frac{1}{g_{m1}\left(1 - g_{m2}R_L\right)} \tag{3.29}$$

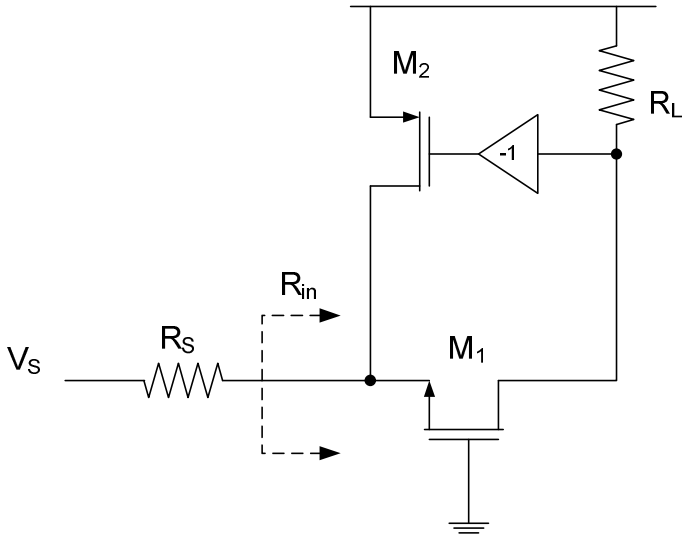

Figure 3.9 Common-gate input matching LNA with positive feedback

If $g_{m2}R_L$ is close to but lower than unity, the value of g_{m1} can be chosen to be much higher than $1/R_S$. This allows the use of high-g_m input devices that have lower input referred noise, resulting in an achievable noise figure close to that of the inductively degenerated amplifier [3.14].

Since the feedback is positive, careful design is needed to ensure that the amplifier is stable over all frequency ranges. This could be especially challenging when process variations are taken into account and the $g_{m2}R_L$ product is close to unity (to allow higher g_{m1}).

3.5.4 Noise-Canceling LNA Architecture

As discussed in section 3.5.3, the transconductance value of the input device in the common-gate architecture is required to be $1/R_S$ unless extra circuitry is added to alter the effective transconductance of the device. This is also the case in a shunt-feedback amplifier when $g_m R_L >> 1$ and $R_F << R_L$. In both cases, this requirement results in high noise contributions from the input transistor and a high noise figure of the circuit. This noise contribution from the input devices, however, could be suppressed by using noise-cancelling techniques [3.15][3.16][3.17].

Figure 3.10 shows a version of a non-canceling low-noise amplifier as reported in [3.15]. It consists of the input matching part and the noise canceling circuitry path. First, let us consider the desired signal (V_S) coming from the voltage source. Due to the inverting nature of the shunt feedback amplifier, the scaled version of the desired signal at node X will have opposite polarity compared to the scaled version of the signal at node Y. In contrast, the noise voltages at node Y and X generated by the drain current noise of M_1 have the same phase. If a noiseless stage with the gain of $-A_v$ is added to amplify the signal at node X, the amplified output signal of this gain stage, which is at node Z, will have the same polarity as the signal at node Y. The noise voltage due to the drain current noise of M_1, however, will appear at node Z with the phase opposite to the noise voltage at node Y. By adding together the signal and noise at nodes Y and Z, the desired signal will be added constructively while the noise from nodes Y and Z will cancel, resulting in a signal to "M_1 noise" ratio that is much higher than at node Y.

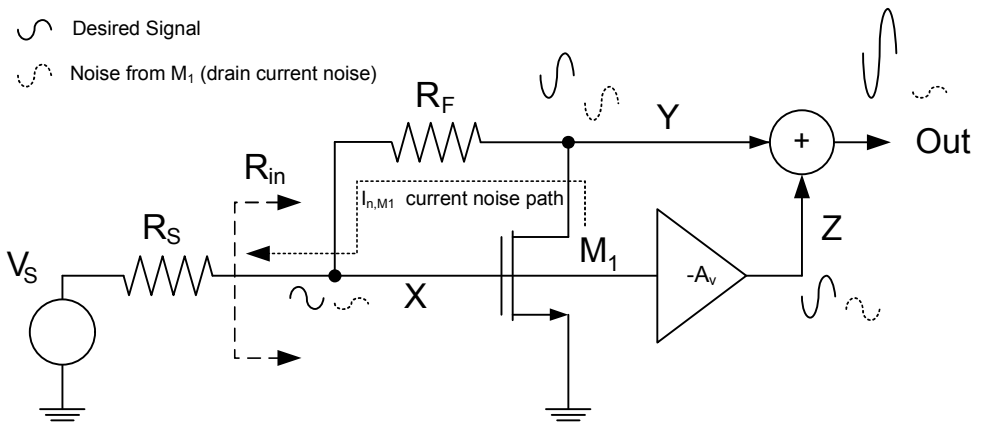

Figure 3.10 Shunt-feedback LNA input matching with noise-canceling

Due to the noise-canceling mechanism, the transconductance of M_1 could be chosen almost entirely by input matching considerations since its noise contributions can be significantly reduced. However, noise contributions from the noise-canceling path ($-A_v$ path) are not canceled out, and the input referred-noise of this path must be kept low.

Another low-noise amplifier with noise-canceling input match is shown in figure 3.11 [3.16]. This circuit consists of common-gate (M_1) and common-source stages (M_2) connecting at the input node. If the parasitic capacitance at the gate of M_2 is relatively small, the input impedance of this amplifier will be determined by the common-gate stage (M_1), and can be set to R_s by setting the g_m of M_1. If we take the output differentially at the drain of M_3 and M_4, the voltage gain through the path of M_1 and M_2 will be constructive (that is, the amplified signal at the drain of M_3 will be out-of-phase compared to the amplified signal at the drain of M_4).

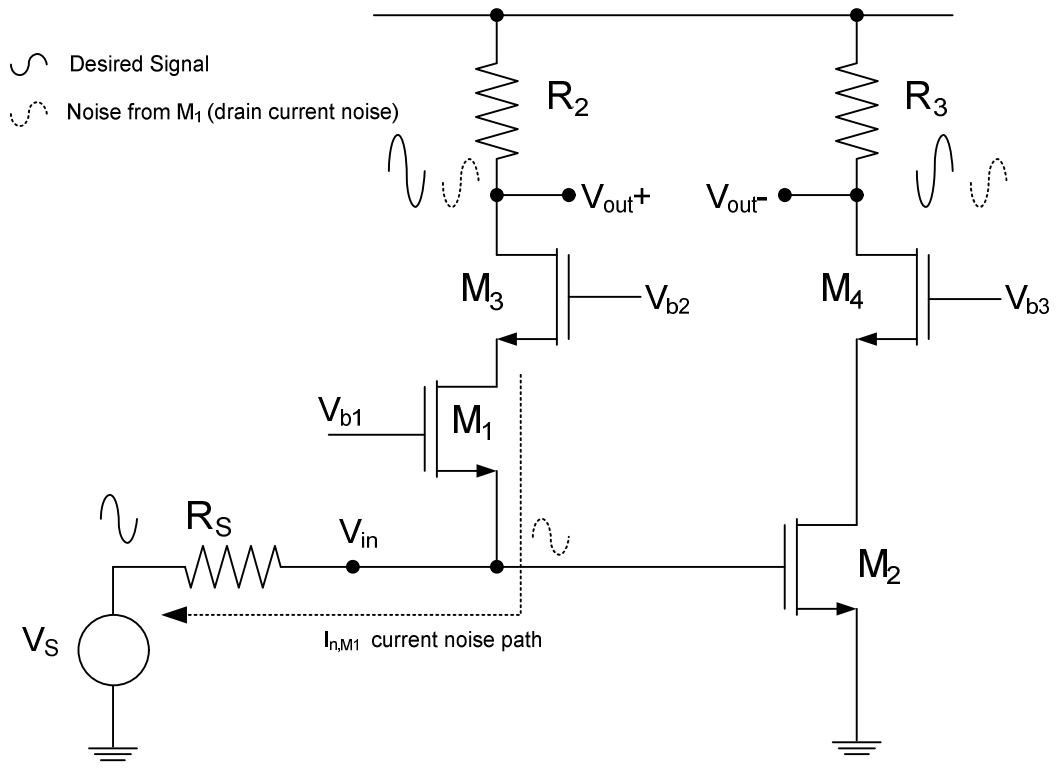

Figure 3.11 Common-gate common-source LNA input matching with noise-canceling

In contrast, the output noise due to the drain noise of M_1 is in the same phase at the drain of M_3 and the drain of M_4. When the output is taken differentially, these two particular noise voltages will cancel each other out. If the values of R_2, R_3, g_{m1} and g_{m2} are chosen carefully, the drain noise from M_1 can be substantially reduced. Since the dominant noise source in a traditional common-gate amplifier is the drain current noise of M_1, the input-referred noise of M_2 could be made low by increasing M_2's g_m without input matching constraints, and very low noise figure could be achieved.

A common-gate common-source thermal noise-cancelling architecture similar to the one in figure 3.12 could also be combined with non-linearity canceling architecture (the concepts of non-linearity cancellation will be discussed in chapter 7), as reported in [3.17]. In this work, the input is a complementary common-gate stage that incorporates both PMOS and NMOS to increase current efficiency. Bias voltages on the input devices, both common-gate and common-source stages, can be set to obtain both noise and nonlinearity cancellation simultaneously. Lastly, the output is taken single-ended by adding an extra common-source stage at the common-gate stage output and combining its output current to the current coming from the main common-source stage.

3.5.5 Inductive Source Degeneration

Unlike the previously discussed techniques, this matching topology provides a perfect match without adding any noise to the system or creating any restrictions on the device g_m. It uses an inductor as a source degeneration device and has another inductor connecting to the gate as shown in figure 3.12.

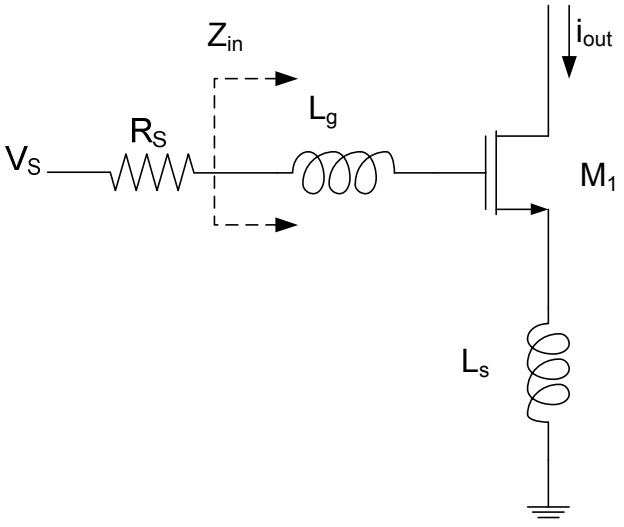

Figure 3.12 Inductive source degeneration matching

Using small signal analysis, and neglecting the gate resistance as well as the C_{gd} of M_1, the impedance looking through the gate inductor can be expressed as:

$$Z_{in} = j\omega(L_g + L_s) + \frac{1}{j\omega C_{gs}} + \omega_T L_s \tag{3.30}$$

$$\omega_T = \frac{g_m}{C_{gs}} \tag{3.30}$$

At the resonance frequency where the inductor impedance and the capacitor impedance are canceled out, the input impedance is the last term in the equation (3.30). The tuned impedance is then given by:

$$Z_{in}(\omega_0) = R_{eq} = \omega_T L_s \tag{3.31}$$

$$\omega_0 = \frac{1}{\sqrt{(L_g + L_s)C_{gs}}} \tag{3.32}$$

Since all the inductors are reactive, they do not add any noise into the circuit. In fact, the LC resonating mechanism improves noise and gain performance of the amplifier due to voltage gain from the resonance mechanism. Starting from the equivalent model of the input matching (figure 3.13), the quality factor of the circuit is given by:

$$Q = \frac{\omega C_{gs}}{R_{eq}} \tag{3.32}$$

At the resonance frequency, the voltage amplitude across the C_{gs} is Q times the voltage across the input terminal from the source, given a matched condition. This effectively increases the transconductance of the input transistor by a factor of Q.

$$G_m = Qg_m \tag{3.33}$$

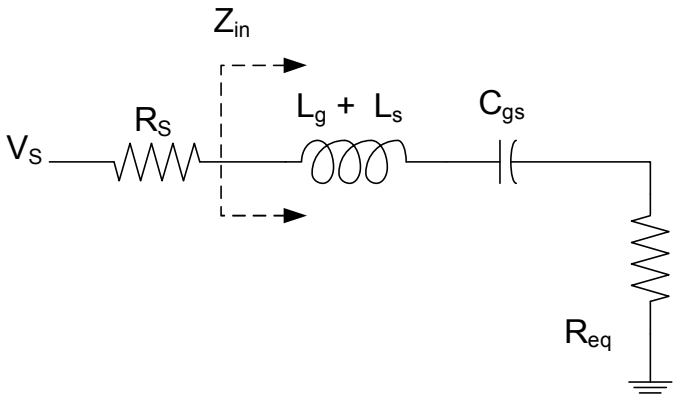

Figure 3.13 An equivalent circuit for the inductively degenerated input match

In typical narrow-band matching, this factor is usually around 2-5. Assuming that the matching network is lossless, this effect helps reduce the input-referred added noise by a factor of Q and increases the voltage gain of the circuit by the same factor. As a result, this topology is preferred in most narrow-band applications.

One major limitation of this topology is that the matching is narrow-band. As can be seen from equation 3.28, the input impedance is a series RLC network with finite Q. Since most wireless receivers are narrow-band, this is usually not a major concern. However, for broadband or multi-band receivers, achieving a very wide matching bandwidth requires the network to have very low Q, resulting in low gain and a poor noise figure of the LNA.

If the LNA is implemented in a deep-submicron CMOS process, C_{gs} of M_1 can be very small such that L_g could be too large to be implemented on-chip. To solve this problem, an extra degree of freedom could be added by placing an extra capacitor across the gate-source terminal of M_1 [3.18]. This extra capacitor is used to increase the effective capacitance into the gate of M1, resulting in a smaller required value of L_g for the same frequency of application. Unlike increasing the effective C_{gs} by directly increasing the size of M_1, this extra capacitor neither changes the amount of the intrinsic gate induced noise (3.2) nor increases C_{gd} and C_{db} of M_1.

3.6 References

[3.1] R. Lu, "CMOS Low Noise Amplifier Design for Wireless Sensor Networks," Master's Thesis, UC Berkeley, 2003.

[3.2] Y. Tsividis. *Operation and Modeling of the MOS transistor*. McGraw-Hill, Boston, 1998.

[3.3] A. Van Der Ziel. *Noise in Solid-State Devices and Circuits*. New York: Wiley, 1986.

[3.4] A. J. Scholten, et al., "Accurate Thermal Noise Model for Deep-Submicron CMOS*," IEEE International Electron Devices Meeting*, IEDM Technical Digest, pp. 155-158, Dec.1999.

[3.5] T. Lee. *The Design of CMOS Radio-Frequency Integrated Circuits*. Cambridge University Press, Cambridge, UK, 1998.

[3.6] P. R. Gray, R.G. Meyer, P. J. Hurst, and S. H. Lewis, *Analysis and Design of Analog Integrated Circuits,* Fourth Edition, Wiley, New York, 2001.

[3.7] J. Janssens and M. Steyaert. *CMOS Cellular Receiver Front-Ends*. Kluwer, The Netherlands, 2002.

[3.8] J. Zhan and S. Taylor, "A 5-GHz Resistive Feedback CMOS LNA for Low-Cost Multi-Standard Applications," in *IEEE Int. Solid-State Circuits Conf. Dig. Tech. Papers*, San Francisco, CA, Feb. 2006, pp. 721-730.

[3.9] Bevilacqua, M. Camponeschi, M. Tiebout, A. Gerosa, and A. Neviani, "Design of broadband inductorless LNAs in ultra-scaled CMOS technologies," in *IEEE International Symposium on Circuits and Systems*, Seattle, CA, May 2008, pp. 1300-1303.

[3.10] B. Perumana, J. Zhan, S. Taylor, B. Carlton, and J. Laskar, "Resistive Feedback Low-Noise Amplifiers for Multiband Applications," *IEEE Transactions on Microwave Theory and Techniques*," vol. 56, no. 5, May 2008, pp 1218-1225.

[3.11] S. Wang, A. Niknejad, and B. Brodersen, "Design of a Sub-mW 960 MHz UWB CMOS LNA," *IEEE J. Solid-State Circuits*, vol. 41, no. 11, Apr. 2006, pp. 2449-2456.

[3.12] A. Liscidini, M. Brandolini, D. Sanzogni, and R. Castello, "A 0.13 μm CMOS Front-End, for DCS1800/UMTS/802.11b-g With Multiband Positive Feedback Low-Noise Amplifier," *IEEE J. Solid-State Circuits*, vol. 41, no. 4, Apr. 2006, pp. 981-989.

[3.13] P. Rossi, A. Liscidini, M. Brandolini, and F. Svelto, "A Variable Gain RF Front-End, Based on Voltage-Voltage Feedback LNA, for Multi-Standard Applications," *IEEE J. Solid-State Circuits*, vol. 40, no. 3, Mar. 2005, pp. 690-697.

[3.14] A. Liscidini, M. Brandolini, P. Rossi, F. Torrisi, and F. Svelto, "Design methodology of feedback-LNAs for GHz applications," in *Proc. Bipolar/BiCMOS Circuits and Technology Meeting (BCTM)*, Sep. 2004, pp.253-256.

[3.15] F. Bruccoleri, E. Klumperink, and B. Nauta, "Wide-Band CMOS Low-Noise Amplifier Exploiting Thermal Noise Canceling," *IEEE J. Solid-State Circuits*, vol. 39, no. 2, Feb. 2004, pp. 275-282.

[3.16] S. Chehrazi, A. Mirzaei, R. Bagheri, and A. Abidi, "A 6.5 GHz wideband CMOS low noise amplifier for multi-band use," in *Proc. IEEE Custom Integrated Circuits Conf.*, Sep. 2005, pp. 801–804.

[3.17] W. Chen, G. Liu, Z. Boos, and A. Niknejad, "A Highly Linear Broadband CMOS LNA Employing Noise and Distortion Cancellation," *IEEE J. Solid-State Circuits*, vol. 43, no. 5, May 2008, pp. 1164-1175.

[3.18] T. Nguyen, C. Kim, G. Ihm, M. Yang, and S. Lee, "CMOS Low Noise Amplifier Design Optimization Techniques," *IEEE Trans. on Microwave Theory and Techniques,* vol. 52, no. 5, May 2004, pp. 1433-1442.

4

Broadband CMOS LNA Analysis and Design

4.1 Introduction

As discussed in chapter 2, a broadband low-noise amplifier (LNA) is an essential building block for all of the mentioned multi-band receiver front-end architectures. This chapter will review the design of such an LNA using a multi-section input matching network as presented in [4.1]. Starting with topology reviews, we will proceed through design considerations and implementation. Finally, experimental results will be presented.

4.2 Multi-Section Input Matching

Most LNAs now in use for integrated wireless receivers are narrow-band, and each is optimized for only one frequency band of operation. The design methodology for these LNAs is straightforward, and most are designed using an inductively degenerated topology that delivers both noise and power match at the same time [4.2].

To broaden the bandwidth of the input matching and gain, we could use the multi-section input matching topology, which is a modified version of the inductively degenerated LNA [4.1][4.3][4.4].

Figure 4.1 shows a generalized schematic of the broadband input matching topology, where N is the number of input stages. Please note that the external C_p is added between the gate and source of M_1 in order to increase the degree of freedom in the design.

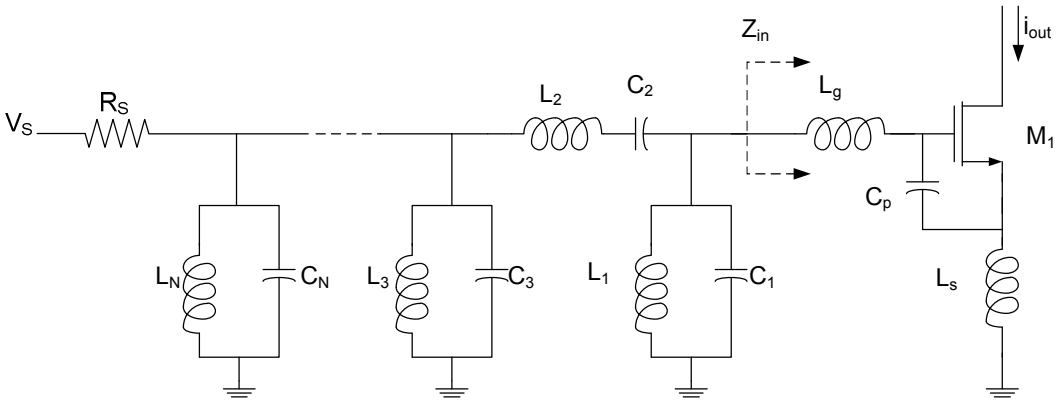

Figure 4.1 A generalized schematic of the multi-stage input matching topology

Using (3.24), and ignoring the effect of C_{gd}, the input impedance of the LNA excluding L_n's and C_n's is given by:

$$Z_{in} = sL_g + \frac{1}{sC_t} + \frac{g_m L_s}{C_t} = sL_g + \frac{1}{sC_t} + R_T \tag{4.1}$$

where

$$C_t = C_p + C_{gs} \tag{4.2}$$

Combining Z_{in} with L_n's and C_n's, we get the equivalent circuit for the input impedance, as shown in figure 4.2. The impedance Z_{in} and the entire L_n's and C_n's form a bandpass filter with the termination resistor R_T. If we look at the inductive degeneration

topology as a first-order filter, the addition of L_n's and C_n's effectively increases the order of the filter beyond first-order. From filter theory [4.5], it is easier to get high bandwidth from a higher-order filter than from a lower-order filter, given the same or comparable component values and quality factor. This makes wideband matching feasible for multi-stage input matching.

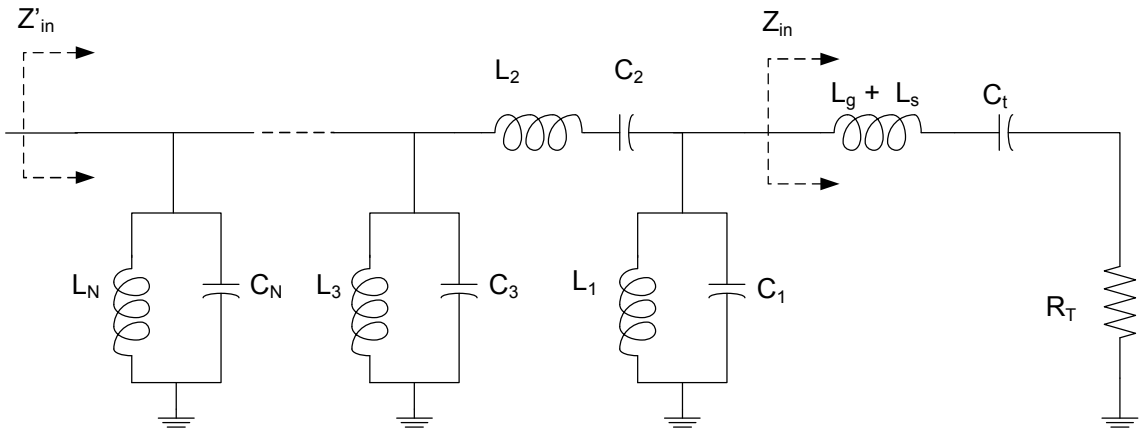

Figure 4.2 Equivalent input impedance of the multi-section input matching

4.2.1 Input Matching

In order to get an input match, the real part of the input impedance (Z'_{in}) must be equal or close to the source impedance R_S. If $R_T = \omega_T L_s = R_S$ and the filter has 0 dB gain with a ripple of ρ_r (note that ρ_r is defined so that 0 dB ripple means $\rho_r = 1$), the input reflection coefficient can be related to the ripple by [4.3]:

$$\left|\Gamma_{in}\right|^2 = \left|1 - \frac{1}{\rho_r^2}\right| \tag{4.2}$$

In the matched condition, the power delivered into the load R_T must be the same as the amount power delivered to the load as if Z_{in} is simply a resistor $R_{in} = R_S$, which we call the available power. If the power delivered to the load is less than this available power, the input matching is then not perfected and it is considered that a portion of the available power is reflected. The reflection coefficient is then simply the ratio between the reflected power and the power available to the load, as expressed in (4.2).

For a numerical example, we need to have $0.953 \leq \rho_r$ (about 0.46 dB) for an input matching of –10 dB or better. This translates to less than 0.46 dB gain variation in the passband. The plot between passband ripple and the reflection coefficient (both in dB) is shown in figure 4.3. Once the input matching requirement is chosen, the reactive element values for any given bandwidth and matching specifications can be obtained by using a well-established LC filter design methodology as presented in [4.5] and [4.6].

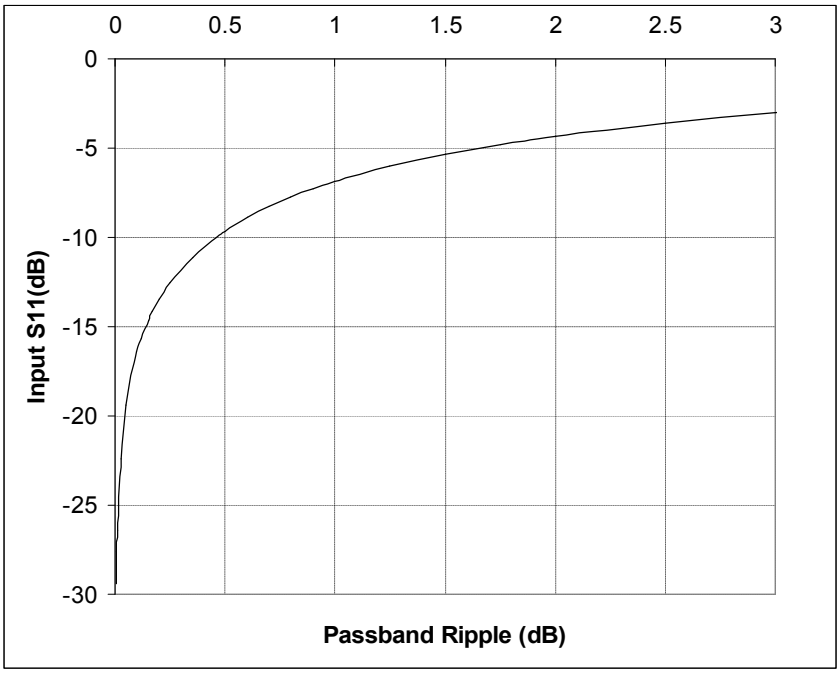

Figure 4.3 Relationship between passband ripple and reflection coefficient (S_{11})

4.2.2 Effective Transconductance

The effective g_m depends on the device g_m and the voltage transfer function from the input terminal to the v_{gs} at the device terminal. Assuming the transfer function of the filter is $W(j\omega)$, the current flowing into the gate of M_1 is then given by [4.3]:

$$i_{M_1,in} = \frac{v_{in}}{R_T} W(j\omega) \tag{4.3}$$

where v_{in} is the terminal voltage as shown in figure 4.2. In the passband, $W(j\omega)$ is approximately unity and the current is simply the terminal voltage divided by R_T. However, $W(j\omega)$ becomes very small out-of-band, and in this case the current transfer

function is minimal. The v_{gs} of M_1 can be found directly by multiplying the gate current to the impedance from C_{gs}:

$$v_{gs} = \frac{i_{M1,in}}{j\omega C_t} = \frac{v_{in}}{R_T}\frac{W(j\omega)}{j\omega C_t} \tag{4.4}$$

Using (4.4), the effective transconductance is:

$$G_m(j\omega) = g_m \frac{v_{gs}}{v_{in}} = \frac{g_m W(j\omega)}{j\omega R_T C_t} \tag{4.5}$$

If only the magnitude of G_m is concerned, (4.5) can be simplified to:

$$|G_m(j\omega)| = g_m Q |W(j\omega)| \tag{4.6}$$

The expressions in equations 4.5 and 4.6 are generalizations of (3.24) in the previous chapter. As shown above, the effective G_m of the circuit depends strongly on the Q of the matching network. For an on-chip implementation, this value is limited by either the practical values of the inductors or parasitic capacitances on the input transistor.

4.2.3 Noise Analysis

There are several major sources of noise for a multi-section input matching LAN. The first is loss at the input-matching network due to finite Q of the passive components, mainly from the input inductors. The other noise sources are the thermal drain and gate current noises of the input device (M_1 in figure 4.1). The optimal device size based on a given bias current for a narrow-band case is given in [4.2].

To see the effect of noise from the transistor in a wideband-matching case, we will follow the analysis in [4.3]. The input transistor with the degeneration inductor is shown in figure 4.4a along with its gate and drain current noises, and the noise sources can be replaced by input referred voltage and current noise sources given by:

$$i_n = i_{ng} + \frac{j\omega C_t}{g_m} i_{nd} \tag{4.7}$$

$$v_n = j\omega L_s i_{ng} + \left(1 - \omega^2 C_t L_s\right)\frac{i_{nd}}{g_m} = \frac{i_{id}}{g_m} + j\omega L_s i_n \tag{4.8}$$

where i_{nd} and i_{ng} are the drain current noise and the gate current noise, respectively. The spectrum densities of these two current noises were discussed in the previous chapter and given as follows:

$$\overline{i_{nd}^2} = 4kT\gamma g_{d0}\Delta f \tag{4.9}$$

$$\overline{i_{ng}^2} = 4kT\delta\frac{\omega^2 C_{gs}^2}{5g_{d0}}\Delta f \tag{4.10}$$

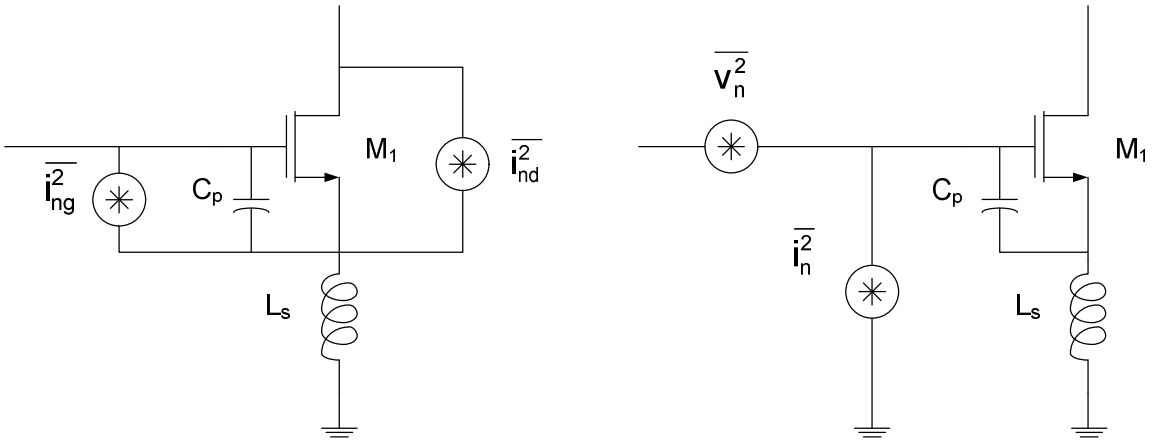

(a) (b)

Figure 4.4 Drain and gate current noise models

These two noises are correlated with a correlation coefficient of approximately j0.4. This means that the correlation admittance has only the imaginary part and is given by [4.3]:

$$Y_c = \frac{i_n}{v_n} = G_c + jB_c = jB_c = \frac{j\omega C_t}{\dfrac{1+|c|\rho\alpha\chi}{1+2|c|\rho\alpha\chi+\rho^2\alpha^2\chi^2} - \omega^2 L_s C_t} \tag{4.11}$$

where $\rho = C_{gs}/C_t$, $\chi = \sqrt{\delta/(5\gamma)}$, and c is the correlation coefficient between i_{ng} and i_{nd}. The parameter $\alpha = g_m/g_{d0}$ accounts for short-channel effects due to velocity saturation and decreasing mobility [4.1][4.5].

The optimal source admittance is then given by [4.2]:

$$G_{opt} = \sqrt{\frac{G_u}{R_n} + G_c^2} = \sqrt{\frac{G_u}{R_n}} = \frac{\omega C_t \left(1 + 2|c|\rho\alpha\chi + \rho^2\alpha^2\chi^2\right)}{\rho\alpha\chi\sqrt{1-|c|^2}} \tag{4.12}$$

$$B_{opt} = -B_c = \frac{\omega C_t}{\omega^2 L_s C_t - \dfrac{1+|c|\rho\alpha\chi}{1+2|c|\rho\alpha\chi+\rho^2\alpha^2\chi^2}} \tag{4.13}$$

Equation (4.13) shows that the optimal admittance (or impedance) is approximately the same as the one that resonates with the series combination of C_t and L_s. This means that a nearly minimum noise figure can be obtained over the wide bandwidth by using the multi-section matching network, and the corresponding noise factor is given by:

$$F \approx 1 + \frac{1}{G_u R_s} + \frac{R_s}{R_n} = 1 + \frac{P(\omega)}{g_m R_s}\frac{\gamma}{\alpha} \tag{4.14}$$

where

$$P(\omega) = \frac{\rho^2\alpha^2\chi^2\left(1-|c|^2\right)}{1+2|c|\rho\alpha\chi+\rho^2\alpha^2\chi^2} + \omega^2 C_t^2 R_s^2\left(1+2|c|\rho\alpha\chi+\rho^2\alpha^2\chi^2\right) \tag{4.15}$$

As seen from equations (4.14) and (4.15), the noise figure depends on frequency, device g_m, C_t, and other process parameters. For a given bias current, there is an optimal device size to obtain the minimum noise figure for single frequency.

As mentioned previously, there are other sources of noise such as loss at the input-matching network, physical gate resistance, and substrate resistance. All of these noise sources must be considered together when designing the circuit. The total noise figure is then expected to be worse than that given in the equation (4.14).

4.3 0.8-2.4 GHz Broadband LNA Design

Having discussed the matching topology, we now turn to the LNA circuit implementation. The simplified schematic of the LNA is shown in figure 4.5. It consists of the main (first) stage and the buffer (second) stage for output matching purposes. Note that the second stage is added for measurement purposes only and could be eliminated if this LNA had an on-chip interface with mixers.

4.3.1 First Stage Design

Because adding inductors for input matching degrades noise performance due to the inductors' lossy property, the minimal number of stages is preferred as long as the required bandwidth can be achieved with reasonable passive component values. In this case, only two stages are required to keep the inductor value below 10 nH, which is the value chosen based on available models and inductor *Q*. The output of the first stage is a low-*Q* tuned circuit with center frequency around mid-band. Using a tuned load reduces out-of-band interferences and noise, while the low-*Q* property ensures broadband operation.

The size of M_1 is determined experimentally by gain, noise, and linearity requirements [4.1]. The chosen value is W/L = 480/0.18 with 16 mA of bias current.

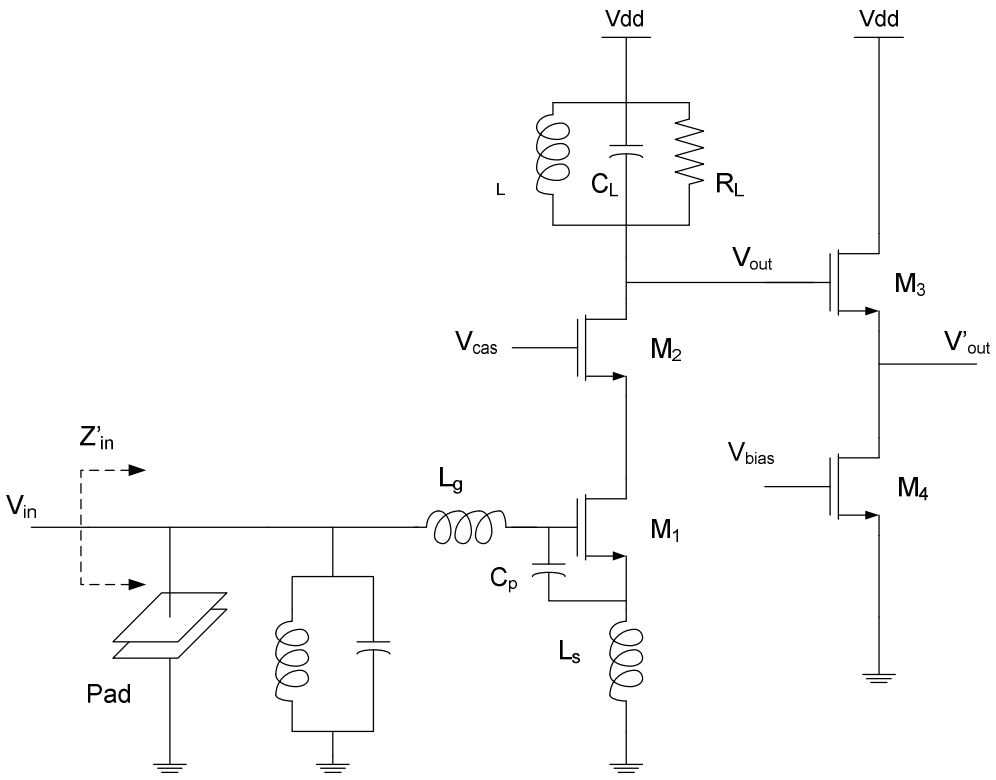

Figure 4.5 Broadband LNA topology using 2-section input matching

Combining Z_{in} with L_1 and C_1, we get the equivalent circuit for the input impedance as shown in figure 4.6.

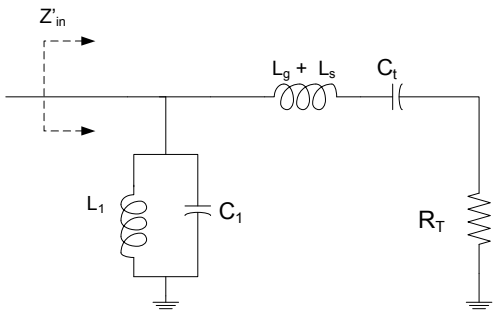

Figure 4.6 Equivalent circuit for input impedance

The values of L_1, C_l, L_g and Ct can be obtained from the standard filter synthesis table [4.5].

We have chosen the Chevbyshev topology as the design starting point since it provides steeper transition band edges. Note that the bandwidth is from 0.8 GHz to 2.4 GHz with center frequency of $\sqrt{(0.8\text{GHz})(2.4\text{GHz})} \approx 1.4$ GHz. In practice, parasitic capacitance of L_1, L_g, and the input pads increases the effective value of C_1. After extensive simulations, the final numbers for the components are: L_s=1.31 nH, L_1= 9.6 nH, C_1= 400 fF (there is about 1 pF of parasitic capacitance from L_1 in parallel to C_1), L_g= 5.52 nH, and C_g= 850 fF.

The cascode device (M_2) is chosen to be as small as possible to reduce the parasitic capacitances. The voltage headroom as well as the cascode transistor noise contributions set the lower bound on the size. The chosen size is W/L = 120/0.18, exactly one-quarter the size of M_1.

The output of the first stage is chosen to be a low-Q tuned circuit. The load is low-Q tuned in order to suppress out-of-band interference and to reduce the gain variations within the operating frequencies. The value of R_L is chosen to be 300 Ω, and the –3 dB gain frequency band ranges from 800 MHz to 2.4 GHz.

4.3.2 Second Stage Design

The second stage is a simple source follower added for output matching. The output impedance of this stage is $1/g_m$ and has been set to 50 Ω, which is the external load impedance during measurement. The measured output voltage (V'_{out}), when driving a

50 Ω load is 6 dB less than the output voltage from the core amplifier (V_{out}). When designing an LNA with a mixer, V_{out} is the output voltage that drives the mixer input. The device M_3 is designed with minimum channel length in order to minimize the associated parasitic capacitances. The bias current of this stage is 10 mA.

4.4 Experimental Results

The circuit has been designed and fabricated in the IBM 0.18 μm technology. The LNA die microphotograph is shown in figure 4.7, and the total chip area is approximately 1.9 mm^2 (1.3 mm x 1.5 mm). The input is on the left, the output is on the right, and both are AC-coupled. Inductors are placed as far from each other as possible given the available area in order to reduce parasitic mutual coupling. In addition, the bias lines are shielded with ground and routed in such a way as to minimize the distances from them to the inductors.

The s-parameters, noise figure, and IIP_3 of the LNA were measured with a Cascade 9000 probing system. The measurements cover from 0.8 GHz to 2.4 GHz. All cable losses are compensated either by calibration (for s-parameters) or subtraction (for NF and IIP_3 measurements).

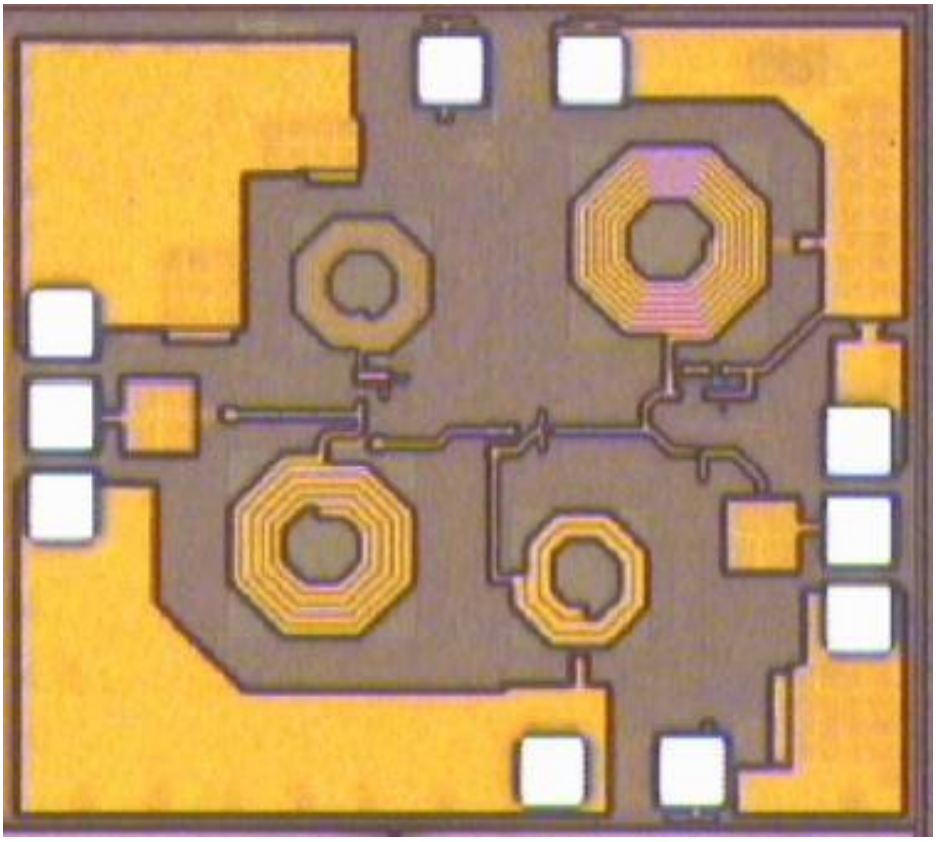

Figure 4.7 LNA die microphotograph (1.3 mm x 1.5 mm)

4.4.1 S_{11}

S_{11} plots at different bias currents are shown in figure 4.8. It is clear from the figure that the -10 dB matching is achieved over the wide range of frequencies and bias currents.

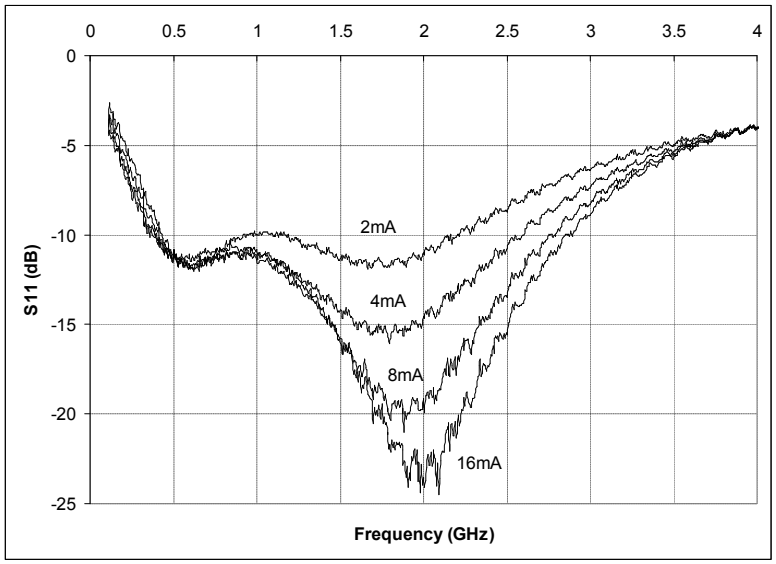

Figure 4.8 Measured S_{11} plots for different bias currents

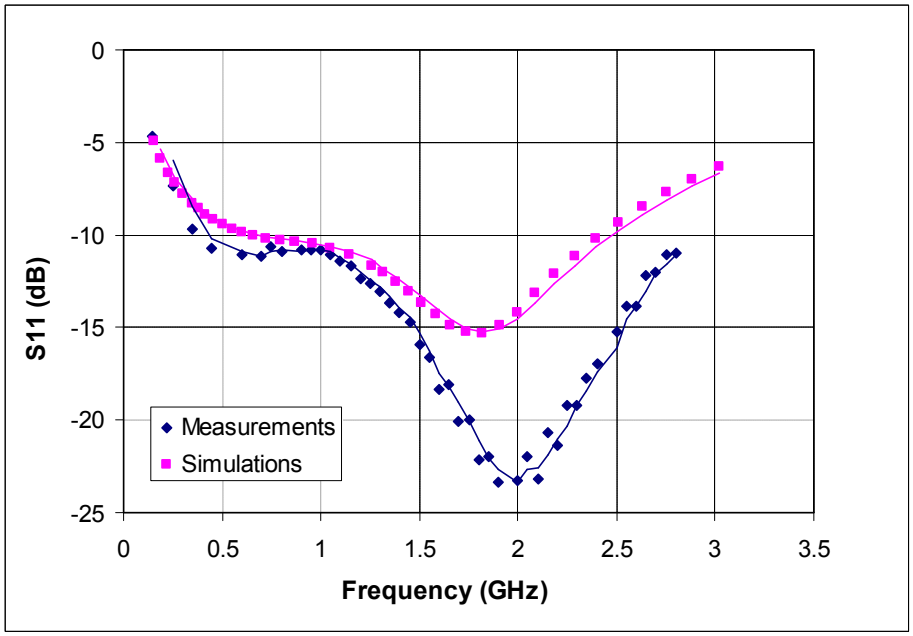

Figure 4.9 Measured and simulated S_{11} at 16mA bias current

As a comparison, figure 4.9 shows the S_{11} plots from simulation and measurements in the same graph for I_d=16 mA. They are slightly off-tuned, nonetheless

the plots share the same trend. Since the matching is dominated by the passive elements at the input, the discrepancies most likely come from parasitic components associated with the inaccuracy of the layout modeling and simulations.

4.4.2 S_{21}

Like S_{11}, S_{21} plots at different bias currents are shown in figure 4.10. The peak gain is around 17 dB at 1.5 GHz with 16 mA bias current. In this case, the -3dB bandwidth is approximately from 1 GHz to 2 GHz. As the bias current changes from 2 mA to 16 mA, S_{21} changes by approximately 5 dB. This means we can trade off some sensitivity with bias current in dynamic operations.

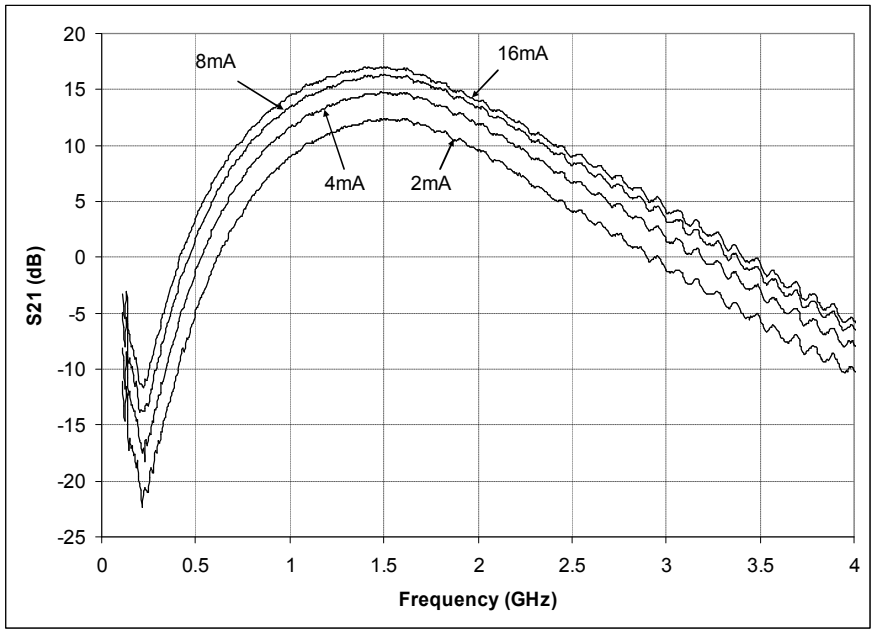

Figure 4.10 S_{21} plots for different bias currents

In addition, the S_{21} plots from simulation and the measurement at 16 mA bias current are shown on the same graph in figure 4.11. The measured S_{21} is off by about 1 dB from the simulations at the peak but matches well with the simulations.

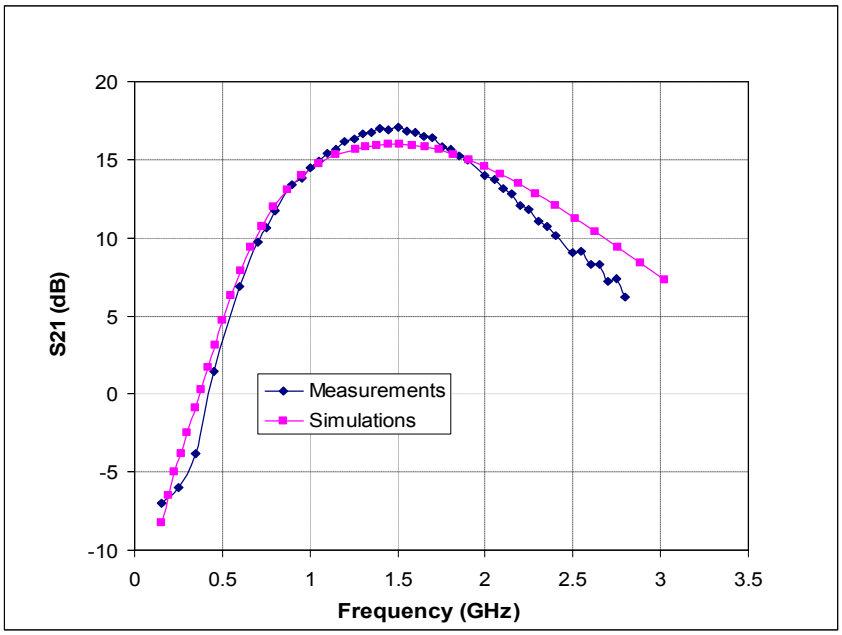

Figure 4.11 Comparisons between measurements and simulations of S_{21} at 16mA

4.4.3 S_{12} and S_{22}

S_{12} has been measured and is between 40 dB and 50 dB from 0.8 GHz to 2.4 GHz. It does not depend on the bias current and only weakly depends on the frequency.

The measured S_{22} is better than -10 dB from 0.8 GHz to 2.4 GHz. The buffer current is fixed at 10 mA for all the measurements, and this makes S_{22} almost independent of the main stage bias condition. According to the data, we can then assume that 6 dB loss occurs at the buffer stage, and the first-stage gain is higher than the overall gain by the same amount.

4.4.4 Noise Figure

The noise measurements were done using a noise figure meter in conjunction with the probe station. Since the measurement cable is lossy, the measured noise figure number must be subtracted by the input cable attenuation. The measurement setup is shown in figure 4.12.

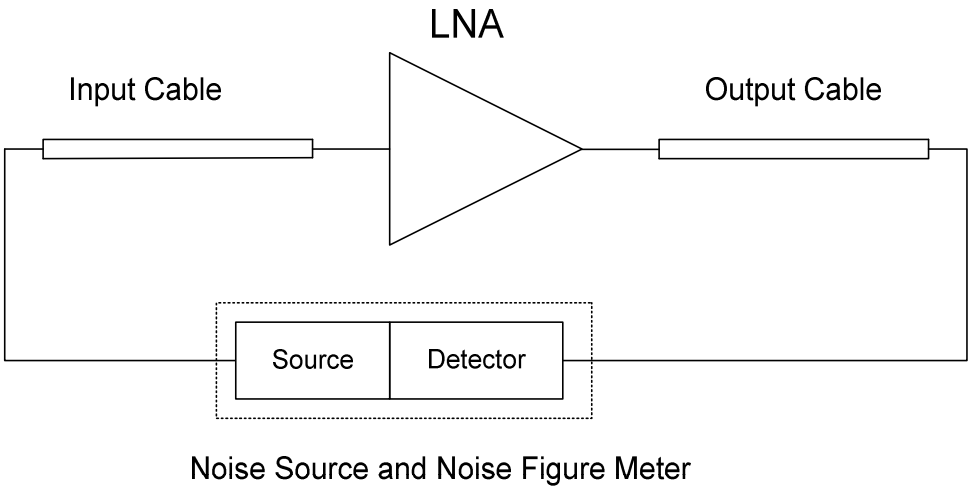

Figure 4.12 Noise measurement setup

If the loss at the output is small, the LNA noise figure can be estimated as follows

$$NF_{LNA}(dB) = NF_{measured}(dB) - L_{cable}(dB) \tag{4.16}$$

Where L_{cable} is the input cable loss. The de-embedded noise measurement results are shown in figure 4.13a-d. In addition, comparisons between the simulated and measured noise figures are shown in figure 4.14.

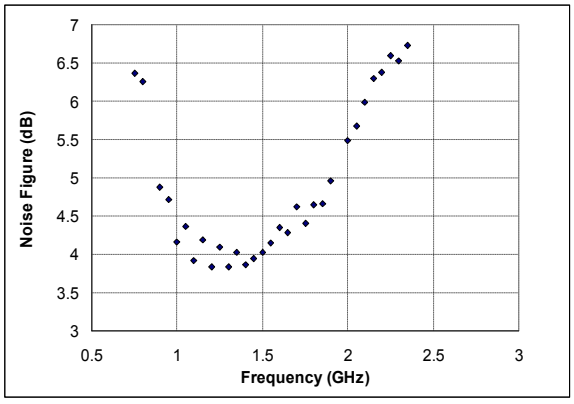

Figure 4.13a I_d = 2 mA

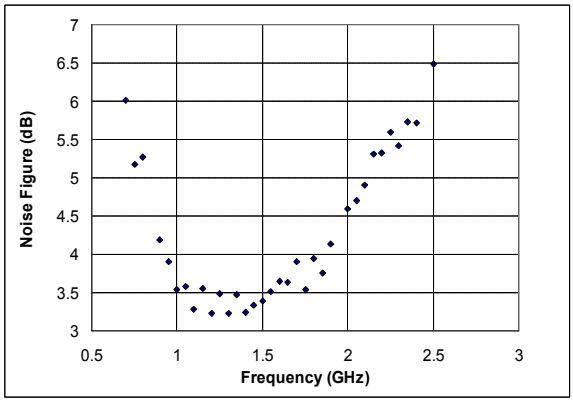

Figure 4.13b I_d = 4 mA

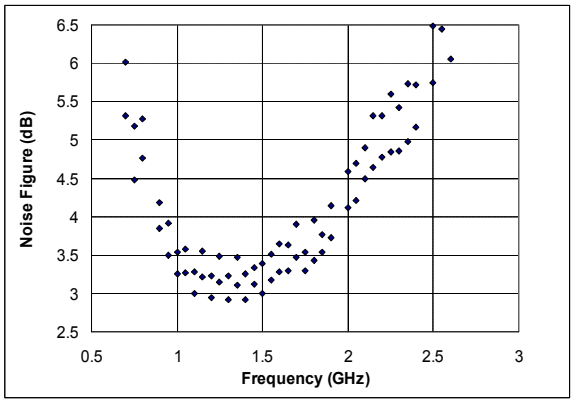

Figure 4.13c I_d = 8 mA

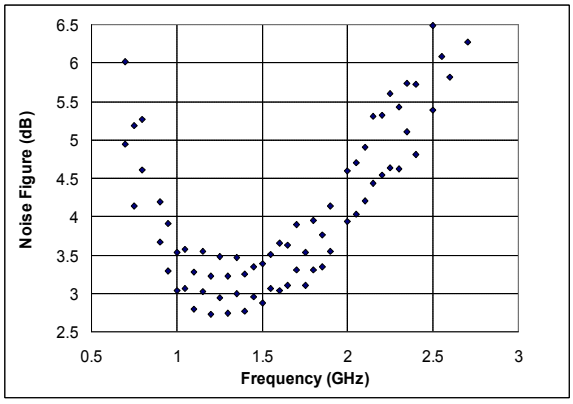

Figure 4.13d I_d = 16 mA

Figure 4.13 NF plots for different bias currents

As shown in the plots, the minimum measured noise figure is approximately 2.7 dB at around 1.2 GHz and 16 mA bias current. For the same bias condition, noise figure is below 4 dB between 0.8 GHz and 2 GHz and is around 5 dB at 2.4 GHz. It is expected that noise performance will get worse when bias current is reduced. At 2 mA bias, the minimum NF is around 4 dB.

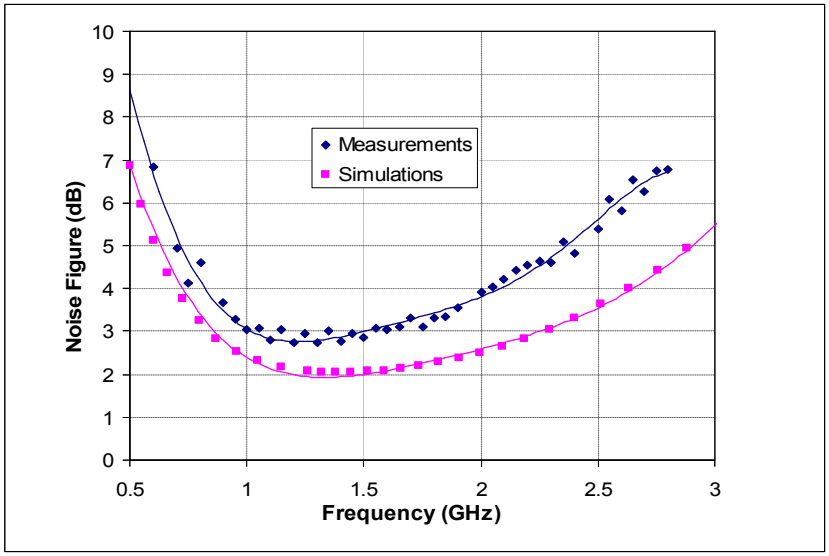

Figure 4.14 Comparison between measured and simulated NF at 16mA

The measured noise figure is around 0.5 dB to 1 dB higher than in the simulations. Since the induced gate noise is not included in the device model in simulations, it is likely a cause of discrepancies. This can be fixed by manually adding the gate-induced noise into the model as suggested in [4.3].

4.4.5 IIP_3

The input IP_3 of the LNA was measured using the two-tone inputs method. The frequencies of the test signals are 1.5 GHz and 1.501 GHz, which are around the mid-band of the LNA. The measurement results are plotted against bias current in figure 4.15 for different bias currents. The measured IIP_3 values are between 0 and -3 dBm for bias currents from 2 mA to 16 mA. In addition, the simulated IIP_3 numbers are shown in the same graph as a comparison.

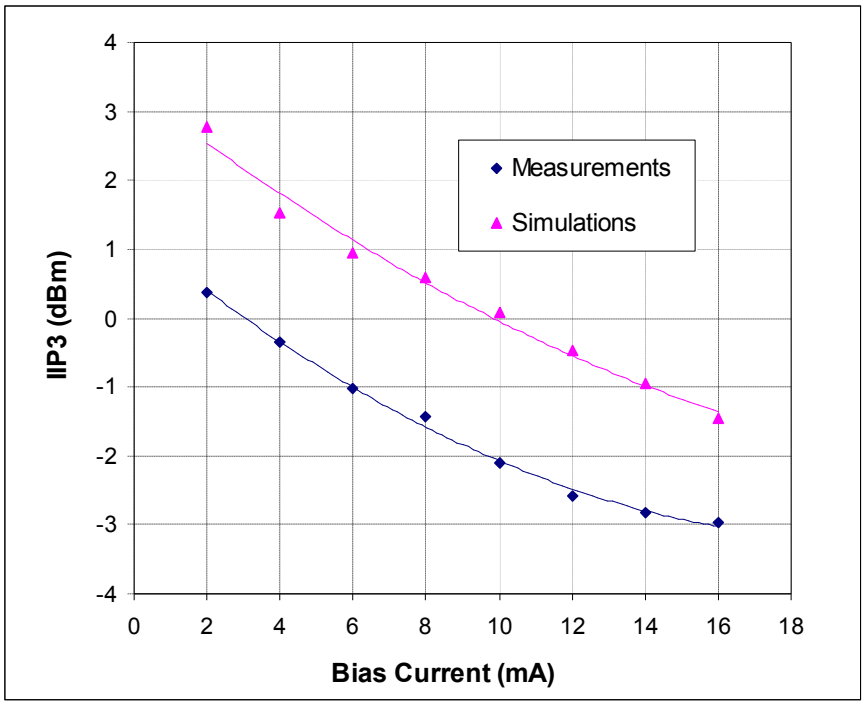

Figure 4.15 LNA IIP_3 plots

Since the IIP_3 of the buffer stage is fixed, the overall IIP_3 is inversely proportional to the gain at the first stage. The measured IIP_3 is approximately 2 dB lower than the numbers from the simulations. The discrepancy is likely due to gain differences in the first stage, which is suggested by the differences in overall gain of the circuit The IIP_3 decreases as bias current increases because it is limited by the nonlinearity of the buffer stage.

4.4.6 Dynamic Performance

An interesting aspect of the LNA is the dynamic operation, or how the performance metrics change with the bias current. As we can see from figure 4.8, the S_{11}

of the LNA stays below –10 dB for bias current from 2 mA to 16 mA in the band of interest (0.8 GHz to 2.4 GHz). This means that we can vary the bias current and adjust the performance without violating the matching requirement. For example, figure 4.16 shows plots of LNA gain and noise figure as a function of bias current at 1.5 GHz are shown. From the plots, it is clear that we can nicely trade the performance with current consumption.

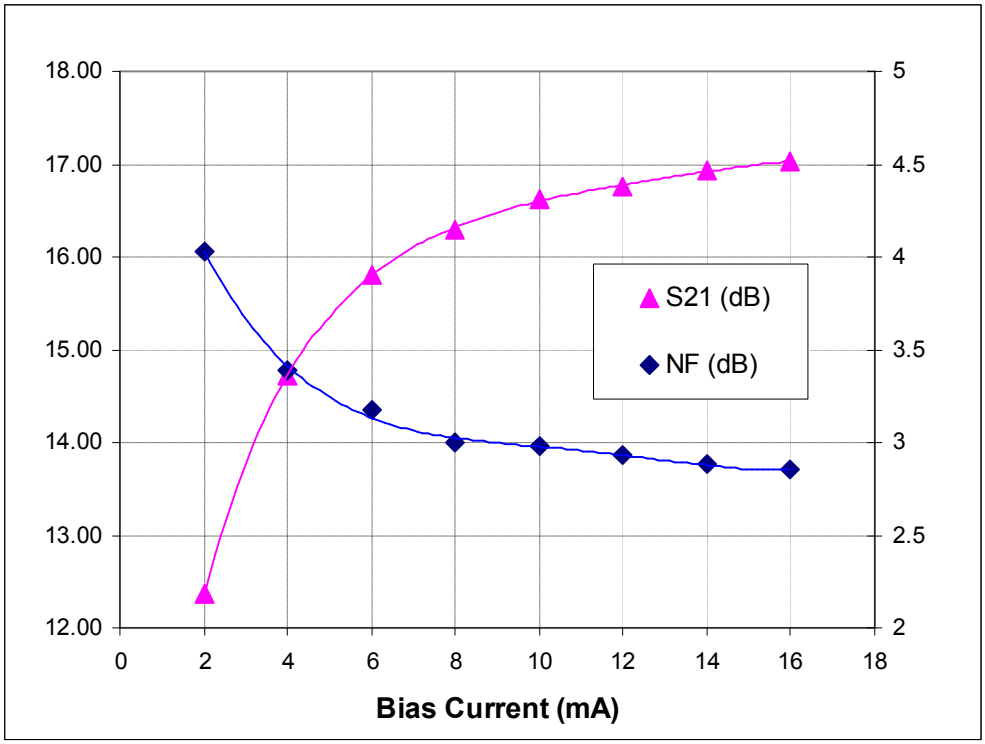

Figure 4.16 LNA Dynamic Characteristics

4.5 References

[4.1] N. Poobuapheun, "A Prototype Broadband CMOS LNA for Universal Radio Receivers," Master's Thesis, UC Berkeley, 2005.

[4.2] T. H. Lee. *The Design of CMOS Radio-Frequency Integrated Circuits*. Cambridge University Press, 1998.

[4.3] A. Bevilacqua and A. M. Niknejad, "*An Ultra Wideband CMOS Low Noise Amplifier for 3.1-10.6 GHz Wireless Receivers,*" IEEE J. Solid-State Circuits, vol. 39, no. 12,pp. 2259-2268, December 2004.

[4.4] A. Ismail and A. Adibi, "*A 3-10-GHz Low Noise Amplifier with Wideband LC-Ladder Matching Network,*" IEEE J. Solid-State Circuits, vol. 39, no. 12, pp. 2269-2277, December 2004.

[4.5] R. Schaumann and M. E. V. Valkenburg. *Design of Analog Filters*. Oxford University Press, New York, 2001.

[4.6] G. Matthaei, L. Young, and E. M. T. Jones. *Microwave Filters, Impedance-Matching Networks, and Coupling Structures*. McGraw-Hill, New York, 1964.

[4.7] P. R. Gray, R.G. Meyer, P. J. Hurst, and S. H. Lewis. *Analysis and Design of Analog Integrated Circuits,* Fourth Edition, Wiley, New York, 2001.

[4.8] B.E. Boser. *EE240 Lecture Notes*. University of California, Berkeley, 2003.

5

CMOS Mixer Fundamentals

5.1 Introduction

The mixer is one the most important blocks in virtually all wireless receivers. As discussed in chapter 2, most wireless transmission is narrow-band, and the information is located within a certain bandwidth around the carrier frequency. The primary function of a mixer is to perform frequency translation of the signal between the carrier frequency and baseband. The mixer's performance strongly affects the overall performance of the receiver, and it is a major component in the receiver front-end.

In section 5.2 we will review mixer fundamentals. Section 5.3 covers the performance metrics of a basic mixer. We will then review mixer architectures in section 5.4, and section 5.5 will discuss quadrature signal generation, which is important in receiver designs for modern communication systems. Finally, we will present a brief survey of mixers for multi-band multi-standard front-ends.

5.2 Mixer Basics

The mixer is a nonlinear device that performs frequency translation by creating multiplication terms between the two signals. It has two inputs, called radio frequency (RF) and local oscillator (LO) ports. The RF port senses the signal to be downconverted, while the LO port senses a static periodic signal coming from local oscillator generation

circuitry [5.1]. The output port of the mixer is called IF (intermediate frequency), or is sometimes called BB (baseband) if the mixer is used for direct downconversion. Figure 5.1 shows a symbol representation of a mixer along with its input and output.

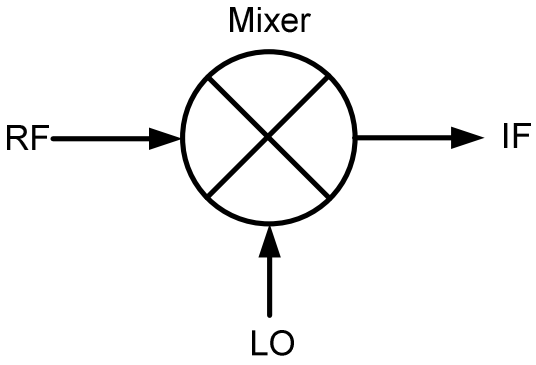

Figure 5.1 Symbol representation of a mixer

In time domain, we can write the relationship between the RF, LO, and IF signals as:

$$v_{IF}(t) = v_{RF}(t) \times v_{LO}(t) \tag{5.1}$$

Since the LO signal does not have to be perfectly sinusoidal, and can be any static periodic waveform, we can write the LO signal as a Fourier series containing higher-order harmonics. In this case, (5.1) becomes:

$$v_{IF}(t) = v_{RF}(t) \times \left(A_0 + A_1 \cos(\omega_{LO} t) + A_2 \cos(2\omega_{LO} t) + A_3 \cos(3\omega_{LO} t) + \ldots\right) \tag{5.2}$$

In narrow-band systems, the signal from the RF port is centered around a fixed carrier frequency, ω_{RF}, and can be modeled as

$$v_{RF}(t) = A_{RF}(t)\cos(\omega_{RF} t) \tag{5.3}$$

$A_{RF}(t)$ is time-varying and contains information being transmitted from the source which the receiver is intended to detect. For narrow-band transmissions, where the bandwidth of data is much lower than the carrier frequency, $A_{RF}(t)$ is considered an "envelope" of the signal. Placing (5.3) into (5.2) above, we get:

$$\begin{aligned} v_{IF}(t) = {} & A_{RF}(t)\cos(\omega_{RF}t)A_0 + A_{RF}(t)\cos(\omega_{RF}t)A_1\cos(\omega_{LO}t) + \\ & A_{RF}(t)\cos(\omega_{RF}t)A_2\cos(2\omega_{LO}t) + A_{RF}(t)\cos(\omega_{RF}t)A_3\cos(3\omega_{LO}t) + \ldots \end{aligned} \tag{5.4}$$

After algebraic manipulation of the sinusoidal multiplication terms, $v_{IF}(t)$ can then be written as:

$$\begin{aligned} v_{IF}(t) = {} & A_0 A_{RF}(t)\cos(\omega_{RF}t)A_0 \\ & + \frac{1}{2}A_1 A_{RF}(t)\cos((\omega_{LO}-\omega_{RF})t) + \frac{1}{2}A_1 A_{RF}(t)\cos((\omega_{LO}+\omega_{RF})t) \\ & + \frac{1}{2}A_2 A_{RF}(t)\cos((2\omega_{LO}-\omega_{RF})t) + \frac{1}{2}A_2 A_{RF}(t)\cos((2\omega_{LO}+\omega_{RF})t) \\ & + \frac{1}{2}A_3 A_{RF}(t)\cos((3\omega_{LO}-\omega_{RF})t) + \frac{1}{2}A_3 A_{RF}(t)\cos((3\omega_{LO}+\omega_{RF})t) \\ & + \ldots \end{aligned} \tag{5.5}$$

The equation above shows that the output $v_{IF}(t)$ has components located at ω_{RF}, $\omega_{LO} \pm \omega_{RF}$, $2\omega_{LO} \pm \omega_{RF}, 3\omega_{LO} \pm \omega_{RF}$, etc., in the frequency domain. In typical downconversion mixer circuits, among all the A_n coefficients, A_0 and A_1 are the highest and provide the greatest gain in the frequency translation process. Since ω_{RF} is simply a direct feed-through term without any frequency translation, the first-order term at

$\omega_{LO} - \omega_{RF}$ is then considered the output term in most applications. If this is the case, all the other terms are considered unwanted and will need to be filtered in the receiver chain.

5.3 Mixer Performance Metrics

5.3.1 Conversion Gain

The conversion gain of a mixer is the ratio between the output level of the component of interest (in many cases, at $\omega_{LO} - \omega_{RF}$) versus the input level at ω_{RF}. Conversion gain can be defined as either voltage or power conversion gain.

From (5.5), if the output frequency is $\omega_{LO} - \omega_{RF}$, the voltage conversion gain is:

$$CG = \frac{\frac{1}{2} A_1 A_{RF}(t)}{A_{RF}(t)} = \frac{1}{2} A_1 \tag{5.6}$$

CG is the voltage (or current) conversion gain of the mixer. The "power conversion gain" of the mixer is defined as the IF power delivered to the load, divided by the RF power going into the mixer input port. The magnitude of the power conversion gain is proportional to the square of the voltage conversion gain. If the input impedance of the mixer is the same as the load impedance, then the power conversion gain is the same as the voltage conversion gain. However, if the impedances are not equal, the power conversion gain will be different from the voltage conversion gain, and care must be taken to avoid confusion when calculating the performance of cascade stages employing a mixer [5.1].

5.3.2 Noise Figure

The noise figure of mixers is often a source of confusion due to the various available noise definitions, such as single-sideband noise figure (SSB NF) and double-sideband noise figure (DSB NF) [5.1]. For simplicity, let us first consider the noise situation in an ideal "noiseless mixer" with the power conversion gain CG_P and the LO port signal only at ω_{LO} (figure 5.2). Consider the case where the incoming signal at the RF port has power S_{in} and noise power per unit signal bandwidth N_{in}.

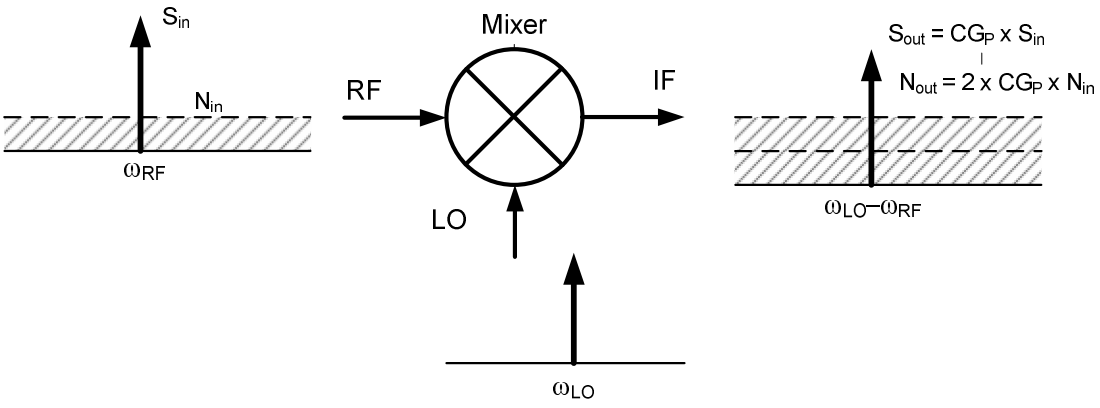

Figure 5.2 Signal and noise mechanism in a mixer

If the signal is located only at one side of ω_{LO} (only at ω_{RF}), and noise spectral density is flat over the bandwidth, the output signal and noise power will be:

$$S_{out} = CG_P \times S_{in} \tag{5.7}$$

$$N_{out} = 2 \times CG_P \times N_{in} \tag{5.8}$$

The factor 2 in the equation (5.8) comes from the fact that the RF noise at both ω_{RF} and at $2\omega_{LO} - \omega_{RF}$ (the second is called an image band) will both be downconverted into $\omega_{LO} - \omega_{RF}$.

In this case, by definition of a noise factor from (2.1), we have:

$$F = \frac{SNR_{in}}{SNR_{out}} = \frac{S_{in}/N_{in}}{S_{out}/N_{out}} = \frac{S_{in}/N_{in}}{(S_{in} \times CG_P)/(2 \times N_{out} \times CG_P)} \tag{5.9}$$
$$= 2$$

As shown in (5.9), even the noiseless mixer can have a noise factor of 2 and a noise figure of 10log(2) = 3 dB. In this situation, the noise figure is defined when the signal is located on only one side of the LO signal. This type of definition is called a single-sideband noise figure (SSB NF) since the signal power is located on only one side of the LO signal. If an image-reject filter is used to suppress the input noise at $2\omega_{LO} - \omega_{RF}$, the noise in the image band can be suppressed and the noise figure could theoretically be as low as 0 dB. An example of this situation is when there is a sharp image-reject filter in front of the mixer.

For a double-sideband modulated waveform, there is signal energy in both sides of the LO signal, and the IF signal (at $\omega_{LO} - \omega_{RF}$) is twice as large, since signal energy from both sidebands (ω_{RF} and $2\omega_{LO} - \omega_{RF}$) falls onto the IF. In this case, we have:

$$S_{out} = 2 \times CG_P \times S_{in} \tag{5.10}$$

$$N_{out} = 2 \times CG_P \times N_{in} \tag{5.11}$$

$$F = \frac{SNR_{in}}{SNR_{out}} = \frac{S_{in}/N_{in}}{S_{out}/N_{out}} = \frac{S_{in}/N_{in}}{(2 \times S_{in} \times CG_P)/(2 \times N_{out} \times CG_P)} = 1 \qquad (5.12)$$

Since the mixer downconverts any energy at a distance of ω_{IF} from ω_{LO}, as well as energy from the harmonics of ω_{LO}, all the noise at ω_{IF} away from those harmonics will also be downconverted to the same frequency, resulting in lower output SNR and a higher noise figure. For example, if the LO signal is a 50% duty cycle square wave with unity amplitude and zero mean, v_{LO} in (5.1) becomes:

$$v_{LO}(t) = \frac{4}{\pi}\left(\sin(\omega_{LO}t) + \frac{1}{3}\sin(3\omega_{LO}t) + \frac{1}{5}\sin(5\omega_{LO}t) + ... + \frac{1}{n}\sin(n\omega_{LO}t) + ...\right) \qquad (5.13)$$

For simplicity, let us assume that the output and the input have the same reference impedance. If the input noise is white, i.e., has a constant power spectral density over all frequency bands, the total noise power downconverted to the same IF frequency will be:

$$N_{out} = 2 \times \left(\frac{2}{\pi}\right)^2 \left(1 + \left(\frac{1}{3}\right)^2 + \left(\frac{1}{5}\right)^2 + \left(\frac{1}{7}\right)^2 + ...\right) N_{in} = N_{in} \qquad (5.14)$$

However, from (5.6) and (5.13), the first-harmonic conversion gain of the mixer is only $2/\pi$. The output signal power in the case of a double-sideband signal becomes:

$$S_{out} = 2 \times \left(\frac{2}{\pi}\right)^2 S_{in} = \frac{8}{\pi^2} S_{in} \approx 0.81 S_{in} \tag{5.15}$$

From (5.14) and (5.15), it is clear that the output noise experiences higher effective gain than the desired signal. If the mixer itself does not add any additional noise into the system, the SNR reduction becomes 10log(1/0.81) = 0.91 dB.

So far, we have considered only the noise figure of the mixer due to "noise folding" of the incoming noise at RF. In practice, noise from the mixer circuitry must be considered as well, in order to evaluate the performance of a mixer. As shown in figure 5.3, circuit noise sources in the mixer can be separated into two groups. The first is the noise being added before mixing, and the other is the noise that is added directly at the output after mixing.

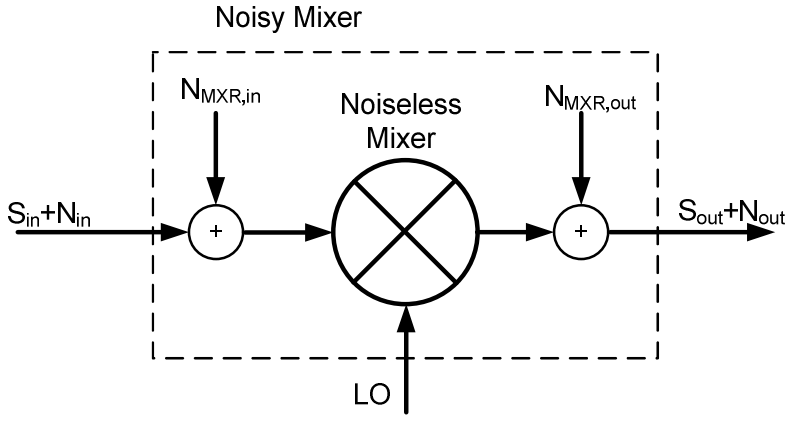

Figure 5.3 Circuit noise representatives in a mixer

The mixer noise at the input experiences the same mixing and noise folding mechanism as the incoming noise N_{in}, whereas the output noise does not. If the dominant

noise source is at the mixer input (before the multiplier), it is important to take into account the noise folding effects during design.

5.4 Basic CMOS Mixer Architectures

Having reviewed the mathematical representatives of a mixer, we now turn to implementation of an integrated mixer in CMOS technologies. In this section, we will review various CMOS downconversion mixer architectures that have been used in wireless communication systems. The reviews are intended to provide a general overview of different types of mixers, and not the detailed implementation of any particular mixers. Most integrated CMOS mixers, however, are constructed based on the architectures discussed in this section.

Mixing actions can be created by passing the RF and LO signals to a nonlinear gain stage and taking the intermodulation products of those two signals as the output. However, such a method usually exhibits high amounts of undesired spectral components, and the port-to-port (such as LO-RF) isolation is low. The lack of isolation causes many problems, such as radiation of the LO signal back to an antenna, leading to a time-varying DC offset problem [5.2].

In most cases, CMOS mixers based directly on multiplication (using a multiplier block instead of a nonlinear gain stage) exhibit superior performance because they generate strong desirable intermodulation products and have higher isolation among the ports (LO, RF, and IF ports). Furthermore, an excellent multiplier-based mixer can easily be implemented using good switches, which are readily available in submicron CMOS technology and can be scaled easily with technology nodes [5.2].

5.4.2 Single-balanced mixer

A common example of a commutating mixer is a single-balanced CMOS mixer, which is shown in figure 5.4. The mixer has a transconductor that converts an RF input voltage into current. The resulting current is then multiplied by the LO signal at the switching pair which consists of M_2 and M_3. If the voltage drive at the LO port is large enough, the RF current will be effectively multiplied by a perfect square wave with 50% duty cycle in which its frequency is that of the local oscillator.

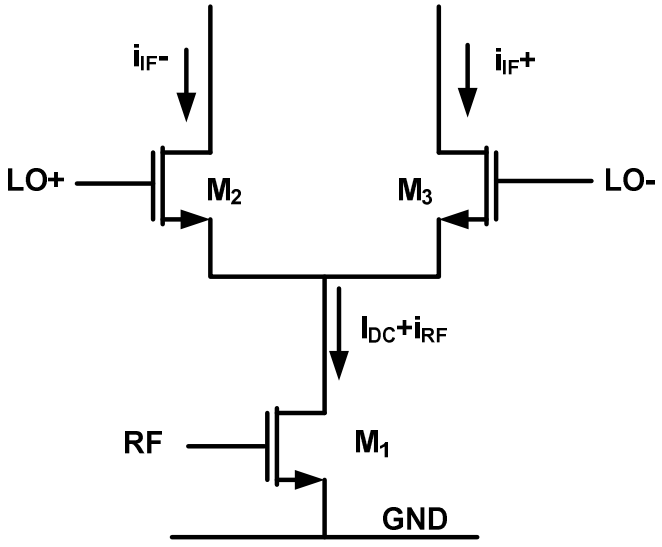

Figure 5.4 A single-balanced mixer

From equations (5.5) and (5.13), the first harmonic of the LO signal would produce the component at the output as follows:

$$i_{IF}(t) = \frac{2}{\pi} i_{RF}(t)\cos((\omega_{LO} - \omega_{RF})t) + \frac{2}{\pi} i_{RF}(t)\cos((\omega_{LO} + \omega_{RF})t) \qquad (5.15)$$

If we consider only one of the two components as the output, the conversion gain of the multiplier is then:

$$A_{I,CG} = \frac{2}{\pi} \tag{5.16}$$

If the transconductance and the load impedance are included in calculations, the voltage conversion gain of the mixer is then:

$$A_{V,CG} = g_m \frac{2}{\pi} Z_L \tag{5.17}$$

Even though the single-balanced mixer has high LO port to RF port isolations, and the conversion gain can be easily adjusted based on the g_m and Z_L as suggested by (5.17), it suffers from significant drawbacks. First, since the current from M_1 contains both DC and RF components, the IF signal contains the ω_{LO} term due to the mixing between the DC component from M_1 and the LO signal. Also, the LO signal can leak to the IF nodes due to a direct capacitive coupling through the drain of M_2 and M_3. Since the LO signal is usually large (in order to implement a fast-switching mechanism at the mixer), it can cause a large LO swing at the output of the mixer, which results in overall signal compression at the output nodes.

Another drawback of a single-balanced mixer is that the RF signal is unbalanced. The unbalanced signal path results in low IIP_2 performance and low common-mode noise immunity. Since IIP_2 is a major requirement in many receivers, especially in direct-conversion architectures, the use of a signal-balanced mixer is limited.

5.4.3 Double balanced active mixer

The most common way to overcome the LO-to-IF leakage and second-order intermediation problems in the single-balanced mixer is to use a double-balanced active

mixer architecture as shown in figure 5.5. This can be viewed as two single-balanced active mixers with separate inputs, and with the outputs tied together.

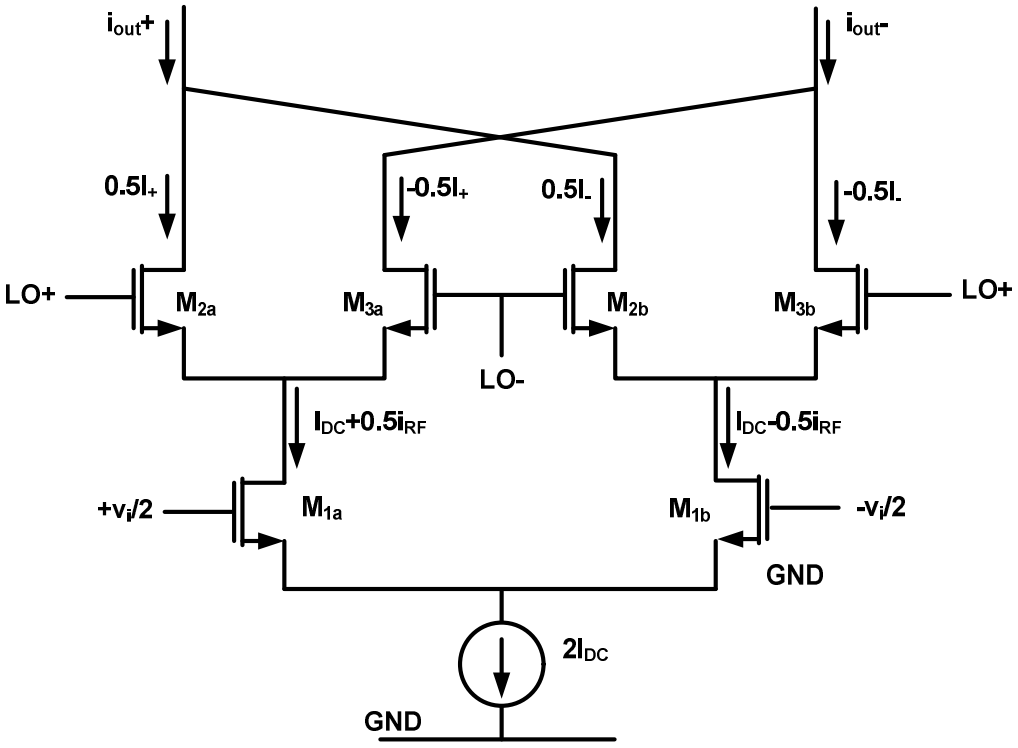

Figure 5.5 A double-balanced active mixer

If the RF drive into the circuit is balanced with the same amplitude and opposite phase (denoted as $+v_i/2$ and $-v_i/2$ in figure 5.5), the output current for the first-order linear term is then:

$$i_{out}(t) = i_{+}(t) - i_{-}(t) \tag{5.18a}$$

$$i_{out}(t) = g_m \frac{v_i}{2} \times g_{LO}(t) - \left(g_m \left(-\frac{v_i}{2} \right) \times g_{LO}(t) \right) \tag{5.18b}$$

$$i_{out}(t) = g_m \frac{v_i}{2} \times g_{LO}(t) + g_m \frac{v_i}{2} \times g_{LO}(t) = g_m v_i g_{LO}(t) \tag{5.18c}$$

Where g_{LO}(t) is the multiplication function that depends on the LO signal. From (5.18), it is clear that a double-balanced mixer provides the same transfer function as the single-balanced active mixer for the linear term of the transconductance. If we consider the second-order term of the transconductance, the overall transfer function becomes:

$$i_{out,2nd}(t) = i_{2nd,+}(t) - i_{2nd,-}(t) \tag{5.19a}$$

$$i_{out,2nd}(t) = g_{m,2nd}\left(\frac{v_i}{2}\right)^2 \times g_{LO}(t) - \left(g_{m,2nd}\left(-\frac{v_i}{2}\right)^2 \times g_{LO}(t)\right) \tag{5.19b}$$

$$i_{out,2nd}(t) = 0 \tag{5.19c}$$

Equations (5.19) suggest that in balanced driving conditions, the second-order nonlinear terms at the input devices are cancelled out. This means that a double-balanced active mixer has theoretically infinite IIP_2.

In practice, the amount of IM_2 cancellation is limited by the mismatches in the circuits. Nevertheless, improvements of IIP_2 compared to the single-balanced mixer usually exceed 40 dB (1% mismatch), and achievable mixer IIP_2 is as high as 80 dBm [5.3].

In general, we can extend the results in (5.19) to any terms in the voltage-to-current transfer function of M_{1a} and M_{1b}. Any even-order terms (including the DC term)

will be cancelled out in this mixer architecture. In contrast, any odd-order terms will experience the same transfer function as in the single-balanced mixer case.

Another advantage in this mixer architecture is that the direct capacitive coupling of the LO signal into the IF port is greatly reduced due to cancellation of multiple coupling in opposite directions. For instance, the LO+ signal couples through M_{2a} into the drain of M_{2a} while the LO- signal couples into the same node via M_{2b}. Due to symmetry, these two coupling signals are similar in size but have the opposite phase, thus significantly reducing the total effective coupling.

The double-balanced active mixer architecture has been used extensively in CMOS receiver designs [5.4][5.5]. However, this architecture has a major drawback when it is employed in a CMOS technology. Since CMOS devices exhibit high levels of 1/*f* noise at high bias currents and small device sizes, the active mixer (either single or double-balanced) generates high levels of output 1/*f* noise at low IF frequencies. The majority of the output noise comes from the 1/*f* noise contributions from the switching pair during the transition period [5.6]. To quantify the amount and mechanism of *1/f* noise in an active mixer, we can review a simple switching pair with noise sources, as shown in figure 5.6. Any noise generated by M_2 and M_3 is modeled as the input-referred voltage noise. During LO switching when V_{LO} is small, both M_2 and M_3 are active and the circuit operates as a differential pair with M_3 as the current source. The input-referred voltage noise of M_2 or M_3 will generate an output noise equal to:

$$\sqrt{\overline{v_{n,out}^2}} = \left| g_{m,M_{2,3}} \right| \sqrt{\overline{v_{n,M_{2,3}}^2}} \tag{5.20}$$

During the period when the mixer is fully switched, one of the two devices in the mixer quad operates as a cascode device on top of M_3, while another device is turned off and does not generate any noise. In this configuration, output noise due to *1/f* noise contributed by the cascode device can be estimated as:

$$\sqrt{\overline{v_{n,out}^2}} = \left| \frac{g_{m,M_{CAS}}}{1 + g_{m,M_{CAS}} Z_{d,M_1}} \right| \sqrt{\overline{v_{n,M_{CAS}}^2}} \tag{5.21}$$

where is Z_{d,M_1} is the impedance looking from the cascode device into the drain of M_1. If the magnitude of $g_{m,M_{CAS}} Z_{d,M_1}$ is much higher than unity (which is likely the case for CMOS devices in saturation), this *1/f* noise contribution can be considered negligible.

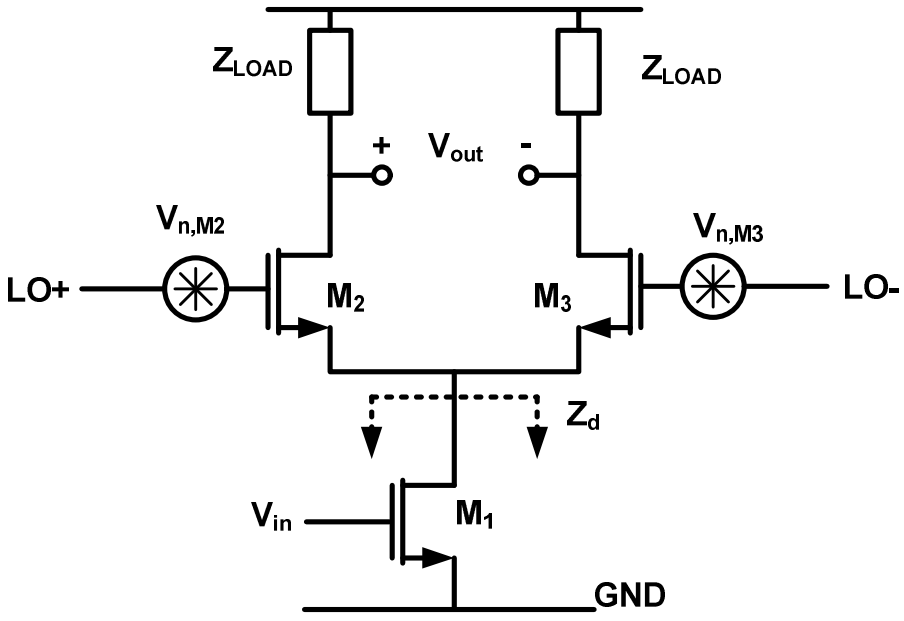

Figure 5.6 A simplified mixer schematic with switching devices noise models

From the above analysis, this means that the *1/f* noises from M_2 and M_3 are being modulated or "mixed" by the time-varying transfer function that depends on the operating states of the mixer switches. Since this is the same mixing process described in section 5.3, these *1/f* noise components will either directly feed through or be frequency translated into higher frequency and present at the output. In most cases, the IF frequency is much lower than the LO frequency and we are interested only in the direct feed-through component of the 1*/f* noise. The coefficient of this feed-through term is the average low-frequency gain from the gate of M_2 or M_3 to the output.

To simplify further analysis, we make the following assumptions:

(1) The mixer is fully switched to one side when $|V_{LO}| > V_{SW}$, and is operating as a differential pair when $|V_{LO}| < V_{SW}$.

(2) The switching mechanism is abrupt (i.e., the mixer moves promptly from "differential-pair" mode to "fully-switched" mode).

(3) The peak amplitude of V_{LO} is higher than V_{SW}, and the mixer is fully switched during each V_{LO} cycle.

(4) V_{LO} slope is constant during the transition period when $|V_{LO}| < V_{SW}$.

(5) During the transition period, output noise caused by M_2 or M_3 is described in (5.20). When the mixer is fully switched, M_2 and M_3 contribute no noise to the output.

Using these assumptions, the amount of time that M_2 and M_3 operates as a differential pair is:

$$T_{diff} = 2\frac{V_{SW}}{S_{LO}} \tag{5.21}$$

where S_{LO} is the slope of the LO during the transition period. If the total LO period is T_{LO}, the total time that LO spends as a percentage of the period is:

$$\frac{T_{diff}}{T_{LO}} = 2\frac{V_{SW}}{S_{LO}T_{LO}} \tag{5.22}$$

From (5.20) and (5.22), the average output noise due to M_2 or M_3 is:

$$\overline{v_{n,M_{2,3}}^2} = \left(2\frac{g_{m,M_{2,3}}V_{SW}}{S_{LO}T_{LO}}\right)^2 \overline{v_{n,M_{2,3}}^2} \tag{5.23}$$

From (5.23), for a given LO frequency, one can reduce the output noise by reducing V_{SW} while keeping g_m and the noise source voltage at the same level or smaller. This can be achieved by reducing overdrive voltage and increasing the width of M_1 and M_2 in such a way that g_m is kept constant. This methodology, however, results in higher loading seen at the LO port and higher power consumption. Also from (5.23), increasing S_{LO} reduces the output noise from M_2 or M_3. However, this tends to result in larger LO swing and higher power consumption as well. In addition, large LO swings can have negative impacts on the linearity of an active mixer due to injection of the LO signal into the signal path, especially at the common source node of M_{1a} and M_{1b}, causing spikes in current and forcing transistors to leave the saturation region [5.2].

5.4.4 Folded passive mixer with active driving stage

As mentioned in the previous section, CMOS active mixers suffer from *1/f* noise problems once the switching-time is finite. Since the amount of the *1/f* noise in a CMOS device is proportional to the DC current [5.7], the *1/f* noise in the mixer can be substantially reduced using a switching quad with very low or no DC current. This type of mixer is called a passive mixer, stressing the fact that the mixer core itself is "passive," i.e., has no DC current and does not provide gain. Most CMOS passive mixers, however, still require supporting circuits that consume currents, such as input drivers and LO buffers. Also, a passive mixer usually requires higher LO drives than active mixers in order to turn the MOS transistors into a deep-triode region [5.8][5.9]. Figure 5.7 shows an example of a passive mixer.

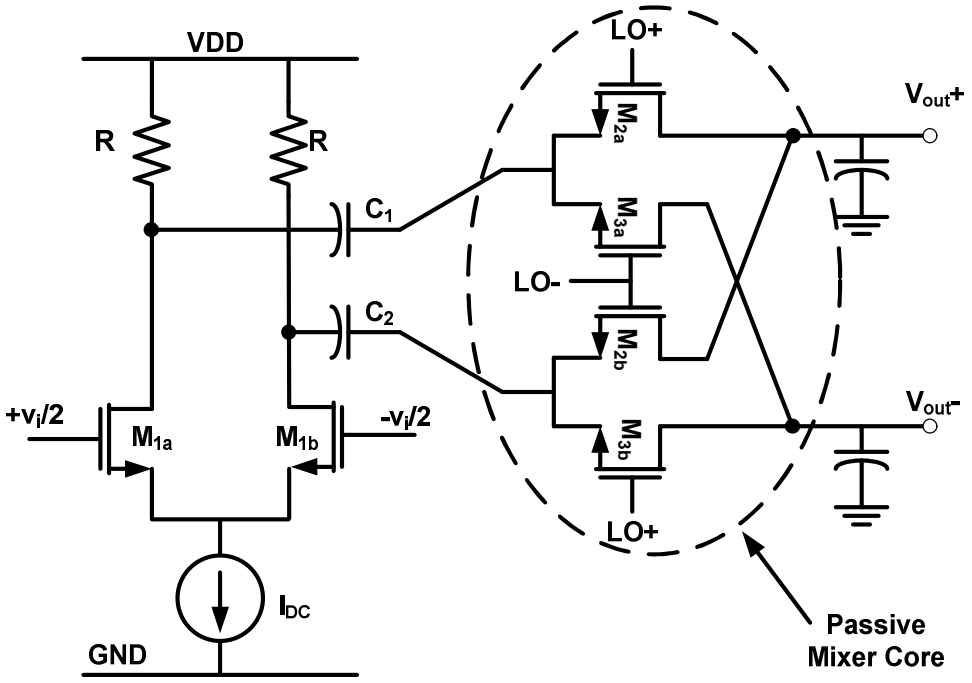

Figure 5.7 A voltage-mode passive mixer

The mixer in figure 5.7 has an active input stage with DC current consumption. Even though the overall circuit consumes a static current, this type of mixer is still considered passive, because the mixer core itself has no bias current due to the DC blocking capacitors C_1 and C_2. The output of this mixer is the voltage across the output capacitors.

5.4.4.1 Voltage Mode Passive Mixer

In general, passive mixers can be categorized as either current-mode mixers or voltage-mode mixers, determined by the amount of current flowing through the mixer core during the mixing process. In voltage-mode mixers, very low currents flow through the mixer core, and the output voltage is developed right at the switching quad output [5.8][5.10][5.11]. The mixer in figure 5.7, for example, is considered a voltage-mode mixer if the load capacitance is low. Since minimal current flows through the mixer, the on-resistance of the switches can be relatively high.

Extensive analysis of voltage-mode mixers with capacitive loading has been carried out by modeling the switches as time-varying conductors [5.12]. The results show that the conversion gain varies with how the switch conductance changes over time. If the change is an ideal square-wave function, the conversion gain will be -3.9dB. However, conversion gain will be -2.1dB if the drive is sinusoidal. Additionally, the conversion gain has low-pass characteristics at the IF (after mixing), and the 3dB pole is determined by the capacitance and the average total conductance from the input node to the output node.

To achieve high-linearity performance, it is prudent to minimize the non-linear voltage across the switches. This can be achieved by 1) reducing the average on-resistance with higher LO drives or using larger switches, both of which result in higher power consumption, or 2) minimizing the amount of current flowing through the switches by using a higher impedance load (higher resistance and/or smaller capacitance).

5.4.4.1 Current Mode Passive Mixer

In contrast to their voltage-mode counterparts, current-mode mixers commute current signals through the switching quad without large voltage swing at the input or output terminals [5.13][5.14][5.15]. An example of a current-mode mixer is shown in figure 5.8.

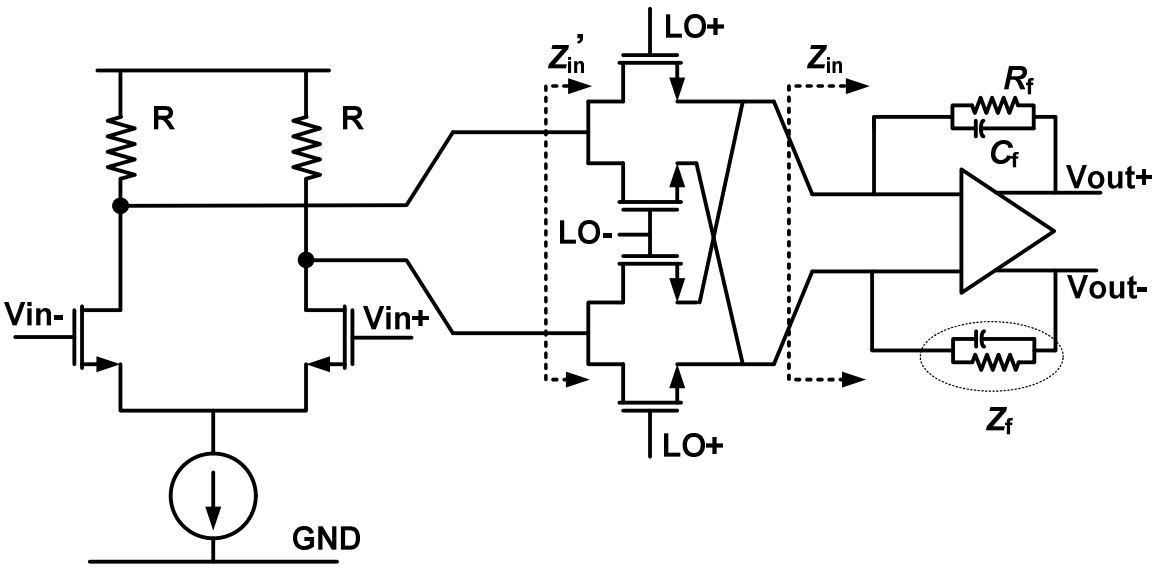

Figure 5.8 A current-mode mixer with a transimpedance amplifier load

In this mixer, the switching quad is driven by an amplifying stage, with a transconductance amplifier connected as an output load. If the impedance looking from the input stage into the mixer core is low compared to the output impedance of the driving stage ($|Z_{in}'| << R$), the input stage will act as a transconductor with output currents flowing into the mixer core. To ensure that $|Z_{in}'|$ is low, the switches must be relatively large and driven strongly by the LO so that their average on-resistance is small. In addition, the gain and bandwidth of the transconductance amplifier load must be sufficiently high to ensure that $|Z_{in}'|$ is low across the IF band of interest. Alternately, a common-gate stage, which has low broadband input impedance, can be chosen as the mixer load instead of a transconductance amplifier [5.15].

Current-mode passive mixers enjoy the benefits of having low *1/f* noise, as in voltage-mode passive mixers. In addition, because the circuit operates in the current domain except at the RF input and final IF output nodes, the voltage swing of internal nodes is minimized. This property is beneficial in a deep-submicron CMOS process with limited supply headroom. Further, designing good CMOS switches has become easier as devices have scaled down in size. As a result, this mixer architecture is an ideal candidate for implementing integrated receiver front-ends in future-generation communication systems. Chapter 6 will provide a discussion of the detailed analysis and design of a high-dynamic-range current-mode mixer with a transimpedance amplifier load, and Chapter 7 will present a wideband receiver front-end incorporating this type of mixer.

It is worth noting that there are reports of finite (and sometimes significant) *1/f* noise measured from a passive mixer [5.10][5.13], possibly due to *1/f* noise from the supporting blocks, such as baseband filters or amplifiers. In the case that the measuring

instruments or other circuits following the mixer (such as a filter) have high *1/f* noise, the de-embedding of the *1/f* noise in the mixer alone could be inaccurate. In practice, if there is an LNA in front of the mixers, the *1/f* noise in the mixer needs to be low enough to be negligible when referred back to the LNA input.

5.5 Quadrature Signal Generation

Many receiver and transmitter architectures require quadrature signals. The accuracy of the quadrature signals determines the image rejection [5.16]. In this section we will discuss the three main quadrature generation techniques used in integrated applications.

5.5.1 Frequency division

In-phase and quadrature periodic signals at ω_{LO} can be generated using a master-slave flip-flop to frequency-divide a signal at $2\omega_{LO}$ by a factor of 2, as shown in figure 5.9(a). In this scheme, each of the flip-flops is triggered by the rising or falling edges of the incoming clock in an opposed manner. For example, flip-flop A is triggered by the rising edges, while flip-flop B is triggered by the falling edges. If the incoming clock has a "high" period of T_D, the phase of V_{out}-Q will lag the phase of V_{out}-I by:

$$\Delta\phi = \phi_I - \phi_Q = (2\pi)\frac{T_D}{2T_{clock}} \tag{5.24}$$

where $2T_{clock}$ is the period of the output clocks (V_{out}-Q and V_{out}-I). If D is the duty cycle of the incoming clock, we then have:

$$D = \frac{T_D}{T_{clock}} \tag{5.25}$$

Applying (5.25) into (5.24), we have:

$$\Delta\phi = \pi D \tag{5.26}$$

If the input clock has a 50% duty cycle (D = 0.5), the output of the flip-flops will be 90° out of phase from each other, resulting in perfect quadrature signal generation.

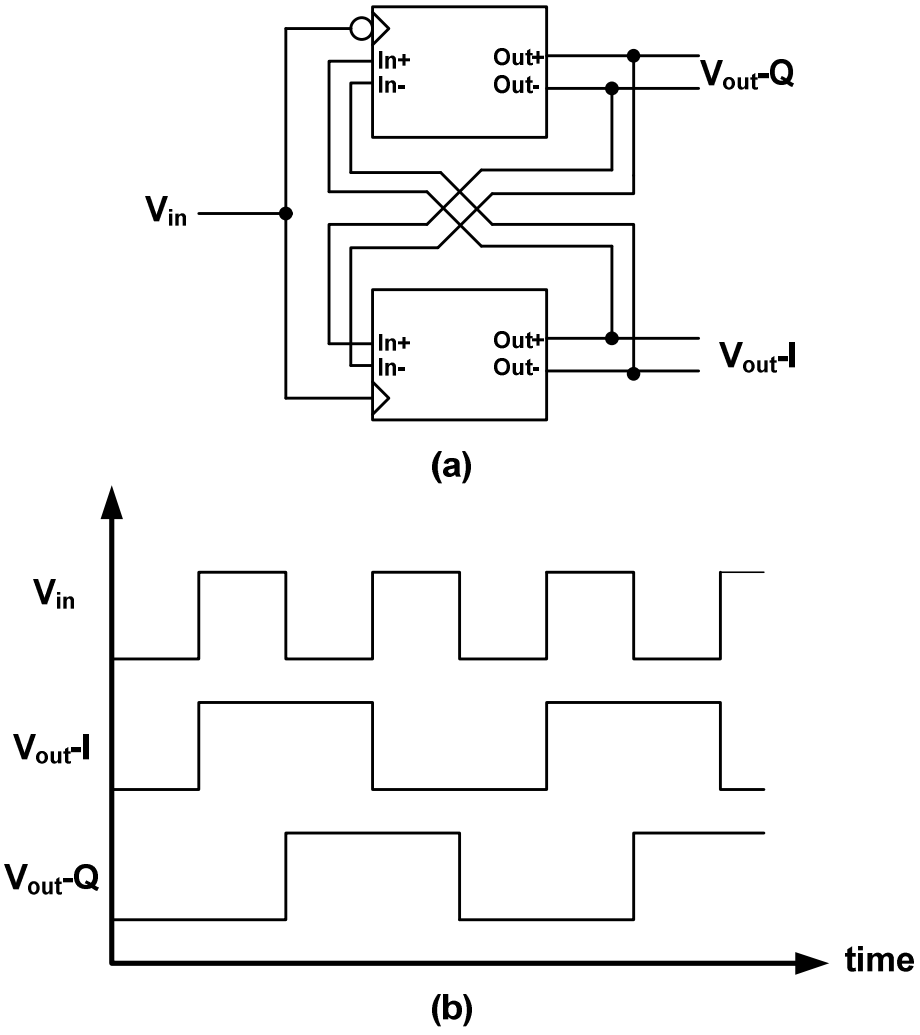

Figure 5.9 Quadrature generation by division by 2

Important drawbacks of this scheme are: a significant increase in power consumption due to the need for an incoming signal running at $2\omega_{LO}$, and the need for an accurate 50% duty cycle of the incoming clock from an oscillator.

The dependence on the duty cycle can be eliminated by running an oscillator at four times the desired frequency ($4\omega_{LO}$) and applying its output to a divide-by-four block implemented by cascading two divide-by-two circuits. Ignoring any non-idealities or mismatches, the output signal of the divide-by-two circuit shown in figure 5.9(b) will have a 50% duty cycle regardless of the duty cycle of the input signal. Using this fact, we can generate a 50% duty cycle signal at $2\omega_{LO}$ as an input clock for the final divider. This method, however, imposes more stringent demands on the digital divider, and requires the oscillator to operate at higher frequencies.

A comparator with an adjustable threshold in front of the divide-by-two can adjust the clock's duty cycle toward highly accurate quadrature outputs. The threshold is computed with a feedback loop that measures the quadrature error [5.17]. This scheme does not suffer from a factor-of-two penalty in speed as in the divide-by-four case, but is limited by the accuracy of the quadrature phase measurement. Additional limitations are imposed by power consumption, feedback stability, and settling time [5.16].

5.5.2 Quadrature coupled oscillator

Another method for generating a quadrature signal is to use a quadrature-coupled oscillator. In this method, two identical oscillators are coupled in such a way that their outputs are forced to oscillate 90° out of phase. Figure 5.10(a) shows the typical approach

to practically coupling two NMOS-only cross-coupled oscillators [5.18]. The block diagram of the circuit is depicted in figure 5.10(b).

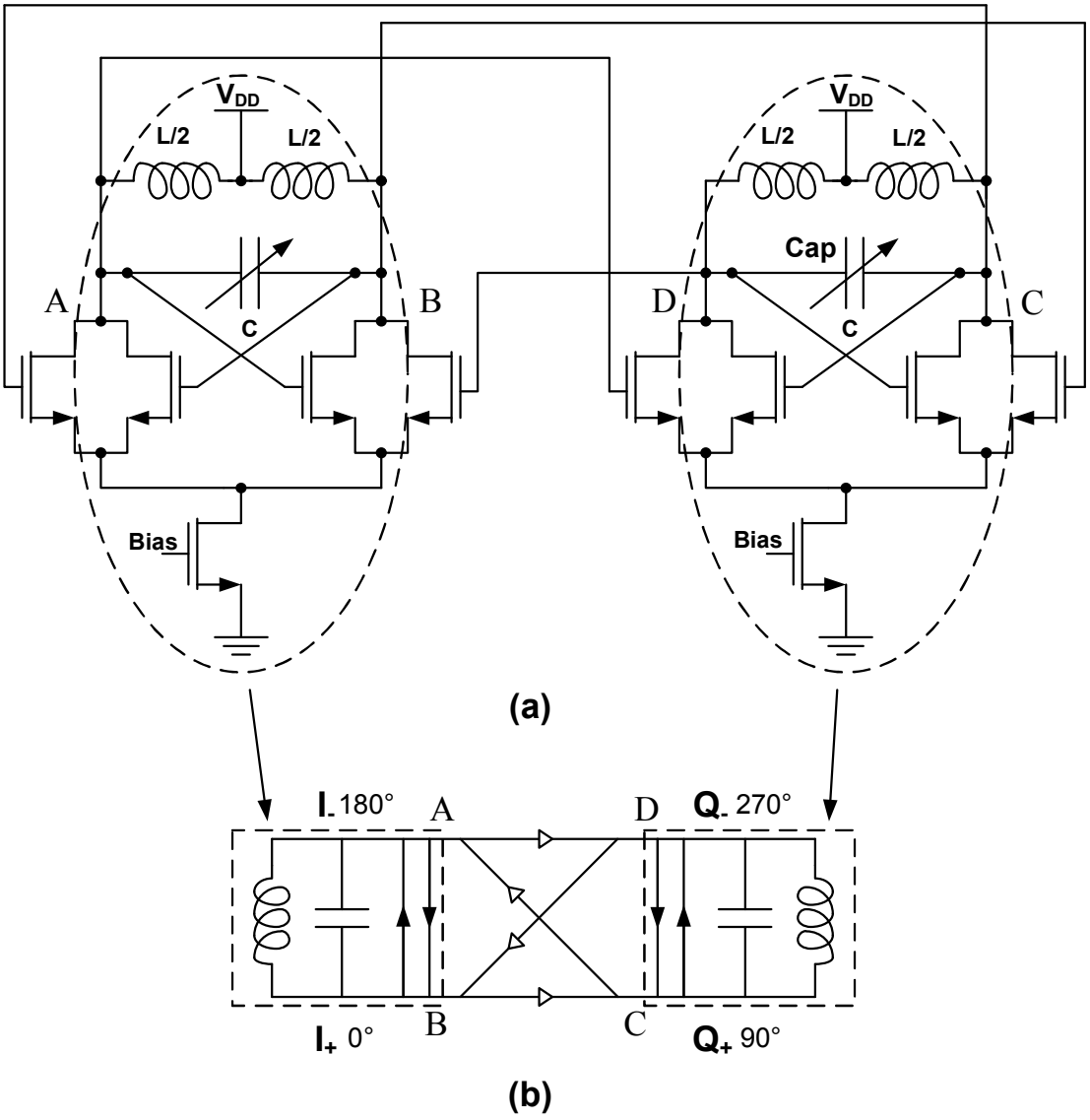

Figure 5.10 Quadrature Coupled LC VCO

As figure 5.10(b) shows, signals at the output nodes of interest, namely I_p, I_n, Q_p, and Q_n, each have the same frequency and amplitude but are phase-shifted in multiples of

90°, respectively. The solid triangle signifies the cross-coupled pair of the transistor, while the white triangle denotes coupling between the two oscillators. Under normal operating conditions at steady state, the two outputs across the cross-coupled pair on each of the oscillator are 180° out of phase. Due to symmetry of the circuit configuration, the coupling transistors (the triangle) provide a 90° phase shift between the input and output. One can see that the A→C path needs to provide the same phase shift as the C→D path due to symmetry. Since the signal at C is 180° out of phase from A, this means that both path A→C and path C→D need to provide the same phase shift, which is 90°. In other words, if one assumes that the oscillator on the left is 90°+Δ ahead of the one on the right, it can be argued that, looking at the mirror image of the oscillator, we will see that the left side is 90°-Δ ahead. Assuming both sides are identical, we should have 90°+Δ = 90°-Δ, and thus Δ =0. Interested readers can find a detailed analysis and design example of a quadrature oscillator in [5.16].

5.5.3 Polyphase filter quadrature signal generation

A quadrature signal can also be created using a polyphase filter to exploit phase shifts across RC networks. A polyphase filter is an RC-CR network with multiple outputs shifted in multiples of 90° from each other. The schematic of a polyphase filter is shown in figure 5.11.

From figure 5.11, the input signal has two terminals (at V_{in}+ and V_{in}-) with the same amplitude and opposite phase. The output will have the same amplitude with phase

shifted as show in the figure. In the ideal condition, the value of 2tan(ωRC) is equal to 90° at the frequency of interest.

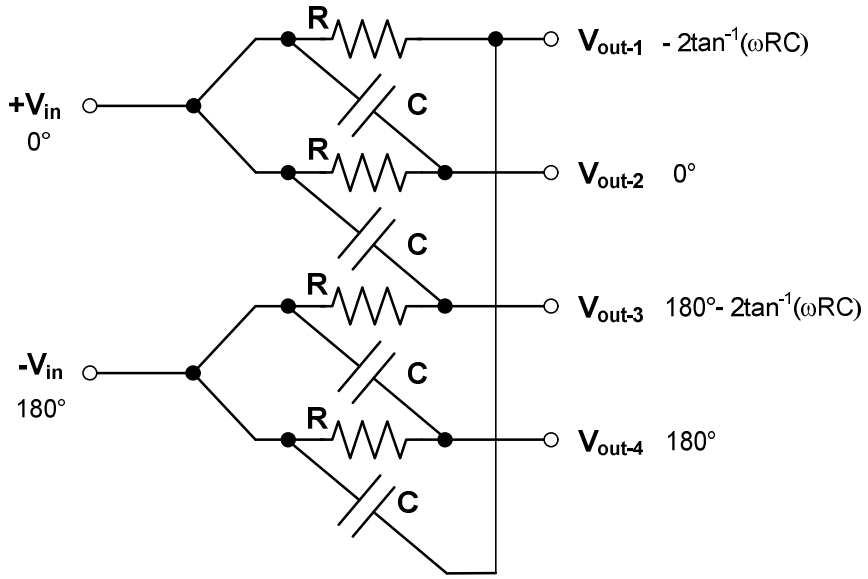

Figure 5.11 RC polyphase filter

Compared to other quadrature generation methods, the polyphase filter method is the simplest and requires no active devices by itself. However, this method is narrowband and works only at one frequency. For example, for the network shown in figure 5.11, ±1.7% variations in frequency translate to ±1° variations in phase shifts. Also, if the input signal contains higher harmonics of the LO signal, those harmonics will experience different phase shifts, causing dispersions leading to overall phase deviations from 90°. However, this problem is solved by employing a multi-stage polyphase filter at the cost of increased signal attenuation [5.19].

Another drawback of this method is that it relies on accurate matching and control of the RC product over process and temperature variations. Even though the process

variations can be minimized using production trimming or temperature compensation, its accuracy over operating ranges is limited.

5.6 CMOS Mixer Architectures for Multi-Band Receivers

This section offers a brief review of recently published CMOS mixers for wireless applications. The goal of this review is to compare the advantages and disadvantages of the topologies and deduce the optimal architecture for multi-band applications.

Figure 5.12 shows a CMOS active mixer with +78 dBm IIP_2, +9 dBm IIP_3, 4 nV/rt-Hz input referred noise, and 16 dB gain for Universal Mobile Telecommunication Systems (UMTS) applications [5.3]. Although the mixer achieves excellent noise and linearity performance, it requires a center-tap differential inductor to tune out parasitic capacitance at the source terminals of the switching devices (this is the 5.5 nH inductor in figure 5.12). Utilizing this architecture in multi-band front-ends would require large inductor areas and frequency-tuning circuitry, both of which have penalties in cost and complexity.

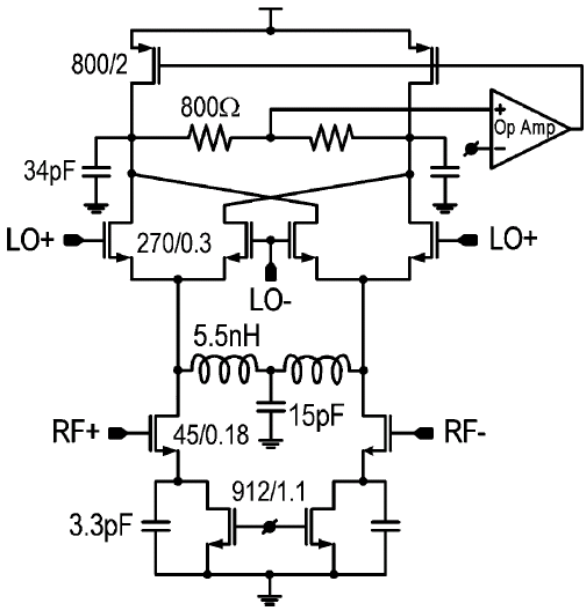

Figure 5.12 A high-linearity CMOS active mixer

(figure from [5.13])

A CMOS voltage-mode passive mixer with common-gate input stage is presented in [5.8], and its architecture is shown in figure 5.13. This mixer is similar to the one in figure 5.7, but the input transconductor is replaced by a differential common-gate amplifier stage. The chip achieves decent performance, with +54 dBm IIP_2, +8 dBm IIP_3, 9 dB DSB NF, and 11 dB voltage gain from 800 MHz to 2.1 GHz. However, it requires off-chip inductors at the input to act as high-frequency current sources for the common-gate stage. When implementing a complete front-end, this requirement results in additional pins required at the mixer input (in addition to the input pins at the LNA input), which can put constraints on package selection or total die area. In addition, this off-chip bias ground path could create bias current mismatches between the input devices and the bias replica, due to parasitic resistances.

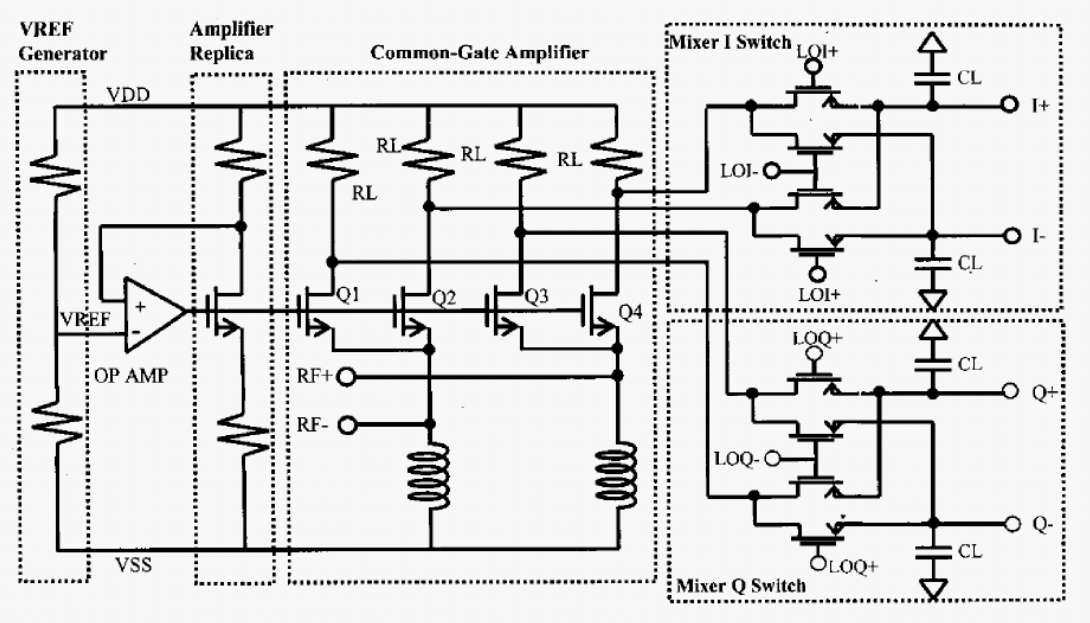

Figure 5.13 A CMOS passive mixer with common-gate input stage

(figure from [5.8])

Another voltage-mode passive mixer is reported in [5.11] and is shown in figure 5.14. The architecture utilizes a complementary input stage, using both PMOS and NMOS as the input transconductance devices in order to increase current efficiency. The chip achieves 15.7dB voltage gain, +1dBm IIP_3, and 12.9dB SSB NF at 2.4 GHz. No inductor or tuned circuit is implemented on the chip, resulting in an inherently broadband architecture suitable for multi-band operations. However, since this mixer has voltage-mode operations, its linearity is limited by the supply headroom as well as the total gain requirement of the circuit. With device scaling trending toward lower supply voltages, it would be challenging to achieve a high dynamic range front-end using this architecture in advanced CMOS technologies.

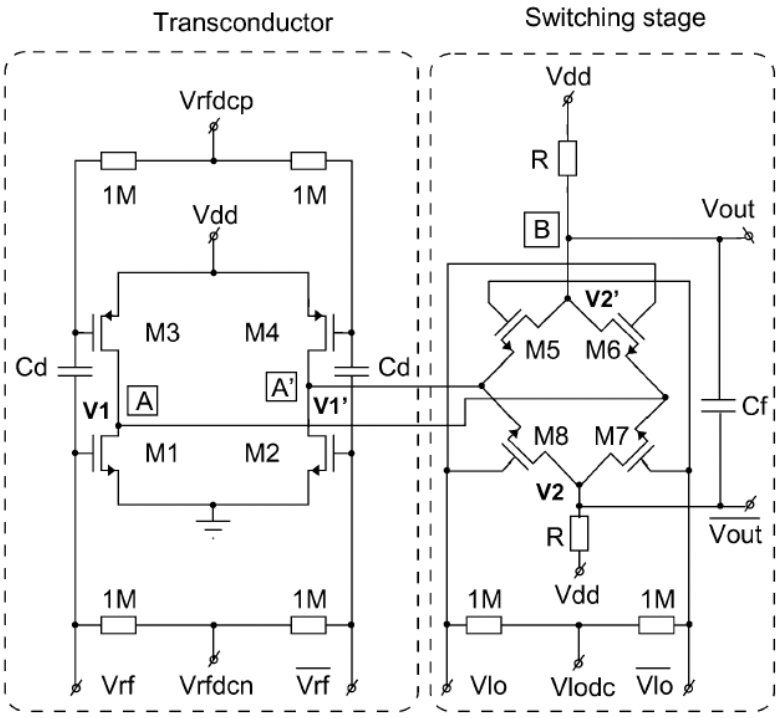

Figure 5.14 A voltage-mode CMOS passive mixer with complementary input (figure from [5.11])

To resolve the low-voltage problems, a current-mode passive mixer is proposed in [5.13]. The architecture is shown in figure 5.15 and is similar to that shown in figure 5.8, with a few differences. First, the input transconductance stage of the mixer in [5.13] is implemented as an LNA stage with input matching. Second, the I-path mixer and the Q-path mixer share the same input nodes, which are the LNA outputs. The front-end achieves 3.5 dB DSB NF, 24 dBm IIP_2, 24 dBm IIP_3, and 26 dB conversion gain. Although the mixer core itself is broadband, the LNA uses a narrow-band inductively degenerated architecture, resulting in an area and complexity penalty for multi-band designs. In addition, the input sharing of I and Q paths results in an overlapping on-

period of the connected switches, causing partial current division and gain reduction of the stage.

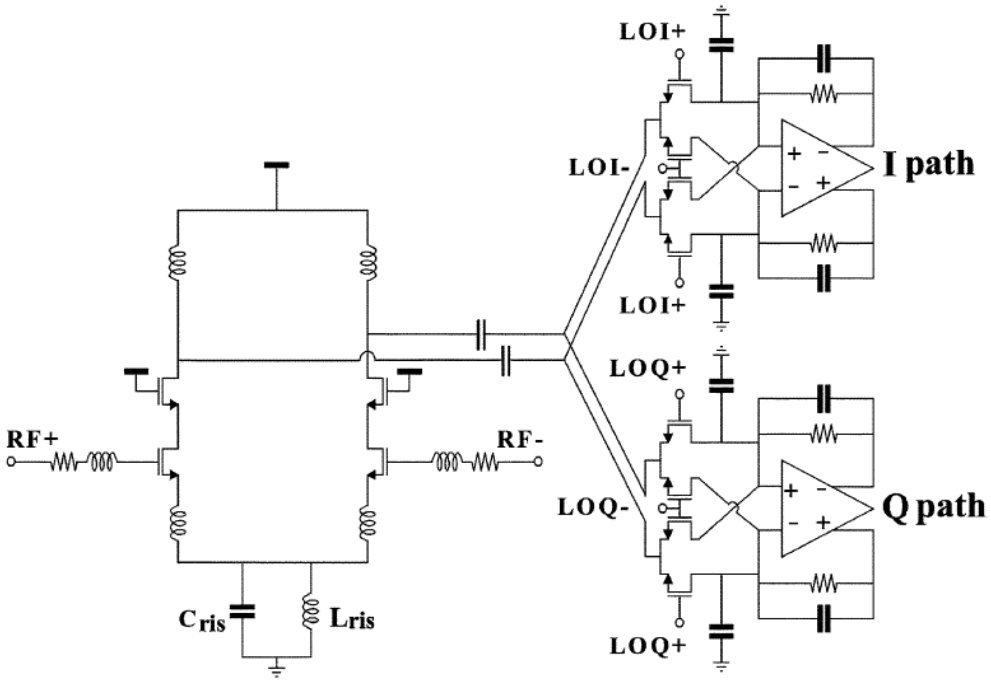

Figure 5.15 A receiver front-end with an LNA and current-mode passive mixers (figure from [5.13])

All of the mixers reviewed in this section exhibit advantages and disadvantages. In multi-band multi-standard applications, the mixer must be able to operate with several RF frequencies. This can be achieved by employing band-switching techniques or using wideband mixers. The band-switching methods have the benefit of increased signal selectivity, and are likely to require lower power consumption than the wideband method. However, implementing a band-switching mechanism usually requires inductors and capacitor banks, both of which result in higher die area and cost. In contrast, implementing a wideband mixer requires no band-switching circuit, and likely requires

no inductor if the speed of the transistors is sufficient. Aside from the cost benefits, an inductorless design reduces any coupling between the mixer and the substrate, resulting in lower magnetic noise and LO coupling in the mixer.

Besides being compatible with multiple RF frequencies, a multi-band multi-standard receiver front-end must have adjustable IF bandwidth, depending on the application. As discussed in chapter 2, the tunable IF bandwidth is best implemented using a direct-conversion architecture with frequency-tunable low-pass filters. In CMOS technologies, the frequency tuning circuitry can easily be implemented using CMOS switches.

Because a direct conversion architecture is preferable, it is important to minimize the low-frequency *1/f* noise at the mixer output. This makes the use of a passive mixer highly favorable. In addition, due to the scaling trend toward using lower supply voltage, current-mode mixer architectures offer better odds of achieving high linearity and dynamic range performance than their voltage-mode counterparts.

All of these considerations point to a passive current-mode passive mixer as an optimal architecture. In chapter 6, we will discuss the analysis, design, and implementation of a wideband quadrature demodulator that includes current-mode mixers and quadrature generation circuitry. Chapter 7 will present a wideband receiver front-end that consists of a quadrature mixer and a wideband inductorless LNA.

5.7 References

[5.1] B. Razavi. *RF microelectronics*. Prentice-Hall, Upper Saddle River, New Jersey, 1997.

[5.2] T. Lee. *The Design of CMOS Radio-Frequency Integrated Circuits*. Cambridge University Press, Cambridge, UK, 1998.

[5.3] M. Brandolini, P. Rossi, D. Sanzogni, and F. Svelto, "A +78 dBm IIP3 CMOS Direct Conversion Mixer for Fully Integrated UMTS Receivers," *IEEE J. Solid-State Circuits*, vol. 41, no. 3, pp. 552-559, Mar. 2006.

[5.4] S. Byun, C.H. Park, Y. Song, S. Wang, C. Conroy, and B. Kim, "A Low-Power CMOS Bluetooth RF Transceiver With a Digital Offset Canceling DLL-Based GFSK Demodulator," *IEEE J. Solid-State Circuits*, vol. 38, no. 10, pp. 1609-1618, Oct. 2003.

[5.5] J. Rogin, I. Kouchev, G. Brenna, D. Tschopp, and Q. Huang, "1.5-V 45-mW Direct-Conversion WCDMA Receiver IC in 0.13-µm CMOS," *IEEE J. Solid-State Circuits*, vol. 38, no. 12, pp. 2239-2248, Dec. 2003.

[5.6] H. Darabi and A. A. Abidi, "Noise in RF-CMOS Mixers: A Simple Physical Model," *IEEE J. Solid-State Circuits*, vol. 35, no. 1, pp. 15-25, Jan. 2000.

[5.7] P. Gray, P. Hurst, S. Lewis, and R. Meyer. *Analysis and Design of Analog Integrated Circuits*, 4th ed. New York: Wiley, 2001.

[5.8] S. Peng, C. Chen, and A. Bellaouar, "A Wideband Mixer for WCDMA/CDMA2000 in 90nm CMOS digital CMOS Process," in Proc. *IEEE Radio Frequency Integrated Circuits (RFIC) Symp.*, Jun. 2005, pp. 179-182.

[5.9] S. Zhou and M. F. Chang, "A CMOS Passive Mixer with Low Flicker Noise for Low-Power Direct-Conversion Receiver," *IEEE J. Solid-State Circuits*, vol. 40, no. 5, pp. 1084-1093, May 2005.

[5.10] H. Jen, S. Rose and R. Meyer, "A 2.2GHz Sub-Harmonic Mixer for Direct Conversion Receivers in 0.13μm CMOS," *IEEE Int. Solid-State Circuits Conf. Dig. Tech. Papers*, San Francisco, CA, Feb. 2006, pp. 460-461.

[5.11] V. Vidojkovic, J. Tang, A. Leeuwenburgh, and A. H. M. Roermund, "A Low Voltage Folded-Switching Mixer in 0.18-μm CMOS," *IEEE J. Solid-State Circuits*, vol. 40, no. 6, pp. 1259-1264, June 2005.

[5.12] A. Shahari, D. Sharffer, and T. Lee, "A 12-mW wide dynamic range CMOS front-end for a portable GPS receiver," *IEEE J. Solid-State Circuits*, vol. 32, no. 12, pp. 2061-2070, Dec. 1997.

[5.13] M. Valla, G. Montagna, R. Castello, R. Tonietto, and I. Bietti, "A 72-mW CMOS 802.11a Direct-Conversion Front-End with 3.5-dB NF and 200-kHz 1/*f* Noise Corner," *IEEE J. Solid-State Circuits*, vol. 40, no. 4, pp. 970-977, Apr. 2005.

[5.14] N. Poobuapheun, W-H. Chen, Z. Boos, and A. M. Niknejad, "A 1.5 V 0.7-2.5GHz CMOS Quadrature Demodulator for Multi-Band Direct-Conversion Receivers," *IEEE J. Solid-State Circuits*, vol. 42, pp. 1669-1677, Aug. 2007.

[5.15] Bagheri, A. Mirzaei, S. Chehrazi, M. Heidari, M. Lee, M. Mikhemar, W. Tang, and A. A. Abidi, "An 800-MHz–6-GHz software-defined wireless receiver in 90-nm CMOS," *IEEE J. Solid-State Circuits*, vol. 41, pp. 2860, Dec. 2006.

[5.16] R.A. Joo, "Frequency Generation Techniques for Integrated Applications," Ph.D. Dissertation, California Institute of Technology, 2004.

[5.17] S. Navid, F. Behbahani, A. Fotowat, A. Hajimiri, R. Gaethke, and M. Delurio, "Level-locked loop: a technique for broadband quadrature signal generation," *Custom Integrated Circuits Conference*, pp. 411-414, 1997.

[5.18] A. Rofougaran, J. Rael, M. Rofougaran, and A. Abidi, "A 900MHz CMOS LC-oscillator with quadrature outputs," in *IEEE Int. Solid-State Circuits Conf. Dig. Tech. Papers*, San Francisco, CA, Feb. 1996, pp. 392-393.

[5.19] C. De Ranter, M. Borremans, and M. Steyaert, "A Wideband Linearisation Technique for Non-Linear Oscillators Using a Multi-Stage Polyphase Filter," *IEEE ESSCIRC 1999*, pp 214-217.

6

Wideband CMOS Demodulator Analysis and Design

6.1 Introduction

As discussed previously, there is an urgent need to design a single transceiver that is compatible with multiple standards and multiple frequency bands of operation. Direct conversion (zero-IF) is attractive for the transceiver due to its high level of integration and the simplicity of the baseband circuitry. Despite the attractiveness, however, designing a mixer for multi-band operations in deep-submicron CMOS technology is nontrivial. The main challenge lies in maintaining moderate gain, noise figure, and linearity at minimum current consumption across a wide frequency spectrum with the abating supply voltage.

In this chapter, we will present the design of a wideband CMOS quadrature demodulator based on the passive current switching mixer with active first-order RC filtering at its output [6.1][6.2][6.3]. Complementary folded inputs [6.4][6.5] are employed to achieve higher transconductance efficiency. In order to realize a wideband demodulator, no inductor has been utilized. The elimination of inductors also leads to substantial die area reduction, and reduced substrate coupling due to the inevitably large inductor dimensions, especially at low GHz frequencies. The circuit operates over a wide

range of frequencies from 700 MHz to 2.5 GHz that cover important cellular and wireless LAN frequency bands.

This chapter is organized as follows. Section 6.2 reviews the architecture of the demodulator and the mixer. Section 6.3 presents the circuit design details of the mixer and the frequency divider, section 6.4 gives the measurement results, and the conclusion follows.

6.2 Quadrature Mixer Architecture

6.2.1 Demodulator High-Level Architecture

Figure 6.1 shows the demodulator block diagram, which includes two separate mixers for in-phase (I) and quadrature-phase (Q) paths, and a local oscillator (LO) generation circuit. The divide-by-two circuit is implemented to generate on-chip quadrature LO signals from the external $2f_{LO}$ source. The on-chip frequency division effectively isolates the signal coupling between LO and RF ports via bondwires, and reduces the reciprocal mixing considerably. This is important in direct-conversion systems where the desired signal is located at f_{LO}. Nonetheless, residual signal coupling occurs between LO and RF ports due to internal ground and supply bounce on the chip. All RF and signal paths are implemented in fully differential style in order to enhance common-mode noise rejection. Since the demodulator is designed to be integrated with an on-chip LNA, its input impedance is not matched to 50 Ω, and an off-chip resistor is used for input matching in measurements. Gain and phase matching between I and Q paths in this architecture depends strongly on the duty cycle of the external $2f_{LO}$, source, as will be discussed later in this chapter.

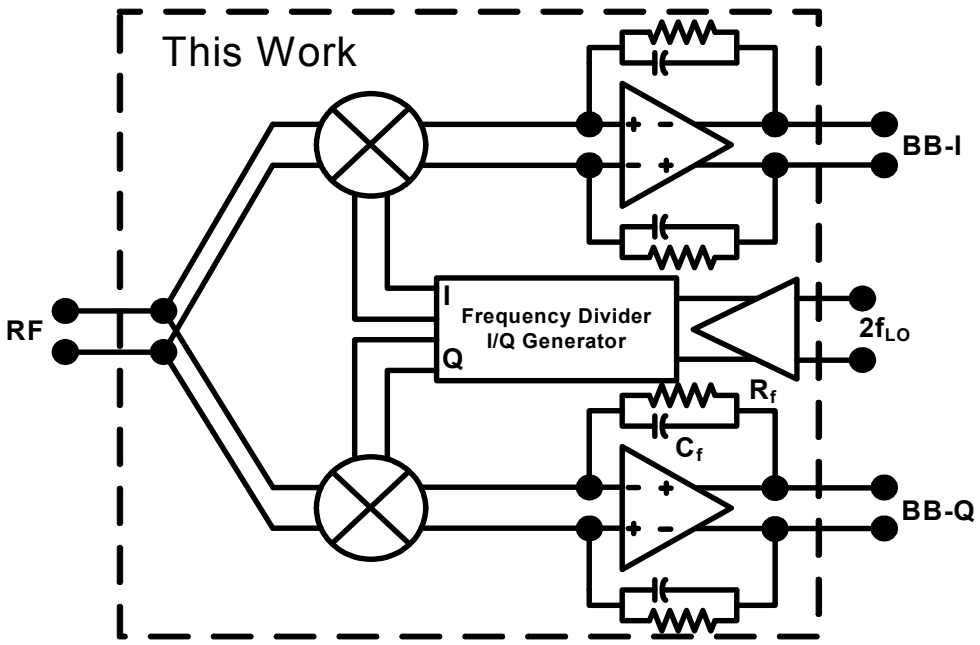

Figure 6.1 Demodulator architecture overview.

6.2.2 Mixer Circuit Architecture

Figure 6.2 shows a conceptual diagram of the mixer core, consisting of an RF transconductance stage followed by a double-balanced switching quad. An RF current from the transconductor commutates through the time-varying switching quad, experiences frequency translation, and flows into the transimpedance load. The baseband voltages are established at the amplifier output after the switching current passes through the first-order RC low-pass network. The overall voltage conversion gain of the mixer due to fundamental tone mixing can thus be approximated as:

$$\frac{V_{out}(f_{out})}{V_{in}(f_{in})} \approx \frac{2}{\pi} g_{\mathrm{m}} \left(\frac{R_{\mathrm{f}}}{1 + j2\pi f_{out} R_{\mathrm{f}} C_{\mathrm{f}}} \right) \tag{6.1}$$

where f_{out} is the output frequency at IF, f_{in} is the input RF frequency, g_{m} is the total transconductance of the input stage, and the factor $2/\pi$ is related to the first harmonic amplitude of the periodically time varying transfer function [6.6].

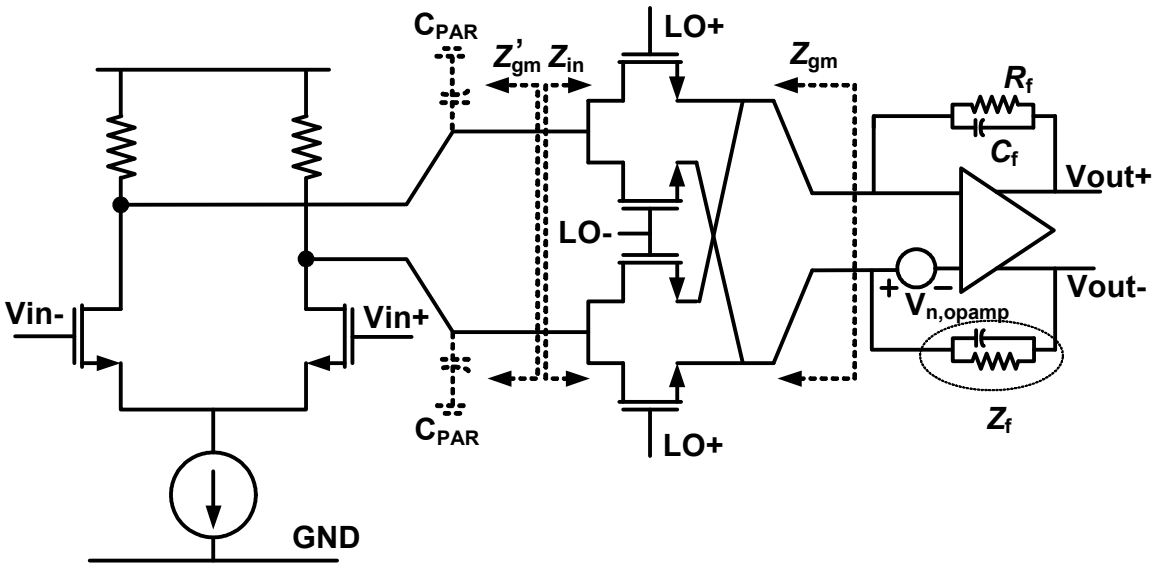

Figure 6.2 Mixer conceptual diagram

The operational amplifier provides a virtual ground at its input and appears as a low impedance (Z_{in}) at the mixer core output. Low Z_{in} retains the current mode operation at the output of the transconductor and hence relieves the linearity degradation imposed by the limited voltage headroom [6.2][6.3]. Another advantage of this architecture is that the signal experiences first-order low-pass filtering before reaching the first high voltage-swing node at the amplifier output. This results in a higher 1-dB compression point for

the mixer, as well as lowered linearity requirements on subsequent blocks in the receiver chain.

Major noise sources in this architecture are: the input transistors, the transimpedance amplifier, the feedback resistors, and the transistors in the switching quad. The 1/*f* noise in the switching quad depends on the amount of current flowing through the switches [6.7]. Since there is a very small DC bias current flowing through the switches, 1/*f* noise from the switching quad can be made negligibly small. Noise at the output of the mixer from each of the major noise sources is:

$$\overline{V}_{n,out}^2\left(f_{out},f_{in}\right)_{g_m}=\left(4kT\gamma g_{ds0}\right)\beta^2\left|Z_{\mathrm{f}}\left(f_{out}\right)\right|^2\Delta f \tag{6.2}$$

$$\overline{V}_{n,out}^2\left(f_{out},f_{in}\right)_{switches}=\frac{4kT}{R_{ON}}\left|\frac{R_{ON}}{R_{ON}+Z_{gm}^{'}\left(f_{in}\right)}\right|^2\beta^2\left|Z_{\mathrm{f}}\left(f_{out}\right)\right|^2\Delta f \tag{6.3}$$

$$\overline{V}_{n,out}^2\left(f_{out},f_{in}\right)_{opamp}=\overline{V}_{n,amp}^2\left|1+\frac{2Z_{\mathrm{f}}\left(f_{out}\right)}{Z_{\mathrm{gm}}\left(f_{in}\right)}\right|^2 \tag{6.4}$$

$$\overline{V}_{n,out}^2\left(f_{out},f_{in}\right)_{R_f}=\frac{4kTR_{\mathrm{f}}\Delta f}{\left|1+j2\pi f_{out}R_{\mathrm{f}}C_{\mathrm{f}}\right|^2} \tag{6.5}$$

where γ is process-dependent [6.6], β^2 is a constant representing switching activities, including noise folding effects, and equals $\pi^2/8$ under the assumption of perfect-square wave switching [6.6]. $\overline{V}_{n,amp}^2$ is the operational amplifier's input-referred voltage noise, R_{ON} is the average on-resistance of the switches, and Z_{gm} is the effective impedance looking into the switches from the transimpedance amplifier, as shown in figure 6.2. If the current is small and the transistor is biased to have low average on-resistance, the

noise contribution from the switches to overall noise performance is negligible. If we exclude the noise from the source and the switching quad, the total added output spot noise in the mixer can be estimated as:

$$\overline{V}_{n,out}^2\left(f_{out},f_{in}\right)=\left(4kT\gamma g_{ds0}\right)\beta^2\left|Z_{\mathrm{f}}\left(f_{out}\right)\right|^2\Delta f+\overline{V}_{n,amp}^2\left|1+\frac{2Z_{\mathrm{f}}\left(f_{out}\right)}{Z_{\mathrm{gm}}\left(f_{in}\right)}\right|^2+\frac{4kTR_{\mathrm{f}}\Delta f}{\left|1+j2\pi f_{out}R_{\mathrm{f}}C_{\mathrm{f}}\right|^2} \tag{6.6}$$

Dividing the output noise by the voltage gain of the mixer, the input referred voltage noise is:

$$\overline{V}_{n,in}^2\left(f_{out},f_{in}\right)=\frac{\left(4kT\gamma g_{ds0}\right)\beta^2\left|Z_{\mathrm{f}}\left(f_{out}\right)\right|^2\Delta f}{g_m^2\left(\frac{2}{\pi}\right)^2\left|Z_{\mathrm{f}}\left(f_{out}\right)\right|^2}+\frac{\overline{V}_{n,amp}^2\left|1+\frac{2Z_{\mathrm{f}}\left(f_{out}\right)}{Z_{\mathrm{gm}}\left(f_{in}\right)}\right|^2}{g_m^2\left(\frac{2}{\pi}\right)^2\left|Z_{\mathrm{f}}\left(f_{out}\right)\right|^2}+\frac{4kTR_{\mathrm{f}}\Delta f}{g_m^2\left(\frac{2}{\pi}\right)^2\left|Z_{\mathrm{f}}\left(f_{out}\right)\right|^2\left|1+j2\pi f_{out}R_{\mathrm{f}}C_{\mathrm{f}}\right|^2} \tag{6.7}$$

If $Z_{\mathrm{f}} >> Z_{\mathrm{gm}}$, and defining $\alpha = g_m/g_{ds0}$, the equation above simplifies to:

$$\overline{V}_{n,in}^2\left(f_{out},f_{in}\right)=\frac{4kT\gamma}{\alpha g_m}\left(\frac{\beta\pi}{2}\right)^2\Delta f+\frac{\pi^2}{g_m^2}\left(\frac{\overline{V}_{n,amp}^2}{\left|Z_{\mathrm{gm}}\left(f_{in}\right)\right|^2}+\frac{kT}{R_{\mathrm{f}}}\Delta f\right) \tag{6.8}$$

An interesting observation from (6.8) is that the input-referred noise increases when Z_{gm} decreases [6.3]. If Z_{gm} is dominated by the parasitic capacitance C_{par} as show in the figure 6.2, then:

$$Z_{gm}\left(f_{in}\right)=\frac{1}{4f_{LO}C_{par}} \tag{6.9}$$

where f_{LO} is the LO frequency, which is close to f_{in} for direct conversion receivers. Applying (6.9) to (6.8), we get:

$$\overline{V}_{n,in}^2(f_{out}, f_{in}) = \frac{4kT\gamma}{\alpha g_m}\left(\frac{\beta\pi}{2}\right)^2 \Delta f + \left(\frac{4\pi f_{LO} C_{par}}{g_m}\right)^2 \overline{V}_{n,amp}^2 + \frac{\pi^2}{g_m^2}\left(\frac{kT}{R_f}\right)\Delta f \tag{6.10}$$

As suggested by the equation above, noise contributions from the transimpedance amplifier become significant at higher input frequency, and increase with C_{par}. In a narrowband design we can employ an inductor to tune out C_{par}, whereas in this broadband design it is important to reduce this capacitor as much as possible.

Linearity performance in the mixer depends on: 1) the linearity of the voltage-to-current conversion in the transconductance stage, 2) effects from the switching stage, as well as 3) the linearity of the transimpedance amplifier stage. The linearity of a transconductance stage has been extensively analyzed in [6.8][6.9], and can be designed to have higher than +10 dBm IIP_3 with careful sizing and moderate current consumption. In wideband designs, the linearity of this stage will be relatively flat as a function of operating and offset frequencies. The linearity of the transimpedance amplifier, however, depends strongly on the frequency offsets of the blocking signal from the carrier, as can be explained as follows. As depicted in figure 6.2, the transimpedance amplifier can be viewed as a current-feedback amplifier with feedback impedance Z_f and driven by a current source with effective impedance Z_{gm}. Assuming an amplifier has a forward voltage transfer function of $A(f)$, the total loop gain of this amplifier can be written as:

$$T(f) = A(f)\frac{Z_{gm}(f)}{Z_{gm}(f) + Z_f(f)} \tag{6.11}$$

$$T(f) = A(f)\frac{Z_{gm}(f)}{Z_{gm}(f) + \left[\frac{R_f}{1 + j2\pi f R_f C_f}\right]} \tag{6.12}$$

To get higher loopgain and a higher input-refereed input intercept point, we need to maximize the open-loop linearity of $A(f)$ as well as the loopgain $T(f)$ [6.10]. Due to frequency conversion in the switches, impedance $Z_{gm}(f)$ at low frequency (near DC) will be proportional to the impedance $Z'_{gm}(f)$ near the LO frequency. Since $Z'_{gm}(f)$ is relatively flat near the LO frequency, $Z_{gm}(f)$ is approximately constant as a function of baseband frequency. $Z_f(f)$, however, follows 20 dB/dec decrease with baseband frequency since it is an RC network. If the magnitude and linearity of $A(f)$ are relatively constant, $T(f)$ increases with the frequency and results in a better input–referred linearity intercept-point of the circuits. Once the frequency increases to a point where the open-loop gain of the amplifier decreases, the loop-gain and linearity performance of the circuit do not increase further. It is worth mentioning that the linearity of $A(f)$ is not constant as a function of frequency, and it affects the overall linearity of the circuit as well. Analysis specifically concerning IIP_2 of a mixer has been extensively performed in [6.11], and many of the considerations can be applied to the present mixer. Since a passive mixer requires a high level of LO drives at the switches, a major concern in this architecture is the LO-RF leakage in the circuit which can degrade IIP_2 of the system due to finite IIP_3 of the front-end blocks [6.12].

6.3 Building Block Designs

In the previous section, we described the architecture with emphasis on system-level tradeoffs in gain, noise, and linearity. In this section, we focus on the implementation of a quadrature demodulator and discuss each of the demodulator building blocks, including the transconductance stage, switching quad, transimpedance amplifier, and LO generation circuits.

6.3.1 Transconductance

Figure 6.3 shows the transconductance stage of the mixer. It consists of a differential complementary pair and a common-mode feedback circuit. The RF and the LO signals are AC-coupled into the mixer core through several linear metal-insulator-metal (MIM) capacitors. AC coupling increases biasing flexibility and suppresses low-frequency distortion interaction between stages. The current from the transconductance stage, however, is DC-coupled to the switching pairs. With no capacitor between the stages (used for DC blocking), we realize minimum parasitic capacitance at the transconductance stage output, C_{par}, by reducing the signal routing. It was shown earlier in [6.3] and in (6.10) that SNR degradations of the signal due to op-amp noise will increase when the value of C_{par} increases.

Unlike narrow-band designs, C_{par} cannot be easily tuned out by using an inductor for all the possible operating frequencies. Since the op-amp is required to have low power consumption, it also contributes a nontrivial portion of the mixer noise, especially in the $1/f$ region. Minimizing C_{par} allows a less stringent noise specification for the op-amp, which favorably translates into a lower-power-consumption circuit design. On the other

hand, the absence of DC blocking capacitors results in non-zero DC bias current flowing through the switches. This current should be minimized in order to reduce 1/*f* noise contributions from the switches, and this was done by careful design of common-mode feedback circuits in both the op-amp and the transconductor.

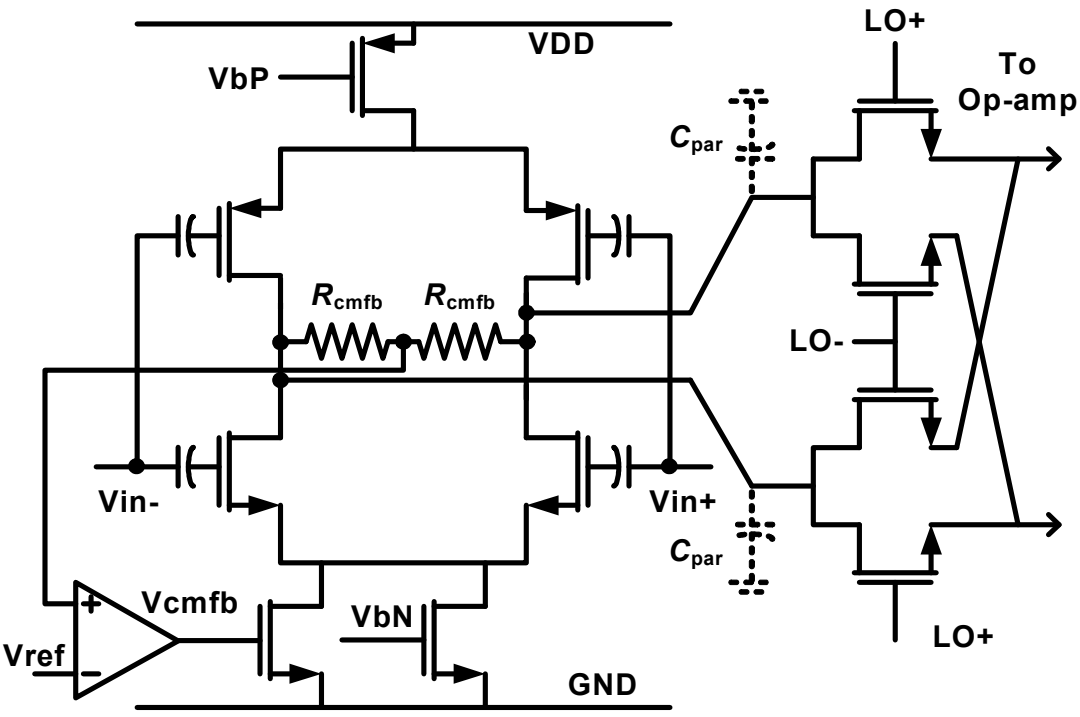

Figure 6.3 Transconductance and switching stages.

Since there is no AC coupling capacitor between this stage and the switches, low-frequency intermodulation tones created by second-order nonlinearity (due to mismatches) will transfer to the next stages downstream. Thus it is important to reduce the second-order nonlinearity in this stage by using a fully differential topology. Although using the fully differential topology requires extra headroom for the pair due to current-source biasing, the RF voltage swings at this stage are low due to the virtual

ground set by an operational amplifier. The NMOS and PMOS devices are biased at the high overdrive V_{gs}-V_{th} region in order to achieve high linearity [6.8]. The common-mode voltages at the mixer and the operational amplifier outputs are set at $V_{dd}/2$ in order to obtain the highest possible headroom for voltage swing. The I/Q mixer and all of the bias circuits together consume 10 mA.

6.3.2 Switches

The switches consist of four transistors forming a double-balanced structure. The DC bias level at the gate of the switches is set at a level where the switches are operating near the threshold of conduction in order to achieve the lowest on-resistance while preventing overlapping on-periods. The overlapping on-periods of the switches result in lowered conversion gain and increased flicker noise from the LO port, while an overlapping off-period will result in linearity degradation [6.13]. To ensure that the bias voltage tracks with process variation, it is generated by a replica bias circuit, as shown in figure 6.4. As mentioned in the previous section, the common-mode voltage level at the drains and sources of the switches is chosen to be $V_{dd}/2$ in order to obtain the highest voltage headroom at the output of the transconductance stage. Assuming the highest allowable gate voltage is V_{dd}, the highest overdrive voltages of the switches will be V_{dd}-$V_{dd}/2$-V_{th}. If the voltage headroom is not a constraint, common-mode voltage level can be reduced to allow higher LO voltage swing and higher overdrive voltage of the switches (as high as $V_{dd}/2$ for the overdrive). Higher overdrive voltage results in lower average on-resistance of the switches and increases linearity, gain, and noise performance of the mixer.

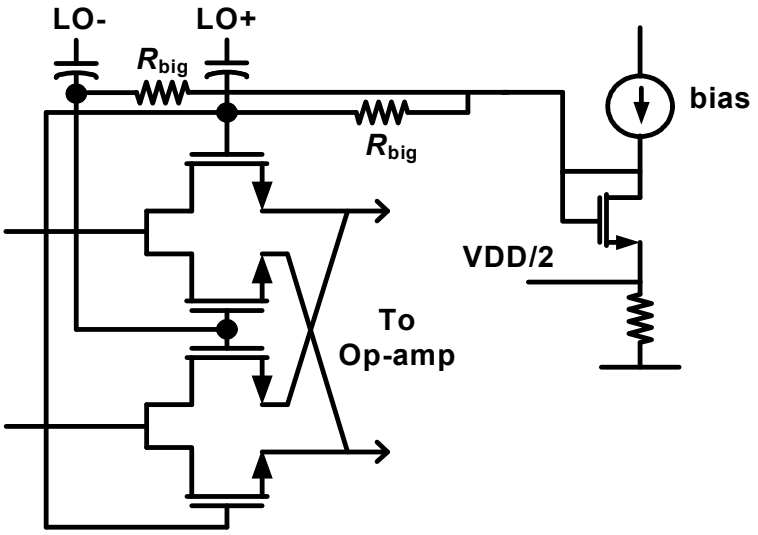

Figure 6.4 Replica bias configuration

The switches are sized large enough to minimize the on-resistance. However, LO power consumption and noise contributions from the operational amplifier determine an upper limit on the size, due to associated parasitic capacitances.

6.3.3 Op-amp and the feedback network

The schematic of the op-amp in figure 6.5 shows the two-stage topology chosen for the op-amp design to obtain both high output voltage swing and low input-referred noise.

The input-referred spot noise of the operational amplifier is given by [6.14].

$$\overline{V}_{n,amp}^2 = 8kT\gamma \frac{1}{g_{mN}^2}\left(\frac{1g_{mN}}{\alpha_N} + \frac{g_{mP}}{\alpha_p}\right)\Delta f + \frac{2}{fC_{\text{ox}}}\left(\frac{K_N}{(WL)_N} + \frac{K_P}{(WL)_P}\frac{g_{mP}^2}{g_{mN}^2}\right)\Delta f \qquad (6.13)$$

where K_P and K_N are process-dependent constants, α is the ratio g_m/g_{ds0}, and C_{ox} is the gate oxide capacitance per unit area. In order to reduce the op-amp noise contribution, the input NMOS transistors were sized to have a high (W/L) ratio with a long channel length, while the PMOS have a low (W/L) ratio with a long channel length.

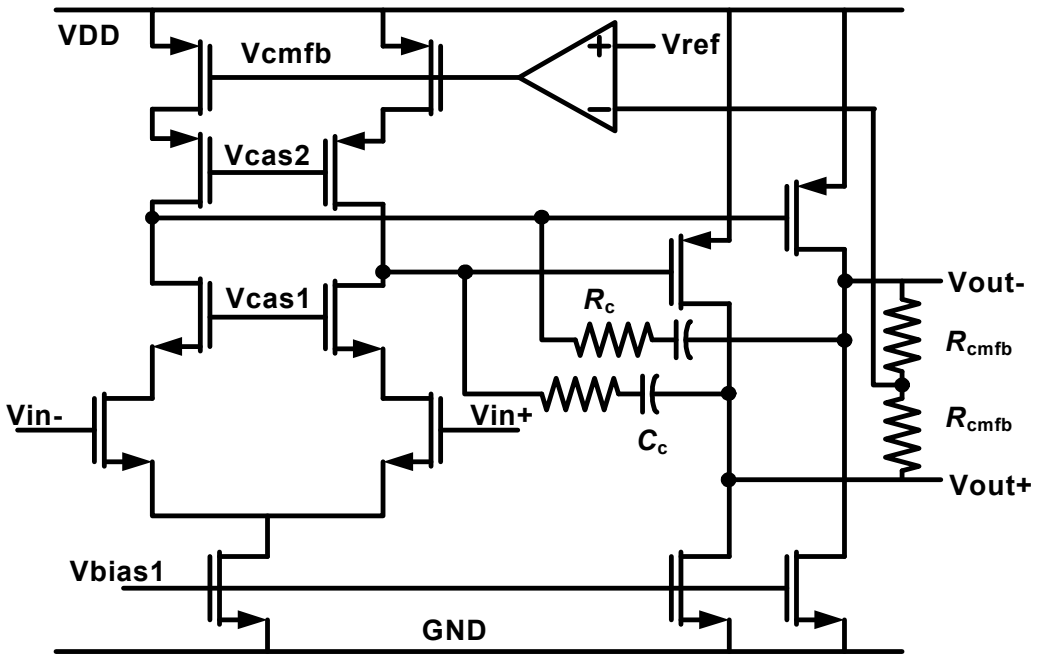

Figure 6.5 Simplified operational amplifier schematic

The output stage of the amplifier is simply a common-source stage and provides almost rail-rail output swing. The feedback resistors were chosen to be large in order to reduce the associated thermal noise, as shown in (6.5) and (6.10). The upper limit of the resistor value was set by the linearity of the circuits. The feedback capacitors are large in order to attenuate the out-of band blockers [6.15]. Although using large feedback capacitors creates a low-frequency gain roll-off at the baseband output, this can be

characterized and corrected in later stages as long as the noise figure is low and the gain is high enough for the baseband frequency of interests. In practice, the available chip area and gain of the circuit determine the upper limit of the capacitor value. The two op-amps (I/Q) draw a total of 3.5 mA from the supply.

6.3.4 Frequency Divider and LO Buffers[1]

The LO generation path of the mixer is as shown in figure 6.6a. The first two inverters in parallel act as the input buffer to reshape the high-frequency waveform that is distorted by the parasitics of the packaged pin, bond wire, and pad. A symmetric LO waveform is critical to ensure balanced switch operation so that the switching quad itself does not degrade the mixer noise figure and create second-order intermodulation products [6.7][6.11]. A divide-by-two frequency scheme is employed in order to produce a 50% LO duty cycle to minimize LO asymmetries. The internal LO frequency ranges from 700 MHz to 2.5 GHz, while the divider operates between 1.4 GHz and 5 GHz. This translates into higher power consumption and a need for a larger balun bandwidth. For testing purposes, multiple baluns were used to accommodate the entire frequency range.

The divide-by-two was implemented in Current Mode Logic (CML) style. The core of the divider block (shown in figure 6.6b) consists of two CML latches with the output cross-toggled back to their inputs. The CML latch circuit diagram is shown in figure 6.6(c). The CML divider draws constant current and has the advantage of generating fewer current spikes during its dynamic operation, which may propagate and appear as noise to other sensitive RF nodes. Because differential signaling is utilized in the CML divider, both I and Q LO outputs with good matching are available. A level

(1) The works on frequency divider and LO buffers have been done by Wei-Hung Chen.

converter, placed between the input inverter and CML divider, brings signal from the CMOS logic to the CML domain. It consists of two CML stages cascaded as in figure 66(c), but without the clocked gate.

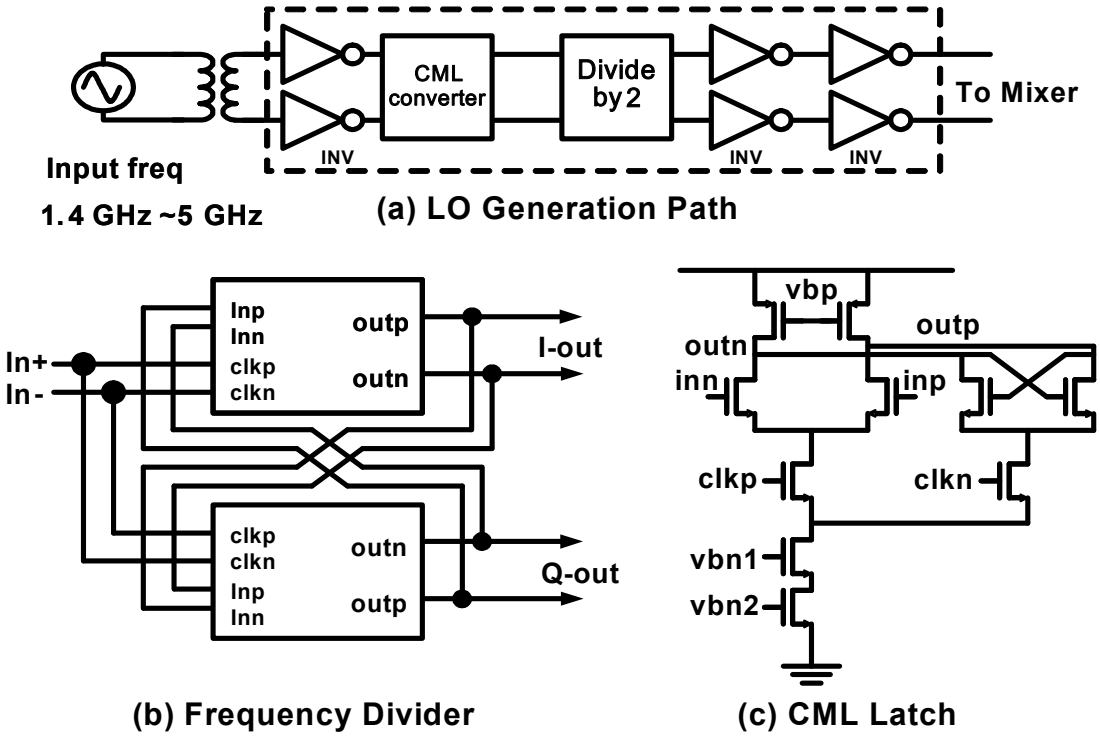

Figure 6.6 LO generation circuitry

A larger LO swing expedites the switching quad transition and helps improve the mixer noise figure and second-order intermodulation product [6.7][6.11]. The mixer core design requires a LO differential swing of at least 1.5 $V_{pk\text{-}pk}$ from a supply of 1.5 V. Two scaled inverters are cascaded in each path to provide sufficient drive capability. The CML circuits (I/Q) consume a total of 1.43 mA.

6.4 Experimental Results

6.4.1. Measurement Setup

The prototype chip was fabricated in a 0.13 μm CMOS technology and occupies a total area of 0.8 mm by 1 mm. The die microphotograph is shown in figure 6.7. All the signal and bias pads were ESD-protected. Sixty percent of the chip area was allocated to the feedback capacitors of the operational amplifiers. The packaged chip was mounted on the PCB board for testing, and on-board baluns were used to perform single-ended to differential conversion at the mixer and LO inputs

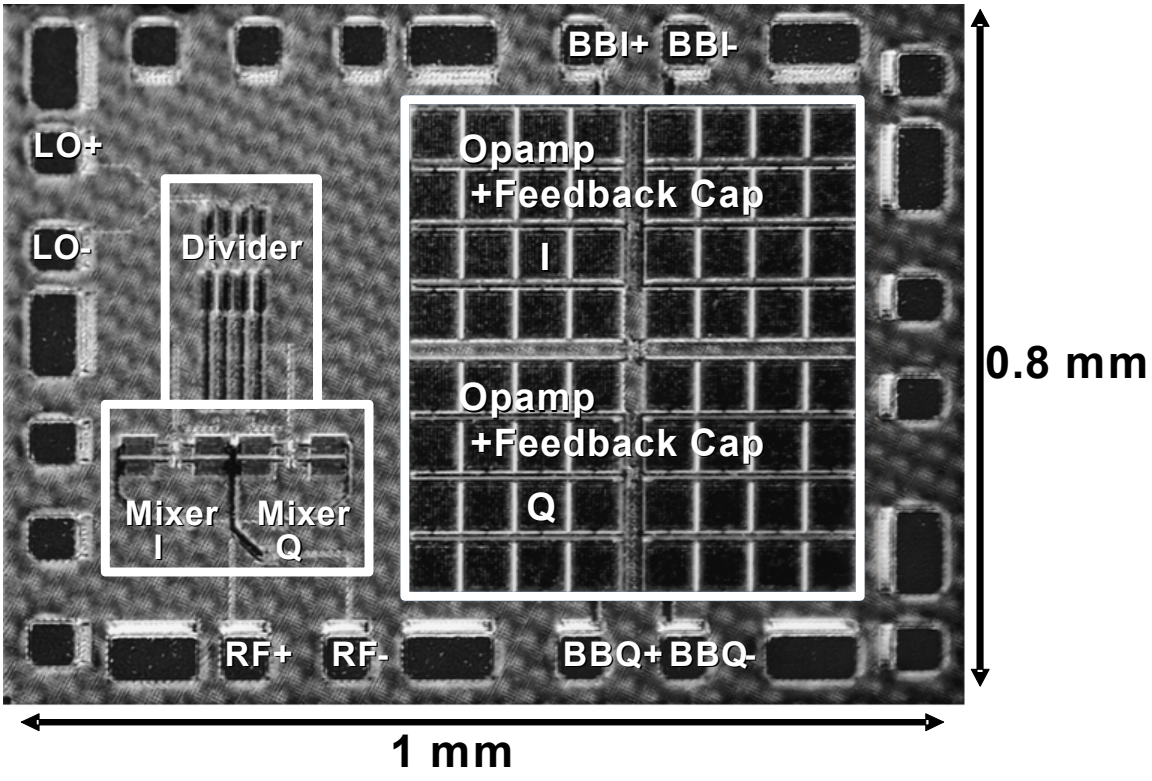

Figure 6.7 Microphotograph of the chip.

An external 100 Ω resistor was placed at the mixer RF input to provide input matching for measurement purposes. At the output of the chip, buffers were used to convert the differential outputs to a single-ended output and to drive low-impedance measurement cables. Noise contributions from the buffers were significant at baseband frequencies higher than 2 MHz, due to mixer gain roll-off, and were de-embedded by estimating the total noise contribution of the buffer from equivalent circuit models obtained from the component provider, and then subtracting it from the output noise. Detailed measurements were done at 900 MHz and 2.1 GHz, near the two ends of the intended operating frequency range. The results can be interpolated into other operating frequencies due to the wideband nature of the circuit.

6.4.2 Measurement Results

Figure 6.8 shows the conversion gain plot for 900 MHz and 2.1 GHz. Conversion gain at 1 kHz and the -3 dB bandwidth of the mixer for inputs from 700 MHz to 2.5 GHz are plotted in figure 6.9. The measured conversion voltage gain is close to 38.5 dB, and the internal voltage gain of the mixer is approximately 3 dB below the measured gain due to the 3 dB voltage gain of the balun.

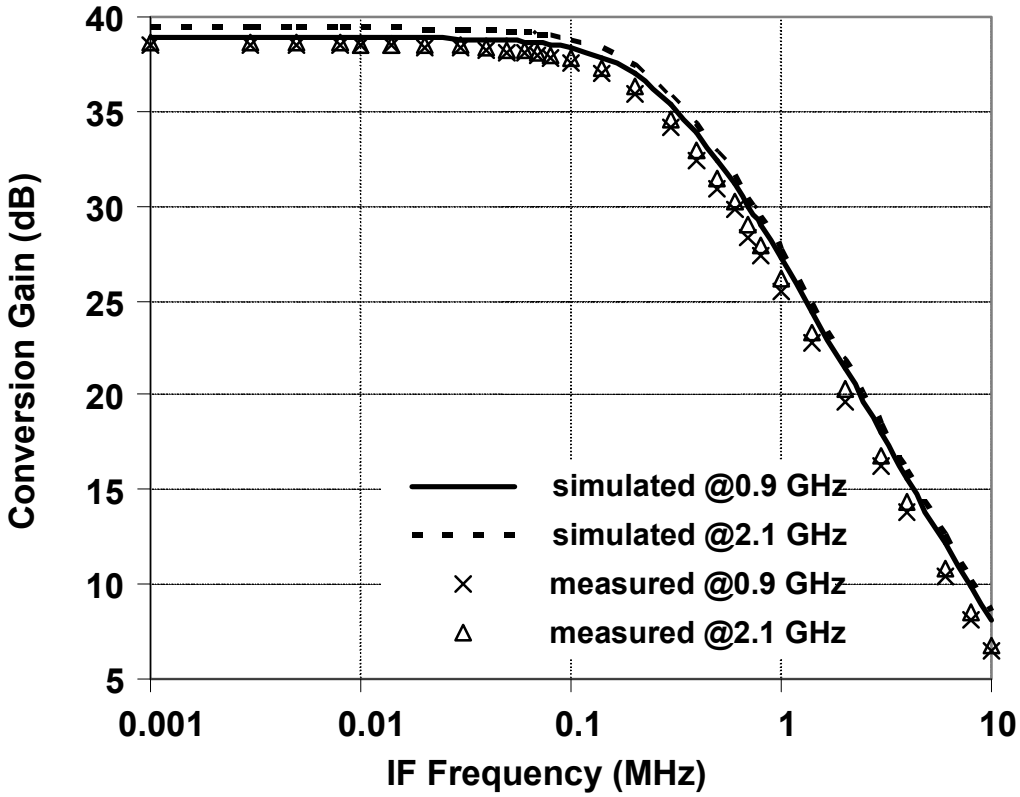

Figure 6.8 Gain plots at 900 MHz and 2.1 GHz f_{LO}

Since the baluns were glued on the same PCB board with the mixer chip, leaving no probing space in between for characterizing the balun loss at different frequencies, the measured mixer gain, noise, and linearity values reported here reflect the combined effect and show a variation of roughly 1 dB. This effect is clearly depicted in figure 6.9. The simulated gain increases with the LO frequency due to high-pass characteristics of the AC coupling networks. Measured gain stays within 1dB of the simulation values and shows the expected variation from balun mismatches, mentioned earlier. The gain drops significantly at 2.5 GHz and is due to the effect of balun loss and the resulting lower LO drives into the switches.

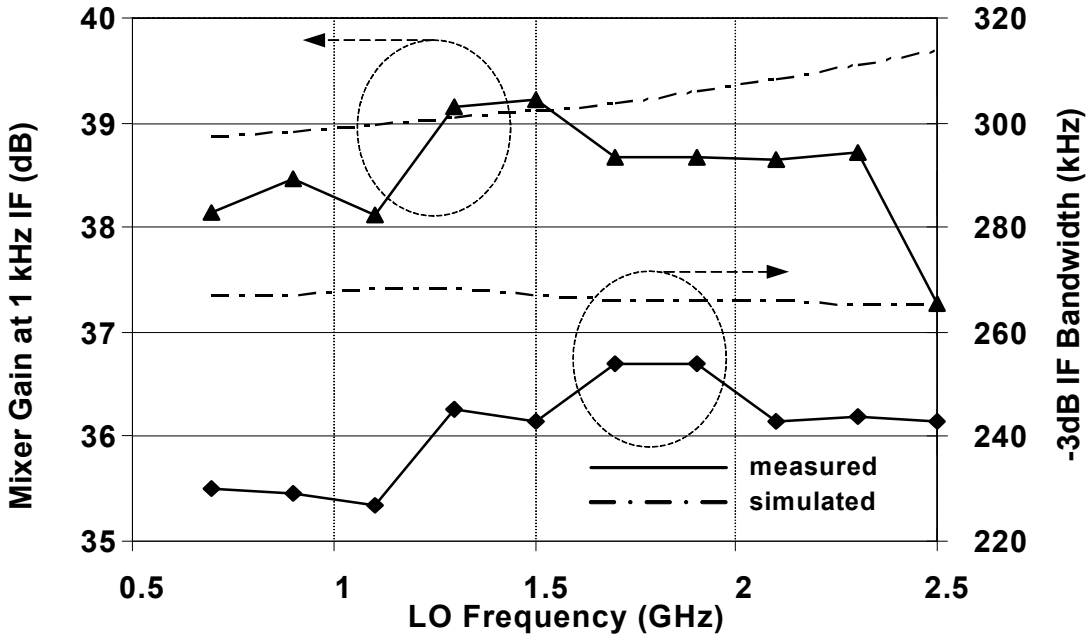

Figure 6.9 Measured conversion gain and bandwidth

Figure 6.10 shows the measured double-sideband noise figures (DSB NF) at 900 MHz and 2.1 GHz. In addition, figure 6.11 shows the DSB NF at 1 MHz baseband frequency and 1/*f* noise corner at different LO frequencies. Variations in noise figure across LO frequencies are due to effects from different balun losses across the frequency range. The measured noise figure floor is near 10 dB, or 2.89 nV/sqrt(Hz), and the 1/*f* noise corner is lower than 35 kHz across the LO frequency range. Taking into account the effect of single-ended to differential conversion, the on-chip input-referred voltage noise floor would be 4.07 nV/sqrt(Hz) assuming a perfect balun were used. The 1/*f* noise increases with higher LO frequency because of higher 1/*f* noise contributions from the operational amplifier as predicted from (6.10). However, the 1/*f* noise corner increases faster than expected as a function of LO frequency, and the potential cause is

parasitic capacitances at the transconductance output. Although not experimentally verified, the amount of 1/*f* noise is expected to rise with the presence of a blocking signal due to higher RMS currents flowing through the switches [6.16]. Measured noise figure increases significantly at 2.5 GHz.

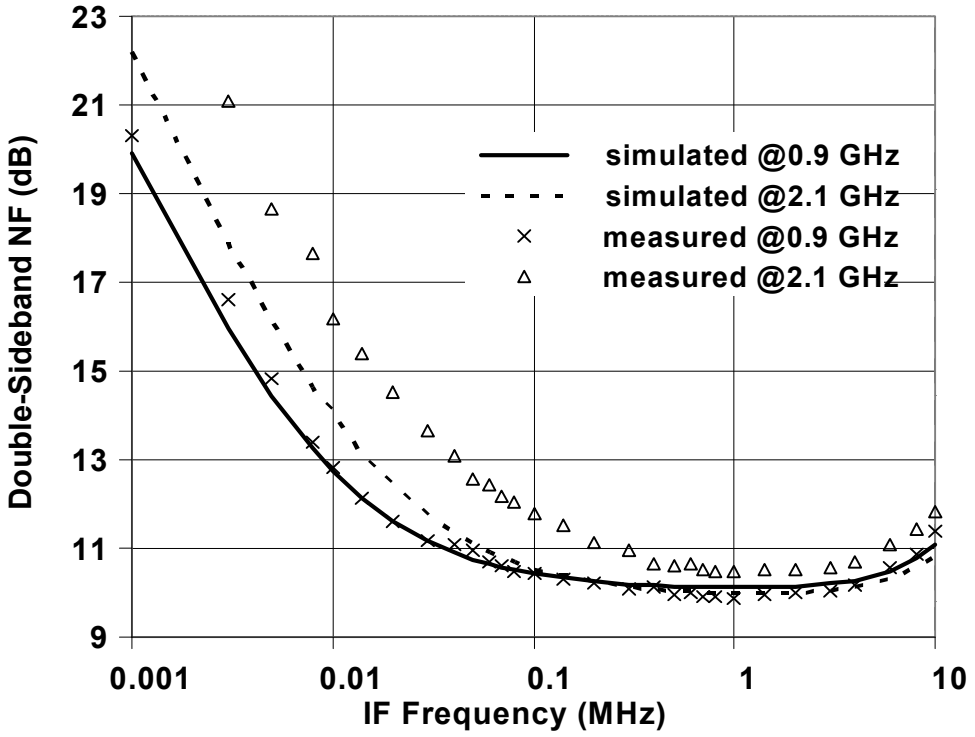

Figure 6.10 Measured double-sideband noise figure at 900 MHz and 2.1 GHz f_{LO}

Figure 6.12 shows the two-tone linearity test results for 900 MHz and 2.1 GHz LO frequencies. The intermodulation (IM) products are located in-band at 30 kHz for all cases. For example, the 1 MHz frequency offset means the input signals are located at 1 MHz and 1.03 MHz offsets for IIP_2 tests, while the input tones for IIP_3 tests are located at 1 MHz and 2.03 MHz offsets. All the input-referred intercept points were calculated from the input-referred powers of the IM products. At very low IF frequency,

IIP_3 and IIP_2 increase as the gain decrease, as suggested by (6.12). Above 2 MHz IF, IIP_3 and IIP_2 flatten or start to decrease due to limitations from the transconductance and the switches' nonlinearity, as well as lowered op-amp loop gain. The op-amp loop gain reduces at high frequency due to gain roll-off in the op-amp open-loop transfer function. At 1 MHz offset, the achieved IIP_3 is +11 dBm, and average IIP_2 is +64 dBm. IIP_2 is measured with five samples, and the minimum is higher than +60 dBm at this frequency. In figure 6.12, an abrupt IIP_3 and IIP_2 dip can be seen at baseband offset around 5 MHz. This is attributed to an unintended peaking in the op-amp's common-mode transfer function. The problem can be prevented in future designs by carefully modifying the common-mode circuit.

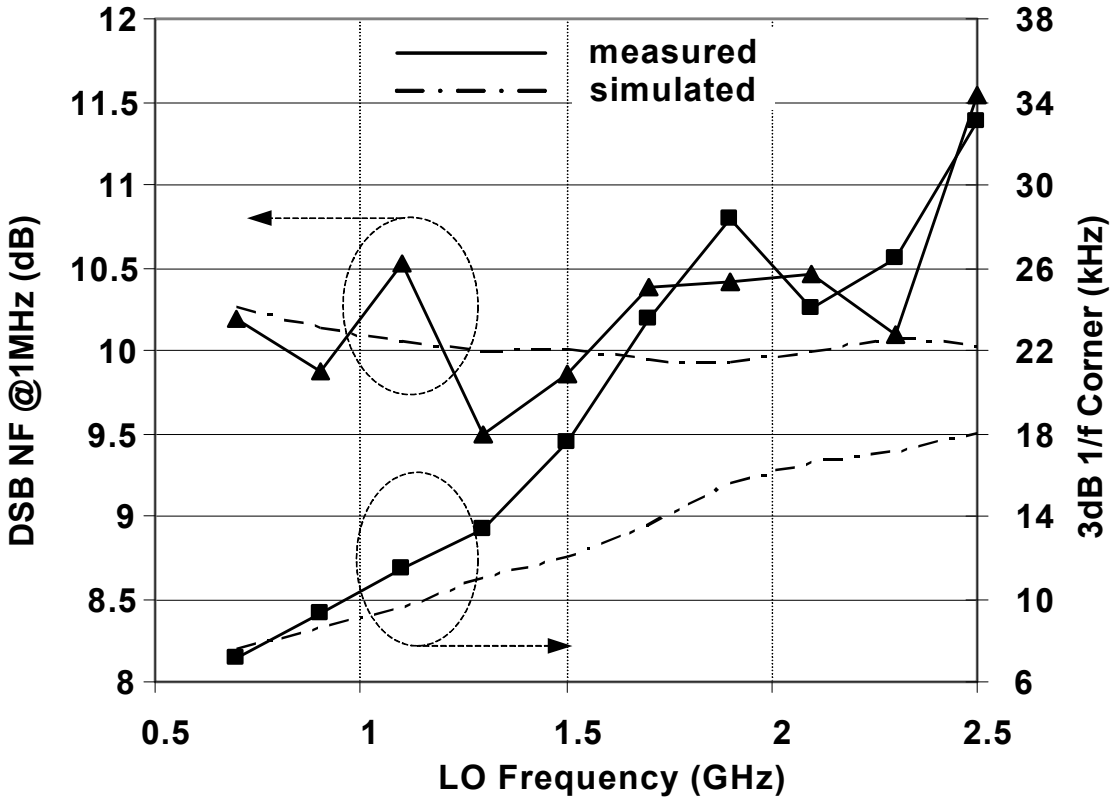

Figure 6.11 Noise characteristics at different f_{LO}

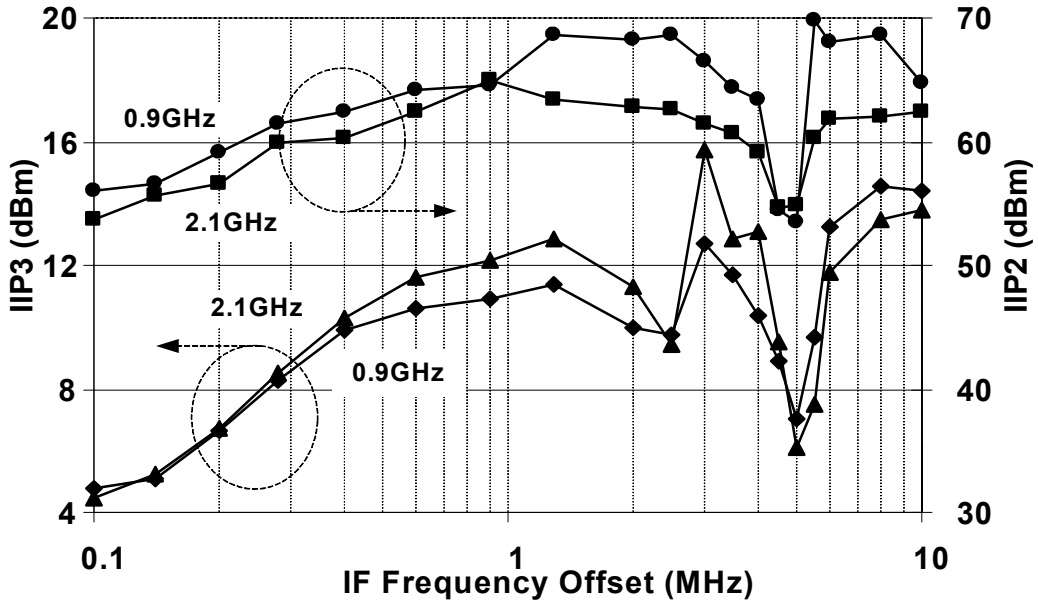

Figure 6.12 Plots of measured IIP_2 and IIP_3 at 900 MHz and 2.1 GHz

The 1 dB compression point (P_{-1dB}) of the circuit is limited by the output swing and varies with the frequency offset of the blocking signals. For 900 MHz f_{LO}, the measured input-referred P_{-1dB} at 100 kHz, 1 MHz, and 10 MHz offsets is -25.8 dBm, -13.5 dBm, and -5.6 dBm, respectively. At the input power of -26 dBm, the output voltage is approximately 0.7 Vp-p on each side of the differential outputs. At this condition, the gain of the transimpedance amplifier drops rapidly as a function of V_{out} amplitude, and the compression is caused by higher-order distortions as well as rapidly decreasing loop gain at the same time. In other words, feedback does not help linearize the circuit at very high output voltage levels, due to significant gain compression in the "feed forward" path. As the blocker offset moves from 0.1 MHz to 1 MHz, IIP_3 increases by 7 dB while P_{-1dB} increases by 12 dB. Similarly, IIP_3 increases by less than 3dB but P_{-1dB} increases by 8 dB when the offset moves from 1 MHz to 10

MHz. The compression point can be increased by either decreasing Z_f or decreasing the transconductance of the input stage. Both methods have negative effects on the noise figure, but the effect can be low depending on how much noise is contributed by Z_f and by the op-amp.

The measured LO leakage at the RF port was -74 dBm on average, with a maximum value of -62 dBm. The measured output DC offset is 19.5 mV_{rms}. The measured I-Q gain imbalance at 100 kHz offset varies from 0.03 dB to 0.1 dB with different LO frequencies. The phase imbalance, however, varies strongly from 0.3° to 10° with different baluns, LO frequencies, and external LO power at 2 f_{LO}. The variation in phase matching comes from the duty cycle error of the signal hitting the on-chip LO divider, and can be solved by using an on-chip divide-by-four circuit to generate I-Q LO drives. The measured performance is summarized in Table 6.1. The total chip, including bias circuitry, consumes 20 mA at 700 MHz and 24 mA at 2.5 GHz from a 1.5 V supply. The highest operating frequency is up to 2.56 GHz and is limited by the frequency divider.

TABLE 6.1

DEMODULATOR PERFORMANCE SUMMARY

Specification		Value
Process Technology		0.13 μm CMOS
Supply Voltage		1.5 V
Total Bias Current		20 mA – 24 mA
Voltage conversion gain		35.5 dB
Output -3 dB Bandwidth		250 kHz
Operating Frequency		0.7 GHz - 2.56 GHz
IIP_3@ 1 MHz Offset	0.9 GHz	11 dBm
	2.1 GHz	12 dBm
IIP_2@ 1 MHz Offset	0.9 GHz	60 dBm minimum
	2.1 GHz	
DSB NF@ 1 MHz Offset	0.9 GHz	10 dB
	2.1 GHz	10.5 dB
$1/f$ 3 dB Corner	0.9 GHz	10 kHz
	2.1 GHz	26 kHz
LO Leakage at RF Port		-74 dBm rms

6.5 References

[6.1] S. Zhou and M. F. Chang, "A CMOS Passive Mixer with Low Flicker Noise for Low-Power Direct-Conversion Receiver," *IEEE J. Solid-State Circuits*, vol. 40, no. 5, pp. 1084-1093, May 2005.

[6.2] M. Valla, G. Montagna, R. Castello, R. Tonietto, and I. Bietti, "A 72-mW CMOS 802.11a Direct-Conversion Front-End With 3.5-dB NF and 200-kHz 1/*f* Noise Corner," *IEEE J. Solid-State Circuits*, vol. 40, no. 4, pp. 970-977, Apr. 2005.

[6.3] E. Sacchi, I. Bietti, S. Erba, L. Tee, P. Vilmercati, and R. Castello, "A 15mW, 70kHz 1/*f* Corner Direct Conversion CMOS Receiver," in *Proc. IEEE Custom Integrated Circuits Conf.*, San Jose, CA, Sep. 2003, pp. 459-462.

[6.4] V. Vidojkovic, J. Tang, A. Leeuwenburgh, and A. H. M. Roermund, "A Low Voltage Folded-Switching Mixer in 0.18-μm CMOS," *IEEE J. Solid-State Circuits*, vol. 40, no. 6, pp. 1259-1264, June 2005.

[6.5] D. Manstretta, R. Castello, and F. Svelto, "Low 1/*f* Noise CMOS Active Mixers for Direct Conversion," *IEEE Trans. Circuits Systs. II, Analog Digit. Signal Process.,* vol. 48, no. 9, pp. 846-850, Sep. 2001.

[6.6] T. H. Lee. *The Design of CMOS Radio-Frequency Integrated Circuits*, 1st ed. Cambridge University Press, 1998.

[6.7] H. Darabi and A. A. Abidi, "Noise in RF-CMOS Mixers: A Simple Physical Model," *IEEE J. Solid-State Circuits*, vol. 35, no. 1, pp. 15-25, Jan. 2000.

[6.8] M. Brandolini, P. Rossi, D. Sanzogni, and F. Svelto, "A +78 dBm IIP2 CMOS Direct Conversion Mixer for Fully Integrated UMTS Receivers," *IEEE J. Solid-State Circuits*, vol. 41, no. 3, pp. 552-559, Mar. 2006.

[6.9] M. T. Terrovitis and R. G. Meyer, "Intermodulation Distortion in Current-Commutating CMOS Mixers," *IEEE J. Solid-State Circuits,* vol. 35, no. 10, pp. 1461-1473, Oct. 2000.

[6.10] P. Gray, P. Hurst, S. Lewis, and R. Meyer. *Analysis and Design of Analog Integrated Circuits*, 4th ed., New York, Wiley, 2001.

[6.11] D. Manstretta, M. Brandolini, and F. Svelto, "Second-Order Inter-modulation Mechanisms in CMOS Downconverters," *IEEE J. Solid-State Circuits*, vol. 38, no. 3, pp. 394-406, Mar. 2003.

[6.12] I. Elahi, K. Muhammad, and P.T. Balsara, "IIP2 and DC Offsets in the Presence of Leakage at LO Frequency," *IEEE Trans. Circuits Systs. II, Analog Digit. Signal Process.,* vol. 53, no. 8, pp. 647-651, Aug. 2006.

[6.13] A. Shahani, D.K. Shaeffer, and T.H. Lee, "A 12-mW Wide Dynamic Range CMOS Front-End for a Portable GPS receiver," *IEEE J. Solid-State Circuits*, vol. 32, no. 12, pp. 2061-2070, Dec. 1997.

[6.14] B. Razavi. *Design of Analog CMOS Integrated Circuits*, New York: McGraw-Hill, 2001.

[6.15] V. Aparin *et al.*, "A Fully-Integrated Highly Linear Zero-IF CMOS Cellular CDMA Receiver," in *IEEE Int. Solid-State Circuits Conf. Dig. Tech. Papers*, San Francisco, CA, Feb. 2005, pp. 324-325.

[6.16] D. Leenaerts, and W. Redman-White, "1/f Noise in Passive CMOS Mixers for Low and Zero IF Integrated Receivers," in *Proc. 27th Eur. Solid-State Circuits Conf.,* Villach, Austria, 2001, pp. 103-107.

[6.17] F. Bruccoleri, E. Klumperink, and B. Nauta, "Wide-Band CMOS Low-Noise Amplifier Exploiting Thermal-Noise Canceling," *IEEE J. Solid-State Circuits*, vol. 39, no. 2, pp. 275-282, Feb. 2004.

[6.18] A. Behzad, et al., "Direct-conversion CMOS transceiver with automatic frequency control for 802.11a wireless LANs," in *IEEE Int. Solid-State Circuits Conf. Dig. Tech. Papers*, San Francisco, CA, Feb. 2003, pp. 356-499.

[6.19] S. Peng, C. Chen, and A. Bellaouar, "A Wideband Mixer for WCDMA/CDMA2000 in 90nm CMOS digital CMOS Process," in Proc. *IEEE Radio Frequency Integrated Circuits (RFIC) Symp.*, Jun. 2005, pp. 179-182.

[6.20] A. Amer, E. Hegazi, and H. F. Ragaie, "A 90-nm Wideband Merged CMOS LNA and Mixer Exploiting Noise Cancellation," *IEEE J. Solid-State Circuits*, vol. 42, no. 2, pp. 323-328, Feb. 2007.

7

Wideband CMOS Front-End Analysis and Design

7.1 Introduction

In the previous chapters we reviewed the analysis and design of a wideband quadrature demodulator and a low-noise amplifier as separate building blocks. In this chapter, we will turn to the design of a complete CMOS front-end that includes an LNA, quadrature mixers, and a frequency divider. Starting with architecture considerations, we will then review the circuit and implementation details.

In the next section, we will discuss the architecture of the demodulator, followed by the circuit details of the various blocks, then implementation, measurement results, and conclusions.

7.2 Receiver Front-End Architecture

In order to achieve the highest level of reconfigurability and simplicity, we have chosen a direct-conversion architecture for the front-end. Figure 7.1 shows the block diagram of the circuit; the key building blocks include a low-noise amplifier, a quadrature demodulator, and a 1^{st}-order low-pass filter. The high-level architecture is the same as the demodulator presented in chapter 6, except that a low-noise amplifier is

added in the front-end. The detailed design considerations for these blocks will be discussed in later sections.

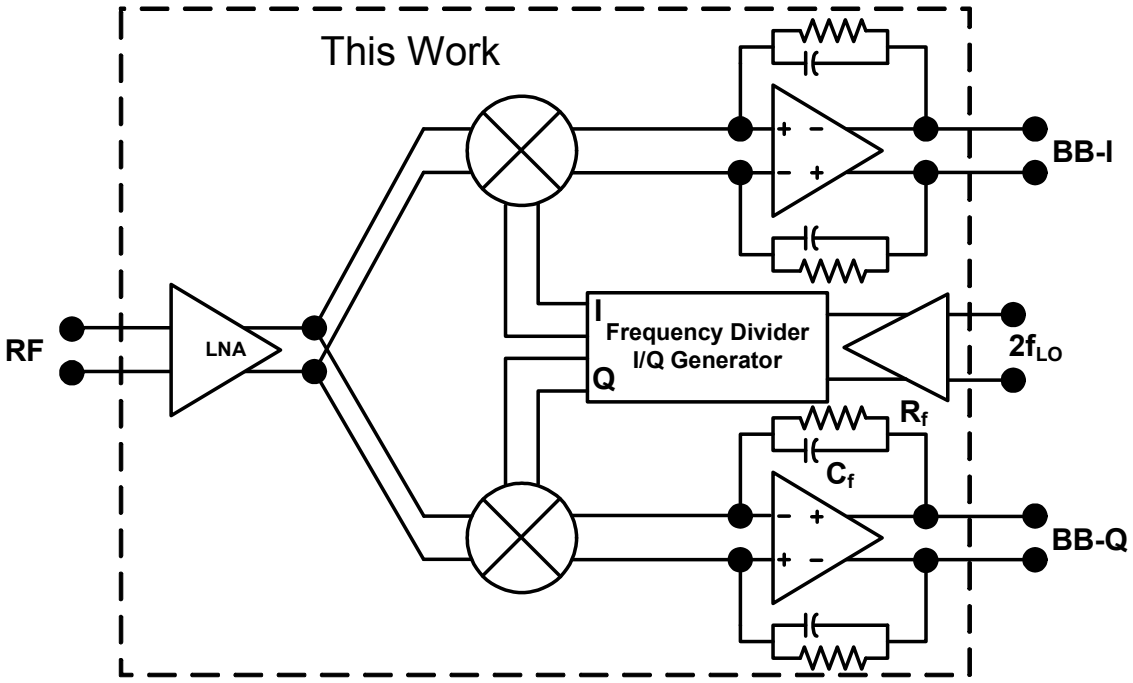

Figure 7.1 Front-end block diagram

7.2.1 Resistive Shunt Feedback Low-Noise Amplifier

Several topologies offer wideband input impedance matching as discussed in chapter 3. However, the resistive-feedback topology has the advantages of simplicity, small die area, and a low achievable noise figure compared to other topologies [7.1][7.2]. In this section, we present an analysis of a basic resistive shunt feedback low-noise amplifier in terms of gain, input impedance, noise, and linearity.

7.2.1.1 Gain and Input Impedance Analysis

Figure 7.2 presents a circuit diagram of a shunt resistive-feedback amplifier. In this analysis, we assume that the operating frequency is "intermediate," which is when the capacitive effects are not significant. Later in the chapter, we will revisit the analysis and estimate the frequency response of the circuit.

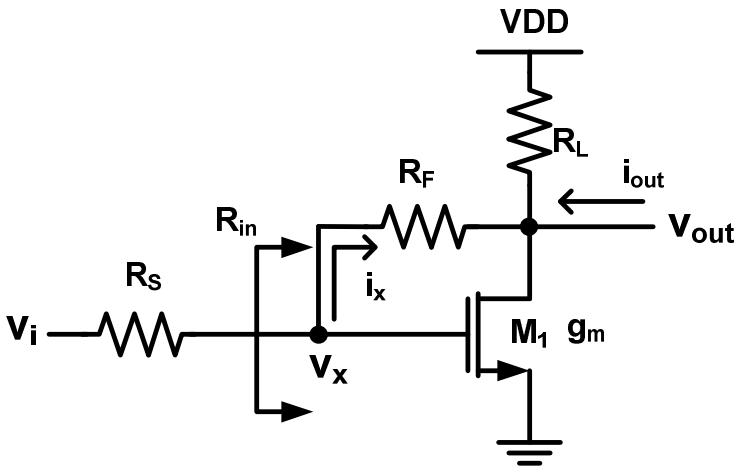

Figure 7.2 A resistive shunt feedback amplifier

Applying KCL at the output node (v_{out}), we have (neglecting the device output impedance):

$$\frac{v_{out}}{R_L} + \frac{v_{out}}{R_F} - \frac{v_x}{R_F} + v_x g_m = 0$$

$$v_x\left(\frac{1 - g_m R_F}{R_R}\right) = v_{out}\left(\frac{R_L + R_F}{R_L R_F}\right)$$

$$\frac{v_{out}}{v_x} = A_V = \frac{R_L\left(1 - g_m R_F\right)}{R_L + R_F} \tag{7.1}$$

Note that (7.1) shows the voltage gain from the gate to the drain of M_1.

Similarly, applying KCL at the gate of M_1 (v_x) yields:

$$\frac{v_x}{R_S}+\frac{v_x}{R_F}-\frac{v_{in}}{R_S}-\frac{v_{out}}{R_F}=0$$

$$v_x\left(\frac{1}{R_S}+\frac{1}{R_F}\right)-v_{in}\left(\frac{1}{R_S}\right)-v_{out}\left(\frac{1}{R_F}\right)=0 \tag{7.2}$$

Applying (7.1) into (7.2), we have:

$$v_{out}\left(\frac{R_L+R_F}{R_L\left(1-g_mR_F\right)}\right)\left(\frac{1}{R_S}+\frac{1}{R_F}\right)-v_{in}\left(\frac{1}{R_S}\right)-v_{out}\left(\frac{1}{R_F}\right)=0$$

$$v_{out}\left(\frac{\left(R_L+R_F\right)\left(R_S+R_F\right)-R_SR_L\left(1-g_mR_F\right)}{R_FR_SR_L\left(1-g_mR_F\right)}\right)=v_{in}\left(\frac{1}{R_S}\right)$$

$$v_{out}=v_{in}\left(\frac{R_L\left(1-g_mR_F\right)}{R_L+R_F+R_S\left(1+g_mR_L\right)}\right) \tag{7.3}$$

To check the limits of (7.3), we will apply two extreme cases of g_m into the equation. If g_m is very large, the expression becomes:

$$v_{out}\Big|_{g_m\to\infty}=v_{in}\left(\frac{-R_Lg_mR_F}{R_Sg_mR_L}\right)=-\frac{R_F}{R_S} \tag{7.4}$$

This is the expected result if we replace M_1 with an ideal operational amplifier. At the other extreme, if g_m is very small we have:

$$v_{out}\big|_{g_m \to 0} = v_{in}\left(\frac{R_L}{R_S + R_F + R_L}\right) \tag{7.5}$$

The results in (7.5) correspond to a simple resistive division between all the resistors from the input to the output (note that VDD is an AC ground), which is to be expected when g_m=0 and the transistor becomes just an open circuit looking into its base and drain.

An observation from (7.3) is that the gain of the circuit becomes zero if $g_m = 1/R_F$. This is the point where the magnitude of the passive gain (through the resistor R_F) equals the active gain (through g_m), but with opposite phase. In most applications, the value of g_m is much higher than $1/R_F$, and the circuit operates as an inverting amplifier.

The input resistance of the amplifier, R_{in}, can be obtained by:

$$R_{in} = \frac{v_x}{i_x} = \frac{v_x}{\left(\frac{v_x - v_{out}}{R_F}\right)} \tag{7.6}$$

Applying (7.1) into (7.6), we have:

$$R_{in} = \frac{v_x}{i_x} = \frac{v_x}{\frac{v_x - v_x\left(\frac{R_L(1 - g_m R_F)}{R_L + R_F}\right)}{R_F}}$$

$$R_{in} = \frac{v_x}{i_x} = \frac{R_F}{1 - \left(\frac{R_L(1 - g_m R_F)}{R_L + R_F}\right)} = \frac{R_F(R_L + R_F)}{R_L + R_F - R_L(1 - g_m R_F)}$$

$$R_{in} = \frac{R_L + R_F}{1 + g_m R_L} \tag{7.7}$$

The output resistance of the amplifier can be calculated in similar fashion:

$$R_{out} = \left.\frac{v_{out}}{i_{out}}\right|_{v_{in}=0} = \frac{v_{out}}{\frac{v_{out}}{R_F} - \frac{v_x}{R_F} + v_x g_m + \frac{v_{out}}{R_L}} \tag{7.8}$$

From (7.2), if v_{in}=0, then v_x can be calculated from the voltage division between R_S and R_F. In this case, we have:

$$R_{out} = \frac{v_{out}}{v_{out}\left(\frac{1}{R_F} + \frac{1}{R_L} + \left(\frac{R_S}{R_S + R_F}\right)\left(g_m - \frac{1}{R_F}\right)\right)}$$

$$R_{out} = \frac{1}{1\left(\frac{1}{R_F}\left(1 - \frac{R_S}{R_S + R_F}\right) + \frac{1}{R_L} + g_m\left(\frac{R_S}{R_S + R_F}\right)\right)}$$

$$R_{out} = \frac{1}{\left(\frac{1}{R_S + R_F} + \frac{1}{R_L} + g_m\left(\frac{R_S}{R_S + R_F}\right)\right)} = \left(R_S + R_F\right) // \frac{1}{g_m}\left(1 + \frac{R_F}{R_S}\right) // R_L \tag{7.9}$$

7.2.1.2 Noise Analysis

Figure 7.3 shows a schematic with major noise sources included. Invoking superposition, we derive the transfer function to the output from each noise source and then combine all noise source powers at the output.

Noise from the input resistor, R_S

The transfer function of the voltage noise $\overline{V_{n,R_S}^2}$ to the output voltage noise $\overline{V_{n,out}^2}$ is the same as the voltage gain of the amplifier shown in (7.3). We then have:

$$\overline{V_{n,out}^2} = \overline{V_{n,R_S}^2}\left(\frac{R_L(1-g_m R_F)}{R_L + R_F + R_S(1+g_m R_L)}\right)^2 \tag{7.10}$$

By modeling $\overline{V_{n,R_S}^2}$ as a thermal noise from R_S, we finally have:

$$\overline{V_{n,out,R_S}^2} = 4kTR_S\left(\frac{R_L(1-g_m R_F)}{R_L + R_F + R_S(1+g_m R_L)}\right)^2 \Delta f \tag{7.11}$$

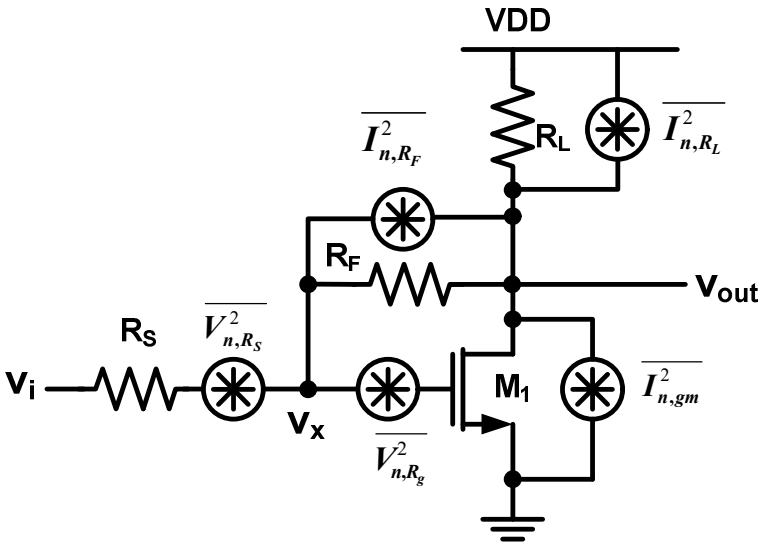

Figure 7.3 Major noise sources in a resistive shunt-feedback amplifier

Noise from the feedback resistor, R_F

In this case, we first need to find the transfer function from $\overline{I_{n,R_F}^2}$ to $\overline{V_{n,out}^2}$. Assuming that the instantaneous i_n noise flows from the V_x node to V_{out} node, applying KCL at V_x node gives:

$$v_x\left(\frac{1}{R_S}+\frac{1}{R_F}\right)+i_n-v_{out}\left(\frac{1}{R_F}\right)=0 \tag{7.12}$$

Similarly, applying KCL at the V_{out} node yields:

$$v_{out}\left(\frac{1}{R_F}+\frac{1}{R_L}\right)-i_n-v_x\left(\frac{1}{R_F}-g_m\right)=0 \tag{7.13}$$

From (7.12) and (7.13), we have:

$$i_n\left(\frac{1}{R_F}-g_m-\frac{1}{R_S}-\frac{1}{R_F}\right)-v_{out}\left(\frac{1}{R_F}\left(\frac{1}{R_F}-g_m\right)-\left(\frac{1}{R_F}+\frac{1}{R_L}\right)\left(\frac{1}{R_S}+\frac{1}{R_F}\right)\right)=0$$

$$v_{out}\left(\frac{g_m}{R_F}+\frac{1}{R_LR_S}+\frac{1}{R_SR_F}+\frac{1}{R_LR_F}\right)=\left(g_m+\frac{1}{R_S}\right)i_n$$

$$v_{out}=\frac{\left(1+g_mR_S\right)}{R_S}\frac{R_LR_SR_F}{R_S+R_L+R_F+g_mR_SR_L}i_n$$

$$v_{out}=\frac{R_LR_F\left(1+g_mR_S\right)}{R_F+R_L+R_S\left(1+g_mR_L\right)}i_n \tag{7.14}$$

From (7.14), we then have:

$$\overline{V_{n,out,R_F}^2}=\left(\frac{R_LR_F\left(1+g_mR_S\right)}{R_F+R_L+R_S\left(1+g_mR_L\right)}\right)^2\overline{I_{n,R_F}^2} \tag{7.15}$$

By modeling $\overline{I_{n,R_F}^2}$ as a thermal noise from R_F, we finally have:

$$\overline{V_{n,out,R_F}^2}=\frac{4kT}{R_F}\left(\frac{R_LR_F\left(1+g_mR_S\right)}{R_F+R_L+R_S\left(1+g_mR_L\right)}\right)^2\Delta f \tag{7.16}$$

Noise from the load resistor, R_L

We first need to find the transfer function from the current noise $\overline{I_{n,R_L}^2}$ to the output voltage noise, $\overline{V_{n,out}^2}$. This is simply:

$$\overline{V_{n,out,R_L}^2} = R_{out}^2 \overline{I_{n,R_L}^2} \tag{7.17}$$

$$\overline{V_{n,out,R_L}^2} = \frac{1}{\left(\frac{1}{R_S+R_F}+\frac{1}{R_L}+g_m\left(\frac{R_S}{R_S+R_F}\right)\right)^2}\overline{I_{n,R_L}^2}$$

$$\overline{V_{n,out,R_L}^2} = \frac{R_L^2\left(R_S+R_F\right)^2}{\left(R_L+R_F+R_S\left(1+g_mR_L\right)\right)^2}\overline{I_{n,R_L}^2} \tag{7.18}$$

By modeling $\overline{I_{n,R_L}^2}$ as a thermal noise from R_L, we finally have:

$$\overline{V_{n,out,R_L}^2} = \frac{4kTR_L\left(R_S+R_F\right)^2}{\left(R_L+R_F+R_S\left(1+g_mR_L\right)\right)^2}\Delta f \tag{7.19}$$

Drain current noise from the transistor M_1

The transfer function from the drain current noise $\overline{I_{n,g_m}^2}$ to the output is the same as the transfer function from $\overline{I_{n,R_L}^2}$ to the output. As a result, we have:

$$\overline{V_{n,out,g_m}^2} = \frac{R_L^2\left(R_S+R_F\right)^2}{\left(R_L+R_F+R_S\left(1+g_mR_L\right)\right)^2}\overline{I_{n,g_m}^2} \tag{7.20}$$

Using

$$\overline{I_{n,g_m}^2} = 4kT\gamma g_{ds0}\Delta f$$

We then have:

$$\overline{V_{n,out,g_m}^2} = \frac{4kT\gamma g_{ds0} R_L^2 (R_S + R_F)^2}{(R_L + R_F + R_S(1 + g_m R_L))^2} \Delta f \tag{7.21}$$

Defining $\alpha = g_m/g_{ds0,}$ the above equation becomes:

$$\overline{V_{n,out,g_m}^2} = \frac{4kT\gamma g_m R_L^2 (R_S + R_F)^2}{\alpha(R_L + R_F + R_S(1 + g_m R_L))^2} \Delta f \tag{7.22}$$

Gate noise from the transistor M_1

The transfer function of gate voltage noise $\overline{V_{n,r_g}^2}$ to the output can be derived by first applying the KCL at the output node:

$$\frac{v_{out}}{R_L} + \frac{v_{out}}{R_F} - \frac{v_x}{R_F} + (v_x - v_{n,r_g}) g_m = 0 \tag{7.23}$$

Note that an instantaneous polarity of $v_{n,rg}$ is assumed in the above equation. By inspection that v_x can be calculated from voltage division between R_S and R_F:

$$\frac{v_{out}}{R_L} + \frac{v_{out}}{R_F} + v_{out}\left(\frac{R_S}{R_S + R_F}\right)\left(g_m - \frac{1}{R_F}\right) - g_m v_{n,r_g} = 0$$

$$v_{out}\left(\frac{1}{R_F} + \frac{1}{R_L}\left(\frac{R_S}{R_S + R_F}\right)\left(g_m - \frac{1}{R_F}\right)\right) - g_m v_{n,r_g} = 0 \tag{7.24}$$

Applying (7.9) into (7.23), we have:

$$v_{out} = g_m R_{out} v_{n,r_g} \tag{7.25}$$

The noise transfer function can then be expressed as:

$$\overline{V_{n,out,r_g}^2} = g_m^2 R_{out}^2 \overline{V_{n,r_g}^2} \tag{7.26}$$

Using the gate noise expression from chapter 3, we then have:

$$\overline{V_{n,out,r_g}^2} = g_m^2 4kT\delta\left(\frac{1}{5g_{ds0}}\right)\frac{R_L^2\left(R_S+R_F\right)^2}{\left(R_L+R_F+R_S\left(1+g_mR_L\right)\right)^2}\Delta f$$

$$\overline{V_{n,out,r_g}^2} = \frac{1}{5}\frac{4kTg_m\delta\alpha R_L^2\left(R_S+R_F\right)^2}{\left(R_L+R_F+R_S\left(1+g_mR_L\right)\right)^2}\Delta f \tag{7.27}$$

Input Referred Noise and Noise Figure

The total output noise can be obtained by combining the results from (7.11), (7.16), (7.19), (7.22), and (7.27):

$$V_{n,out,tot}^2 = \frac{4kT\Delta f}{\left(R_L+R_F+R_S\left(1+g_mR_L\right)\right)^2}\begin{pmatrix} R_SR_L^2\left(1-g_mR_F\right)^2+R_FR_L^2\left(1+g_mR_S\right)^2 \\ +R_L\left(R_S+R_F\right)^2+\frac{\gamma g_m}{\alpha}R_L^2\left(R_S+R_F\right)^2 \\ +\frac{1}{5}\delta\alpha g_mR_L^2\left(R_S+R_F\right)^2 \end{pmatrix} \tag{7.28}$$

Dividing (7.28) by the voltage gain of the circuit (7.3), we get:

$$V_{n,in,tot}^2 = \frac{4kT\Delta f}{R_L^2\left(1-g_mR_F\right)^2}\begin{pmatrix} R_SR_L^2\left(1-g_mR_F\right)^2+R_FR_L^2\left(1+g_mR_S\right)^2 \\ +R_L\left(R_S+R_F\right)^2+\frac{\gamma g_m}{\alpha}R_L^2\left(R_S+R_F\right)^2 \\ +\frac{1}{5}\delta\alpha g_mR_L^2\left(R_S+R_F\right)^2 \end{pmatrix}$$

$$V_{n,in,tot}^2 = \frac{4kT\Delta f}{\left(1-g_m R_F\right)^2}\left(\begin{array}{l} R_S\left(1-g_m R_F\right)^2 + R_F\left(1+g_m R_S\right)^2 \\ +\frac{1}{R_L}\left(R_S+R_F\right)^2 + \frac{\gamma g_m}{\alpha}\left(R_S+R_F\right)^2 \\ +\frac{1}{5}\delta\alpha g_m\left(R_S+R_F\right)^2 \end{array}\right) \tag{7.29}$$

To obtain the noise factor, we then divide the total noise by the noise contributions from the source resistance:

$$F = 1+\frac{1}{R_S\left(1-g_m R_F\right)^2}\left(R_F\left(1+g_m R_S\right)^2 + \left(R_S+R_F\right)^2\left(\frac{1}{R_L}+\frac{\gamma g_m}{\alpha}+\frac{\delta\alpha g_m}{5}\right)\right) \tag{7.30}$$

If $g_m R_F >> 1$, we can simplify (7.30) as:

$$F = 1+\frac{1}{R_S R_F}\left(\frac{1}{g_m}+R_S\right)^2 + \frac{1}{R_S}\left(1+\frac{R_S}{R_F}\right)^2\left(\frac{1}{g_m^2 R_L}+\frac{\gamma}{\alpha g_m}+\frac{\delta\alpha}{5g_m}\right) \tag{7.31}$$

Equation (7.31) suggests that the noise factor of the resistive shunt-feedback amplifier always decreases when G_F (1/ R_F) or g_m increases. R_S is usually fixed at or near 50 Ω, and $g_m R_L$ is usually much greater than $\gamma/\alpha + \delta\alpha/5$. As a result, the noise factor of an amplifier is almost entirely determined by the values of R_F and g_m for a given process technology.

To minimize the noise figure of the amplifier, it is absolutely necessary to minimize the gate and substrate resistance of the input transistor (M_1) as much as possible. Gate resistance can be reduced by using a small transistor width per finger and by using double contacts at the gates. For substrate resistance minimization, it is imperative to put substrate contacts as close to the transistors as possible. Although the

effects of body-source substrate resistance noise are not included in (7.31), they can be modeled as a current noise source in parallel with $\overline{I_{n,g_m}^2}$ as:

$$\overline{I_{n,rsub}^2} = 4kTR_{SUB}g_{mbs}^2 \tag{7.32}$$

where R_{SUB} is the substrate resistance and g_{mbs} is the body-effect transconductance.

7.2.1.2 Design steps for noise and gain performance

In most cases, the key specifications in an LNA design are the input matching, gain, and noise performance, as it needs to interface with off-chip components as well as provide low-noise amplification of the incoming signal. For a resistive shunt-feedback LNA, important design equations include (7.1), (7.7), and (7.31), and they are repeated as follows:

$$\frac{v_{out}}{v_x} = A_V = \frac{R_L(1-g_mR_F)}{R_L+R_F} \tag{7.1}$$

$$R_{in} = \frac{R_L+R_F}{1+g_mR_L} \tag{7.7}$$

$$F = 1+\frac{1}{R_SR_F}\left(\frac{1}{g_m}+R_S\right)^2+\frac{1}{R_S}\left(1+\frac{R_S}{R_F}\right)^2\left(\frac{1}{g_m^2R_L}+\frac{\gamma}{\alpha g_m}+\frac{\delta\alpha}{5g_m}\right) \tag{7.31}$$

If the input resistance and the voltage gain of the amplifier are specified, we can find R_F from the concept of Miller multiplication [7.3] as:

$$R_F = R_{in}(1-A_V) \tag{7.33}$$

An observation from (7.33) is that the value of R_F is independent of g_m once the gain and input resistance are chosen. In most cases, R_{in} is designed to be the same or close to R_S due to the input impedance-matching constraint. We will later show that setting R_{in} higher than R_S results in a lower noise figure of the circuit.

The next design step is to select the g_m that results in the desired noise figure, by using (7.31). The value of R_{in} for a given g_m, R_F, and R_{in} could be obtained using (7.7). For example, if the required voltage gain is 18 dB (inverting) with $R_{in} = R_S = 50\ \Omega$, and process parameters of γ=2, α=1, and δ=4 result in R_F=447, the plot of noise figure versus g_m can be calculated as shown in figure 7.4.

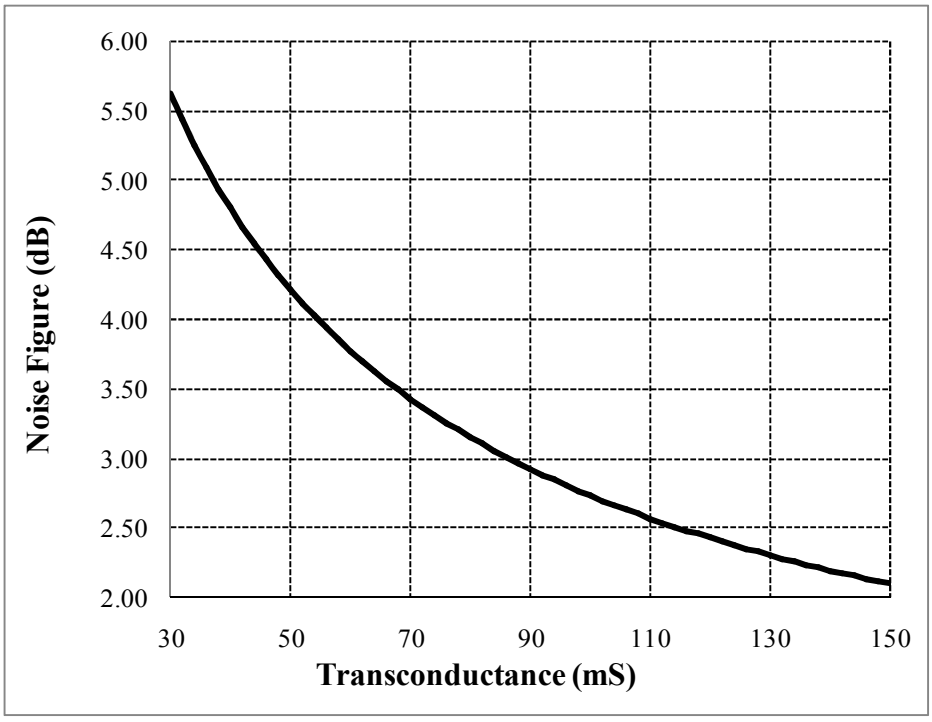

Figure 7.4 NF versus transconductance of a shunt-feedback amplifier

It is clear from figure 7.4 that there is a tradeoff between the noise figure and transconductance. In this case, we need g_m ~ 140 mS in order to achieve 2.5 dB noise figures.

In practice, R_{in} can be set a little higher or lower than R_S while maintaining better than -10 dB of input S_{11}. For instance, R_{in} of 1.5 R_S yields S_{11} of -14 dB. The benefit of using higher R_{in} is that R_F becomes higher, hence a lower noise figure could be obtained using the same g_m (or bias current). Figure 7.5 shows plots of amplifier noise figures versus device g_m for various R_{in}. The noise figure can also be reduced by increasing the gate-to-drain voltage gain of the circuit. By increasing the voltage gain, the required R_F becomes larger, resulting in lower noise contribution to the output.

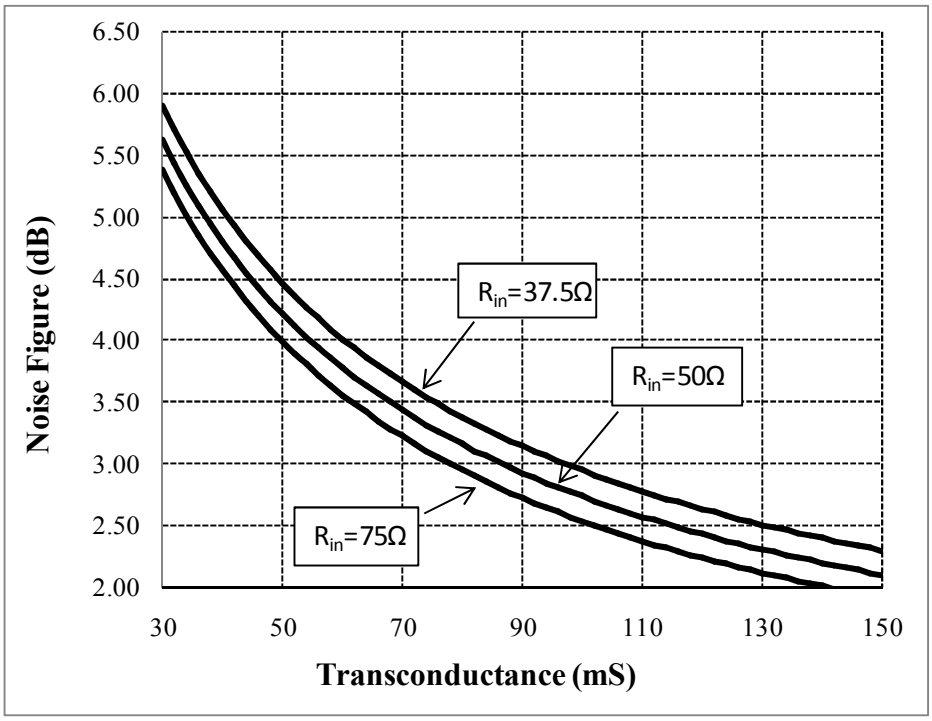

Figure 7.5 NF-g_m plots for different input resistance

Once the g_m of the transistor is chosen, we can determine the transistor sizing and bias current based on the operating frequency and linearity requirements. For instance, higher bandwidth and better linearity both require higher overdrive voltage of the transistor, resulting in smaller device sizes and higher current consumption.

7.2.1.3 Linearity

The main sources of low-frequency nonlinearity of the amplifier shown in figure 7.2 are the transconductance nonlinearity of M_1, and output conductance modulation due to output voltage swing. The linearity can then be enhanced by increasing the overdrive voltage of the input transistors and increasing voltage headroom at the output node. High overdrive results in higher current consumption for the same g_m, while the headroom requirements limit transistor stacking to only a few devices.

Feedback also affects the overall linearity of the LNA. In general, a higher feedback factor (lower R_f) results in better *input* referred linearity intercept points. However, feedback could also introduce third-order tones from the second-order nonlinearity of the devices due to second-order interaction. These third-order tones could increase or decrease the overall third-order linearity of the circuit, and care should be taken when designing and simulating the amplifier.

In any case, the linearity of the LNA is usually not a dominating factor in determining the overall linearity of the system, and it is not difficult to achieve sufficient values for a given system.

7.2.1.4 High-Frequency Limitations

The analysis so far focuses on using the resistive-feedback amplifier at a "low" frequency relative to the intrinsic device speed. It is still important to be able to determine the bandwidth of the amplifier. In this section, we will estimate the bandwidth of an amplifier and separate our analysis into voltage gain bandwidth and input bandwidth.

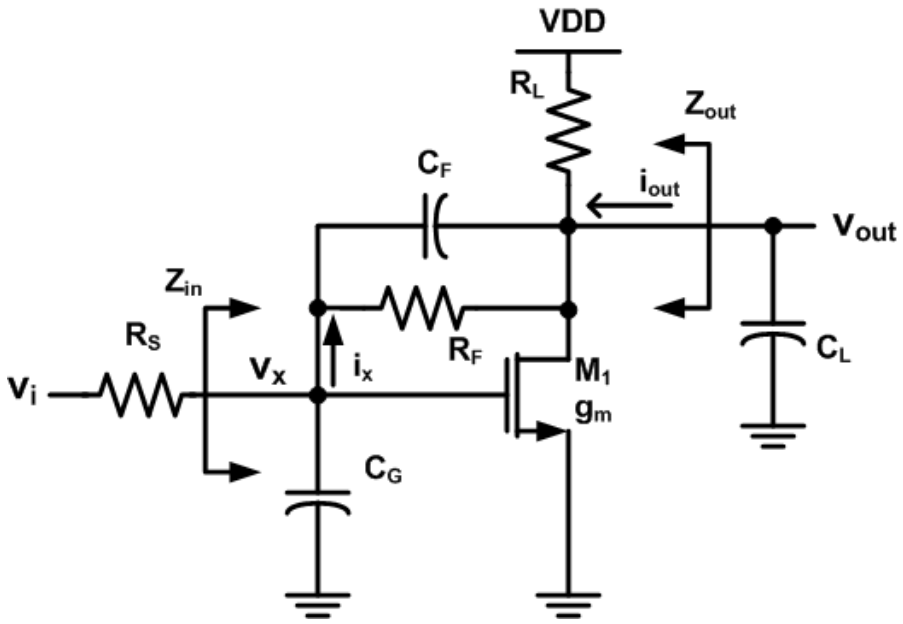

Figure 7.6 A shunt feedback amplifier with capacitors

Voltage gain from gate to drain of M_1

Figure 7.6 shows a shunt-feedback amplifier with all the capacitors. Applying KCL at the output node yields:

$$v_{out}\left(\frac{1}{R_L}+\frac{1}{R_F}+sC_L+sC_F\right)-v_x\left(\frac{1}{R_F}+sC_F-g_m\right)=0$$

$$v_{out} = v_x \frac{R_L(1 - R_F g_m)}{R_F + R_L} \frac{\left(1 + s\frac{R_F C_F}{(1 - R_F g_m)}\right)}{\left(1 + s\frac{(C_L + C_F)(R_L R_F)}{R_F + R_L}\right)} \tag{7.34}$$

If $g_m R_F >> 1$, (7.33) becomes:

$$A_V(s) = \frac{v_{out}}{v_x} = -g_m(R_L // R_F)\frac{\left(1 + s\frac{C_F}{g_m}\right)}{(1 + s(C_L + C_F)(R_F // R_L))} \tag{7.35}$$

In most cases, $C_F < C_L$ and $g_m >> 1/(R_F//R_L)$. This suggests that the voltage gain transfer function exhibits a pole at $(C_L+C_F)(R_F//R_L)$. This pole location is approximately 2-4 GHz for an amplifier with high-gain (>16 dB), low-noise (sub-3dB), and reasonable power consumption that is implemented in a 0.13 μm CMOS technology. If the same amplifier is implemented in a 45 nm CMOS technology, the achievable 3 dB bandwidth should be in excess of 10 GHz.

Input impedance seen at the gate

The input impedance seen at the gate (node V_x), together with the voltage gain transfer function discussed earlier, describes the overall transfer function for a given source impedance. In addition, it also determines the "matching" bandwidth of the amplifier. As depicted in figure 7.6, three main capacitors affect the input impedance: C_G, C_F and C_L. We will separately analyze the "effective" impedance (or admittance) that results from these capacitances in order to determine the overall impedance of the circuit.

Effects from C_G

Since C_G connects directly to the node V_x, its effective admittance seen at the node is simply its admittance, which is:

$$B_G^{eff} = j\omega C_G \qquad (s = j\omega \text{ is used}) \tag{7.36}$$

Effects from C_F and C_L

We first need to determine $i_x(s)$ when v_x is applied at the gate of M_1:

$$i_x(s) = \left(\frac{1}{R_F} + sC_F\right)\left(v_x(s) - v_{out}(s)\right) \tag{7.37}$$

Using the expression from (7.34), we get:

$$\frac{i_x}{v_x}(s) = \left(\frac{1}{R_F} + sC_F\right)\left(1 - \frac{R_L}{R_F + R_L}\frac{\left(1 - R_F g_m + sR_F C_F\right)}{\left(1 + s\dfrac{\left(C_L + C_F\right)\left(R_L R_F\right)}{R_F + R_L}\right)}\right)$$

$$\frac{i_x}{v_x}(s) = \frac{1}{R_F + R_L}\left(\frac{1}{R_F} + sC_F\right)\left(\frac{R_F\left(1 + g_m R_L\right) + sC_F R_F R_L}{\left(1 + s\left(C_L + C_F\right)\left(R_F \,//\, R_L\right)\right)}\right) \tag{7.38}$$

Replace s with $j\omega$ and we get:

$$\frac{i_x}{v_x}(j\omega) = \frac{1}{R_F + R_L}\left(1 + j\omega C_F R_F\right)\left(\frac{\left(1 + g_m R_L\right) + j\omega C_F R_L}{\left(1 + j\omega\left(C_L + C_F\right)\left(R_F \,//\, R_L\right)\right)}\right)$$

$$\frac{i_x}{v_x}(j\omega)=\frac{(1+j\omega C_F R_F)}{R_F+R_L}\left(\frac{((1+g_m R_L)+j\omega C_F R_L)\times(1-j\omega(C_L+C_F)(R_F\,//\,R_L))}{(1+\omega^2(C_L+C_F)^2(R_F\,//\,R_L)^2)}\right) \quad (7.39)$$

For simplicity, let us assume that the operating frequency is much lower than any $1/RC$ in the circuit (say, at least 3 times lower). In this case, we can ignore the second-order terms (terms with ω^2, ω^3, ω^4, etc.), while the accuracy is still acceptable. Using these conditions, (7.39) becomes:

$$\frac{i_x}{v_x}(j\omega)=\frac{1}{R_F+R_L}\frac{(1+j\omega C_F R_F)\begin{pmatrix}((1+g_m R_L)+j\omega C_F R_L)\\ \times(1-j\omega(C_L+C_F)(R_F\,//\,R_L))\end{pmatrix}}{(1+\omega^2(C_L+C_F)^2(R_F\,//\,R_L)^2)}$$

$$\frac{i_x}{v_x}(j\omega)\approx\frac{1+g_m R_L}{R_F+R_L}+j\omega\begin{pmatrix}C_F\left(\frac{R_F}{R_F+R_L}\right)\left(\frac{R_F(1+g_m R_L)}{(R_F+R_L)}+\frac{R_L}{R_F}\right)\\ -C_L\left(\frac{R_F R_L(1+g_m R_L)}{(R_F+R_L)^2}\right)\end{pmatrix}$$

$$\frac{i_x}{v_x}(j\omega)\approx\frac{1}{R_{in}}+j\omega\begin{pmatrix}C_F\left(\frac{R_F}{R_F+R_L}\right)\left(\frac{R_F}{R_{in}}+\frac{R_L}{R_F}\right)\\ -C_L\frac{(R_F\,//\,R_L)}{R_{in}}\end{pmatrix} \quad (7.40)$$

$$\frac{i_x}{v_x}(j\omega)\approx\frac{1}{R_{in}}+j\omega\begin{pmatrix}C_F\left(\frac{R_F}{R_F+R_L}\right)\left(\frac{R_F}{R_{in}}+\frac{R_L}{R_F}\right)\\ -C_L\frac{(R_F\,//\,R_L)}{R_{in}}\end{pmatrix}$$

The real part in (7.40) matches the input conductance value calculated earlier (equation (7.7)). The imaginary part depicts two equivalent susceptances that are linearly proportional to either C_F or C_L and could be viewed as effective capacitors at

the gate of M_1. In the case of C_L, V_{out} has the opposite phase of V_x at low frequency, and any imaginary-part current flowing though C_L must flow though the feedback network. As a result, the effective capacitance looking from node V_x is negative, as shown in (7.40).

From (7.36) and (7.40), an equivalent circuit of the input impedance is shown in figure 7.7. The term "low-frequency" signifies the approximation that ignores higher-order terms in (7.39).

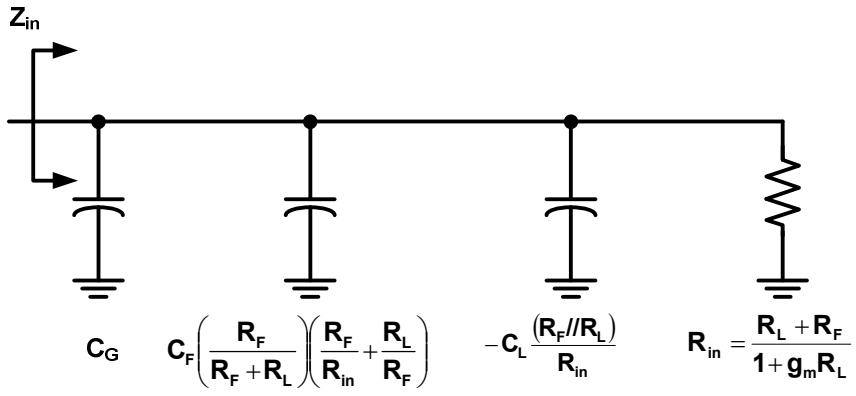

Figure 7.7 Equivalent low-frequency input impedance of the LNA

The bandwidth of the network shown in figure 7.7 in the event that $R_S = R_{in}$ is:

$$p_{in} = \frac{2}{R_{in}} \frac{1}{C_G - C_L \dfrac{R_L // R_F}{R_{in}} + C_F \dfrac{R_F}{R_F + R_L}\left(\dfrac{R_F}{R_{in}} + \dfrac{R_L}{R_F}\right)} \tag{7.41}$$

$$p_{in} = \frac{2}{R_{in} C_G - C_L\left(R_L // R_F\right) + C_F \dfrac{R_F}{R_F + R_L}\left(R_F + \dfrac{R_{in} R_L}{R_F}\right)} \tag{7.42}$$

Since $R_{in} << R_F$, the pole location at the input suggested by (7.41) should be much higher than the pole in the voltage gain transfer function. This suggests that the maximum frequency that this LNA should use is likely to be determined by the voltage gain pole. For example, if we have R_F = 447 Ω, R_{in} = 50, R_L = 100, C_G = 250 fF, C_L = 200 fF, and C_F = 100 fF, the input pole location will be at 9.5 GHz while the gate-drain voltage gain pole will locate at 3.9 GHz.

7.2.2 Multiple Gated Linearity Enhancement Techniques

One technique that can be used for building block linearization is by using multiple gated transistors [7.4]. In general, the drain current of a common source MOS transistor (assuming a memory-less non-linearity) is expressed as:

$$I_{DS} = I_{DC} + g_m v_{gs} + \frac{g_m^{'}}{2!} v_{gs}^2 + \frac{g_m^{''}}{3!} v_{gs}^3 + \ldots \tag{7.43}$$

where $g_m^{'}$ and $g_m^{''}$ are, respectively, the first and the second derivatives with respect to gate-to-source voltage. Figure 7.8(a) shows a typical measured current and its derivative (g_m, $g_m^{'}$ and $g_m^{''}$) characteristics of an NMOS. The figure shows that the $g_m^{''}$ goes to the positive peak value in the subthreshold region, then crosses zero and shows a negative peak value at the gate voltage higher than V_{th}. To reduce the DC power consumption without losing the RF gain, the gate bias voltage of the RF amplifier is usually biased at overdrive (V_{gs}-V_{th}) in the range between 0.1 and 0.4 V. Unfortunately, the $g_m^{''}$ in this bias region has a negative peak value (as shown in figure 7.8(a)), which significantly degrades the linearity of an amplifier.

In figure 7.8(b), M_1 is biased at V_{gs}, and M_2 is biased at V_{gs}-V_{shift}, so the transfer characteristic curve for M_2 is shifted to the right by the amount of V_{shift}. Once the bias points for M_1 and M_2 are determined, the amount of compensation for the value of g_m'' can be chosen by adjusting the width of M_2, resulting in a Multi-Gate Transistor (MGTR) amplifier, as shown in figure 7.8(c) [7.4][7.5].

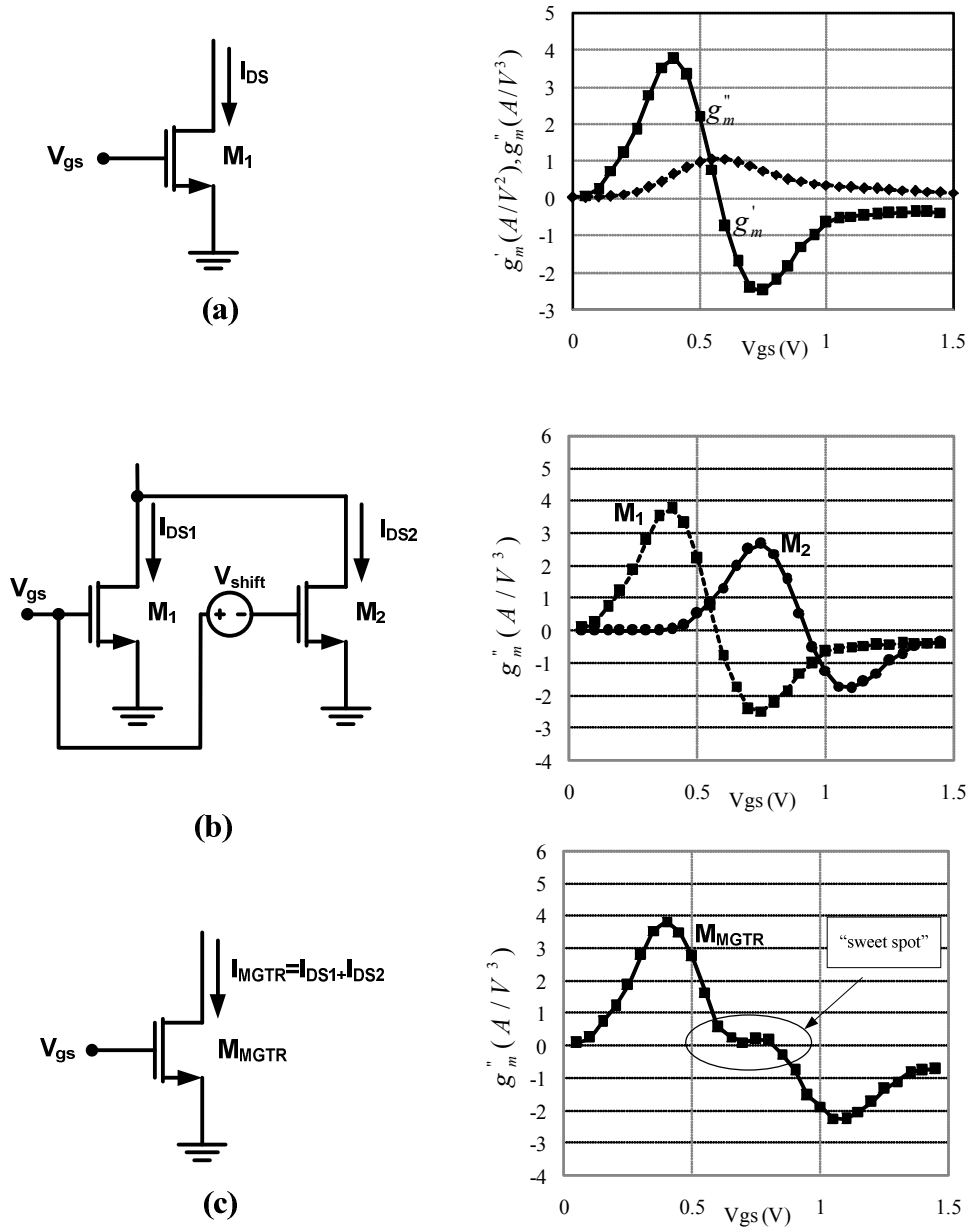

Figure 7.8 Multi-gate transistor concept

Because the positive and negative characteristics of g_m'' are not symmetrical, the compensated flat region for the gate bias is quite narrow (about 0.2 V) with only one auxiliary transistor (M_2 in this case). This flat region can be extended farther by adding multiple gated transistors with proper bias voltage and size. However, adding too many transistors can lead to worse characteristics due to other effects, such as parasitic capacitance, and can increase loss in the auxiliary transistors [7.5]. Please note that because M_2 is biased in the subthreshold regime, this linearization method does not consume significant extra power, and could be added to any transconductance stage with minimal penalties in area or power.

7.3 Circuit Implementations

In this section we will discuss detailed implementations of the front-end, covering all the major building blocks.

7.3.1 Low noise amplifier (LNA)

Figure 7.9 shows the implemented LNA. The LNA core uses a complementary gain stage in order to increase the overall current efficiency. The bias current of the LNA core is set by the PMOS device bias voltage (V_{biasP}), and the NMOS device is self-biased through the feedback resistor R_f. Using this biasing scheme results in a controllable bias current and voltage headroom without a need for common-mode feedback circuitry, which is beneficial for process trimming purposes and costs. The LNA has a low-gain mode that is activated by turning on the NMOS transistors (setting V_{gain} to high). The LNA bias current is 8 mA, and the total transconductance of the stage

is ~90 mS. Total voltage gain of the LNA core in the high and low gain modes is simulated to be 18 dB and 0 dB respectively.

Since the resistive-feedback LNA suffers from low reverse-isolation due to the direct output-to-input path via R_f, and a buffer stage is added to increase the reverse isolation of the receive chain. This buffer also helps isolate the large capacitive loads at the input of the mixer stage from the LNA output nodes. The buffer consumes 2 mA of total current.

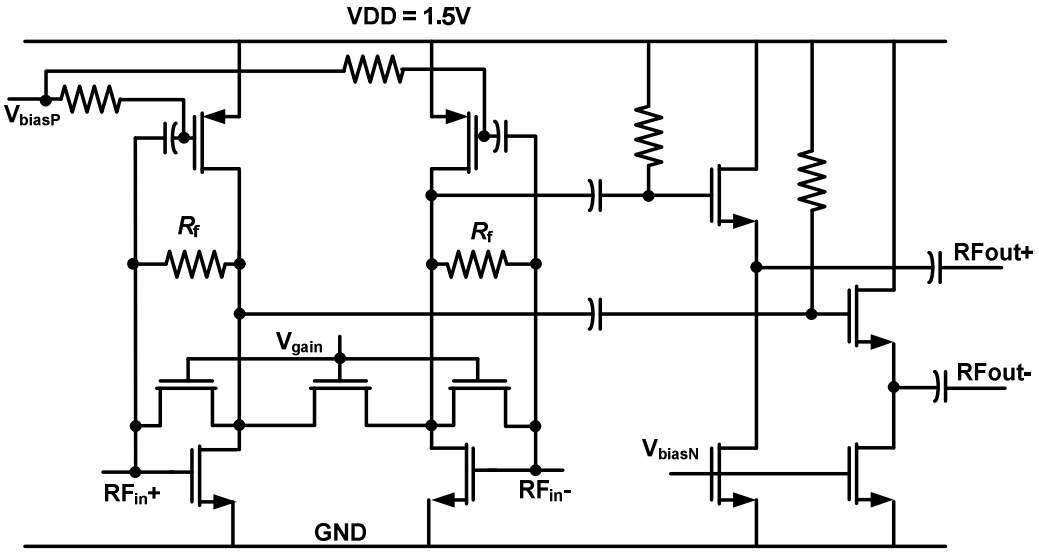

Figure 7.9 A low-noise amplifier with bias connections

7.3.2 Mixer core and low-pass filters

The mixer consists of a transconductance (g_m) stage, a switching quad, and an RC feedback transimpedance amplifier at the output, which is similar to the topology presented in [7.6] and described in chapter 6. The mixer g_m stage is shown in figure 7.10 and is again a complementary pair, with both NMOS and PMOS input devices.

A complementary input increases the current efficiency of the circuit and reduces the overall IM_2 contribution of the stage due to the IM_2 cancellation mechanism, as discussed in [7.7]. Both PMOS and NMOS input stages are balanced inputs with no current source, in order to reduce voltage headroom requirements and allow the use of multi-gated input pairs for IM_3 cancellation.

The use of multi-gated input pairs allows tuning to find the optimal operating points that result in higher performance of the circuit with almost the same bias current. Although no automatic tuning or compensation is implemented in this design, the tuning capability is added to enable on-board tuning and to enable use of the front-end for future research in tuning algorithms.

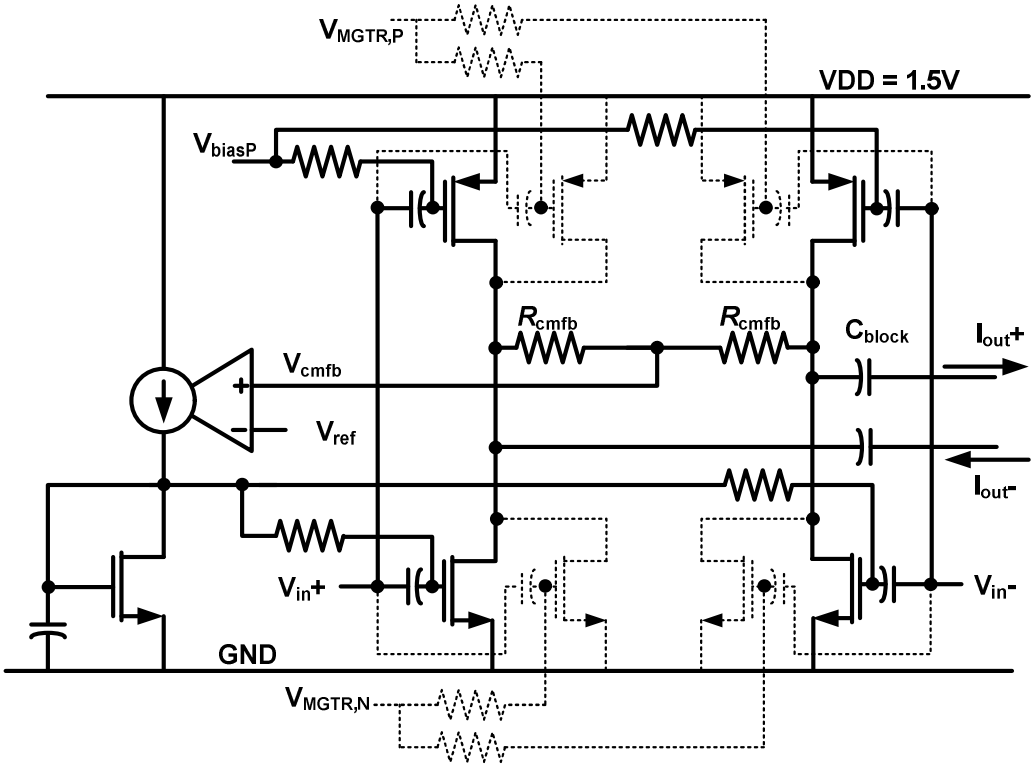

Figure 7.10 Transconductance stage of the mixer

An AC coupling capacitor is used at the output in order to block low-frequency IM_2 tones from entering the later stages. The switching quad is a basic passive mixer driven by CMOS buffers at the LO port, and the output of the switching quad connects to a transimpedance amplifier with an RC feedback network. Effectively, this structure is a 1^{st}-order low-pass current-to-voltage conversion network [7.6]. The bandwidth of the filter can be digitally tuned by controlling the values of the feedback and input capacitors. The switches are implemented by CMOS transistors. The tuning of the input capacitor is needed in order to keep the feedback factor of the circuit relatively constant and to provide a wider stable tuning range. In this particular implementation, the capacitor value can be tuned to provide a baseband 3-dB bandwidth from 1 MHz to 5MHz.

7.3.3 Operational amplifier for the transimpedance stage.

Figure 7.11 shows an operational amplifier for the transimpedance amplifier that was implemented as a two-stage amplifier. A push-pull output stage was chosen to provide higher driving capability and output range, given the same bias current. A common-mode feedback loop was used to ensure that the quiescent bias current flowing through the output stage is well-defined.

7.3.4 Frequency Divider

The frequency divider architecture is the same as that shown in figure 6.6 in the previous chapter. The input at $2f_{LO}$ frequency goes through a pair of buffers before

entering the main CML divider core. The output is then buffered to drive the switching quad.

An auxiliary circuit for quadrature phase correction is added to the frequency divider, and its block diagram is shown in figure 7.12. It consists of a multiplier, an integrator, an amplifier, and delay correction circuitry. A similar phase correction circuit was reported in [7.8].

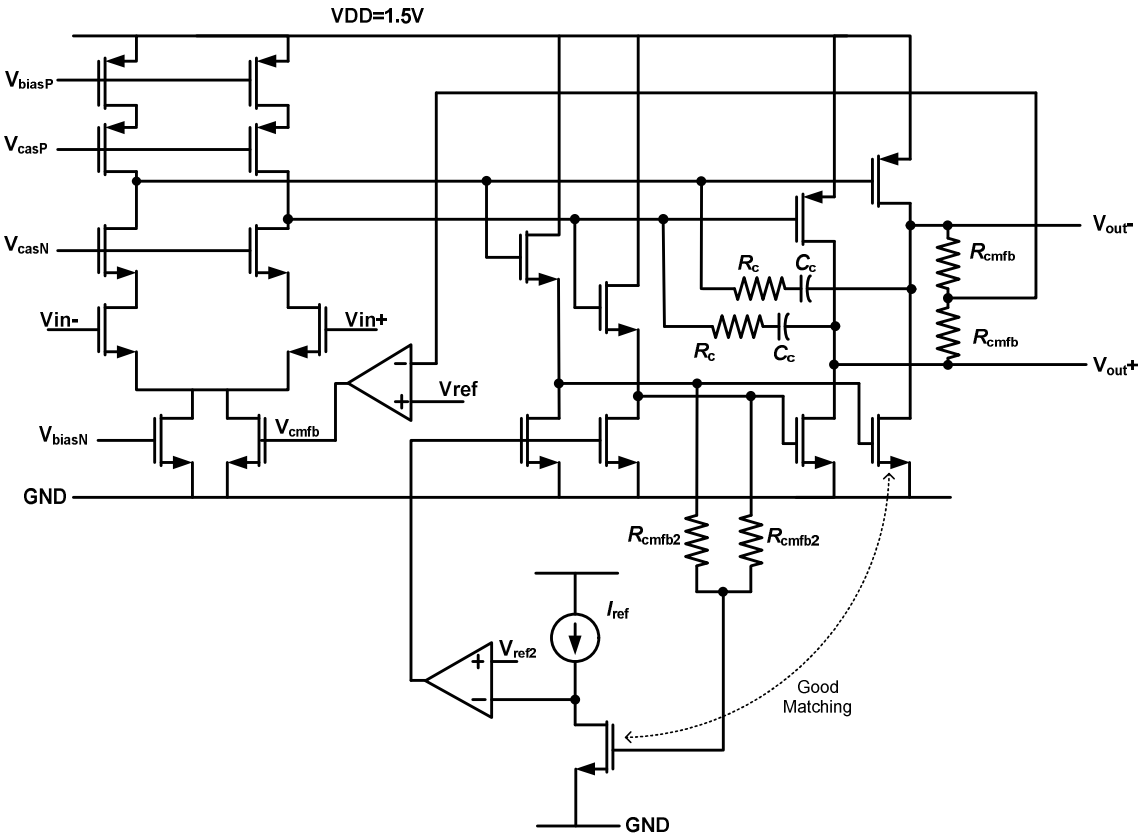

Figure 7.11 Opamp for the transconductance stage

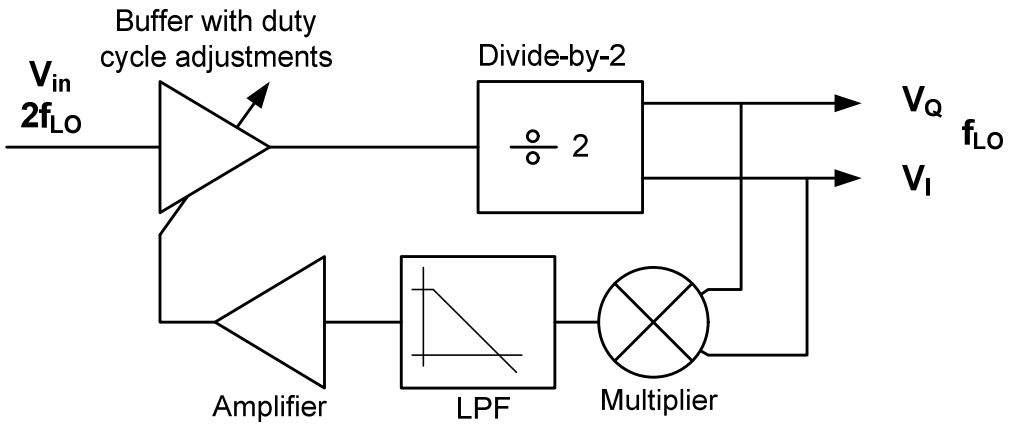

Figure 7.12 Frequency divider phase correction circuitry block diagram.

The circuit takes in the in-phase (I) and quadrature-phase (Q) outputs from the divider and multiplies the two signals together. These two signals could be written as:

$$V_I(t) = a_0 + a_1\cos(\omega_o t) + a_2\cos(2\omega_o t) + a_3\cos(3\omega_o t) + a_4\cos(4\omega_o t) + ... \quad (7.44)$$

$$\begin{aligned} V_Q(t) = {} & a_0 + a_1\cos(\omega_o(t+\Delta t)) + a_2\cos(2\omega_o(t+\Delta t)) \\ & + a_3\cos(3\omega_o(t+\Delta t)) + a_4\cos(4\omega_o(t+\Delta t)) + ... \end{aligned} \quad (7.45)$$

If differential signaling is used and a high degree of symmetry and matching is achieved, all the even-order terms in (7.44) and (7.45) will be negligible and the expressions become:

$$V_I(t) = a_1\cos(\omega_o t) + a_3\cos(3\omega_o t) + a_5\cos(5\omega_o t) + ... \quad (7.46)$$

$$V_Q(t) = a_1\cos(\omega_o(t+\Delta t)) + a_3\cos(3\omega_o(t+\Delta t)) + a_5\cos(5\omega_o(t+\Delta t)) + ... \quad (7.47)$$

Multiplication of (7.46) and (7.47) gives:

$$\begin{aligned} V_Q(t)V_I(t) = a_1^2\cos(\omega_o t)\cos(\omega_o(t+\Delta t)) + a_1 a_3\cos(\omega_o t)\cos(3\omega_o(t+\Delta t)) \\ + a_1 a_3\cos(3\omega_o t)\cos(\omega_o(t+\Delta t)) + a_3^2\cos(3\omega_o t)\cos(3\omega_o(t+\Delta t)) + .. \end{aligned} \quad (7.48)$$

Assuming that all the sinusoidal terms will be filtered out later by an integrator or a low-pass filter, we can then focus on the DC components of (7.48). These DC components can be expressed as:

$$V_Q(t)V_I(t)\big|_{DC} = \frac{1}{2}a_1^2\cos(\omega_o\Delta t) + \frac{1}{2}a_3^2\cos(3\omega_o\Delta t) + \frac{1}{2}a_5^2\cos(5\omega_o\Delta t) + ... \quad (7.49)$$

In an ideal case, the quadrature-phase signal (V_Q) is shifted from the in-phase signal (V_I) by 90° for the fundamental tone (ω_o tone), hence we have:

$$\omega_o\Delta t_{ideal} = \frac{\pi}{2}$$

$$\Delta t_{ideal} = \frac{\pi}{2\omega_o} \quad (7.50)$$

If we define δ as the deviation of Δt from the ideal value, the expression of Δt can be expressed as:

$$\Delta t = \Delta t_{ideal} + \delta = \frac{\pi}{2\omega_o} + \delta \tag{7.51}$$

Using (7.49) and (7.51), we then get:

$$V_Q(t)V_I(t)\big|_{DC} = -\frac{1}{2}a_1^2 \sin(\omega_o\delta) + \frac{1}{2}a_3^2 \sin(3\omega_o\delta) - \frac{1}{2}a_5^2 \sin(5\omega_o\delta) + \ldots \tag{7.52}$$

If $\omega_o\delta$ is small (for example, less than 10°), (7.52) could be estimated as in (7.53). Note that higher-order terms ($7\omega_o\delta$ or higher) might be grossly overestimated but can be neglected in certain cases depending on the values of a_n. (for example, in the case of a square wave where a_7 is 1/7):

$$V_Q(t)V_I(t)\big|_{DC} \approx -\frac{1}{2}a_1^2(\omega_o\delta) + \frac{3}{2}a_3^2(\omega_o\delta) - \frac{5}{2}a_5^2(\omega_o\delta) + \ldots \tag{7.53}$$

If $V_Q(t)$ *and* $V_I(t)$ are square waves, which is a good approximation in most cases, we then get:

$$\begin{aligned} V_Q(t)V_I(t)\big|_{DC,Square} &\approx -\frac{1}{2}(\omega_o\delta) + \frac{1}{6}(\omega_o\delta) - \frac{1}{10}(\omega_o\delta) + \frac{1}{14}(\omega_o\delta) - \ldots \\ &= -K_1(\omega_o\delta) \end{aligned} \tag{7.54}$$

where K_1 is a *finite positive* coefficient. This means that the DC portion of the multiplier output voltage is proportional to δ with negative coefficient.

The delay correction circuitry could be implemented in different ways as long as it can adjust the zero-crossing points of the divider input signal. In this particular implementation, the delay is corrected by adjusting the rise and fall time of the inverters used in a buffering stage before the divider. The simplified schematic of the adjustment mechanism is shown in figure 7.13 below.

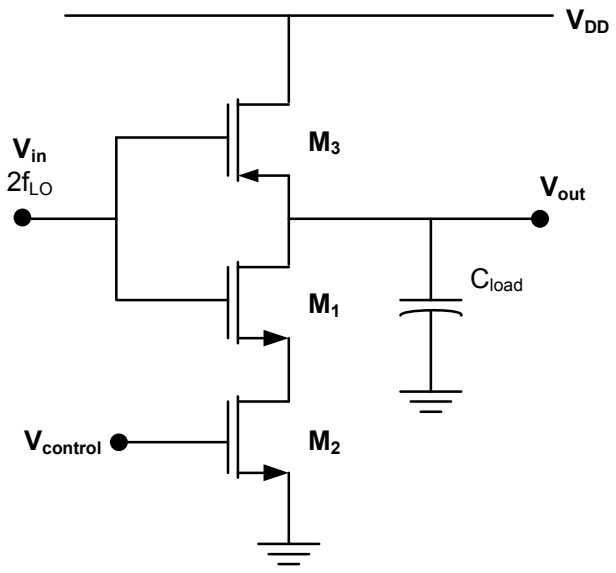

Figure 7.13 An inverter with a delay adjustment circuitry.

In figure 7.13, the pull-down resistance is a series combination of the on-resistance of M_1 and the on-resistance of M_2. During the pull-down, the gate of M_1 is tied to V_{DD} while the gate of M_2 is tied to a control voltage $V_{control}$. Assuming a square law, the on-resistance of a MOS transistor in triode mode is given by:

$$R_{ON} = \frac{1}{k' \frac{W}{L}\left(V_{Control} - V_{th}\right)} \tag{7.55}$$

where k' is a constant that depends on the process technology. W and L are the width and length of the transistor. If the control voltage consists of a "static" part (V_C) and dynamic part (v_c), the pull-down resistance could be:

$$R_{ON} = \frac{1}{k' \frac{W}{L}\left(V_D - V_{th} - v_c\right)} \tag{7.56}$$

$$R_{ON} = \frac{1}{k' \frac{W}{L}\left(V_{OD} - v_c\right)} \tag{7.57}$$

where V_{OD} is the overdrive voltage of the transistor. The total on-resistance of the combined pull-down path will be:

$$R_{pull} = R_1 + \frac{1}{k' \frac{W}{L}\left(V_{OD} - v_c\right)} \tag{7.58}$$

Since the time delay in pull-up and pull-down is linearly proportional to the capacitance and resistance of the pull-down path, we can then write:

$$T_{down} = K_{pull}\left(R_1 + \frac{1}{k' \frac{W}{L}\left(V_{OD} - v_c\right)}\right) \tag{7.59}$$

where K_{pull} depends on the output capacitance of the stage and the characteristics of the input signals. If we define Δt_{down} as the deviation of pull-down time from the case when v_c=0, we then get:

$$\Delta t_{down} = K_{pull}\left(R_1 + \frac{1}{k'\frac{W}{L}(V_{OD} - v_c)}\right) - K_{pull}\left(R_1 + \frac{1}{k'\frac{W}{L}V_{OD}}\right) \tag{7.60}$$

$$\Delta t_{down} \approx K_{pull}\left(R_1 + \frac{1}{k'\frac{W}{L}V_{OD}}\left(1 + \frac{v_c}{V_{OD}}\right)\right) - K_{pull}\left(R_1 + \frac{1}{k'\frac{W}{L}V_{OD}}\right)$$

$$\Delta t_{down} \approx K_{pull}\frac{v_c}{k'\frac{W}{L}V_{OD}^2} = K_{delay}v_c \tag{7.61}$$

Using (7.54) and (7.61), we can draw a simplified mathematical model of the phase correction loop, as shown in figure 7.14.

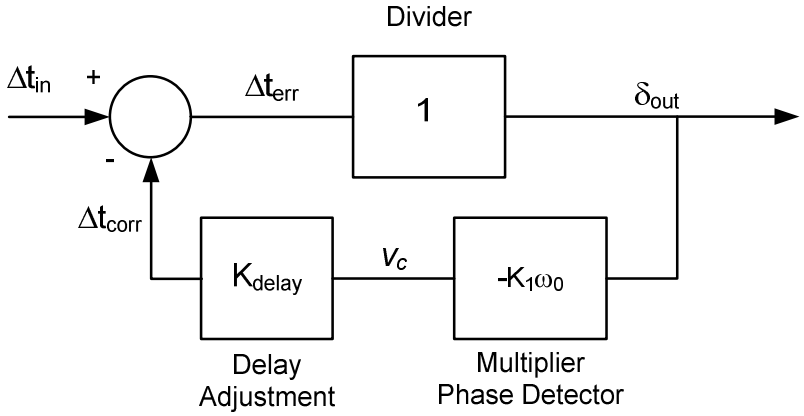

Figure 7.14 A simplified model of the IQ phase correction loop

Although this diagram ignores the frequency response that controls the dynamics of the loop, it captures the main part of the loop that regulates the phase error. The closed-loop DC transfer function, from the phase error at the input to the phase error at the output, is given by:

$$\frac{\delta_{out}}{\Delta t_{in}} = \frac{1}{1 + K_{delay} K_1 \omega_o} \tag{7.62}$$

From (7.62), it is clear that a lower phase error could be achieved by increasing loopgain. Since this is a feedback system, loop stability could be an issue and should be considered in the design. In this work, the frequency response is compensated by placing a dominant RC pole at the output of the IQ multiplier. In addition, the accuracy of the compensation is affected by mismatches and compensation of devices in the system, especially the comparison devices (the IQ multiplier and the first amplifier afterwards). In the final implementation, this phase correction could be turned off entirely using a digital bit.

7.4 Experimental Results

The circuit was fabricated in a 0.13 μm CMOS technology provided by Infineon Technologies, and the die microphotograph is shown in figure 7.15. The chip size including all pads is 1.5 mm x 1.5 mm. Active areas for the LNA, mixer core, and dividers are approximately 0.1 mm^2 in total, and the transimpedance amplifiers occupy 0.6 mm^2.

Measurements were done on a PCB with encapsulated chip-on-board. The board has differential RF inputs and differential $2f_{LO}$ inputs. Off-board baluns were used to provide differential drives. At the output of the receiver, a differential-to-single-ended buffer was added to isolate the loading effects seen in the mixer output stage. These buffers were implemented using ADA4899-1 chips from analog devices [7.9]. The test boards were built with FR4 material. Figure 7.16 shows a complete photograph of the assembled test board.

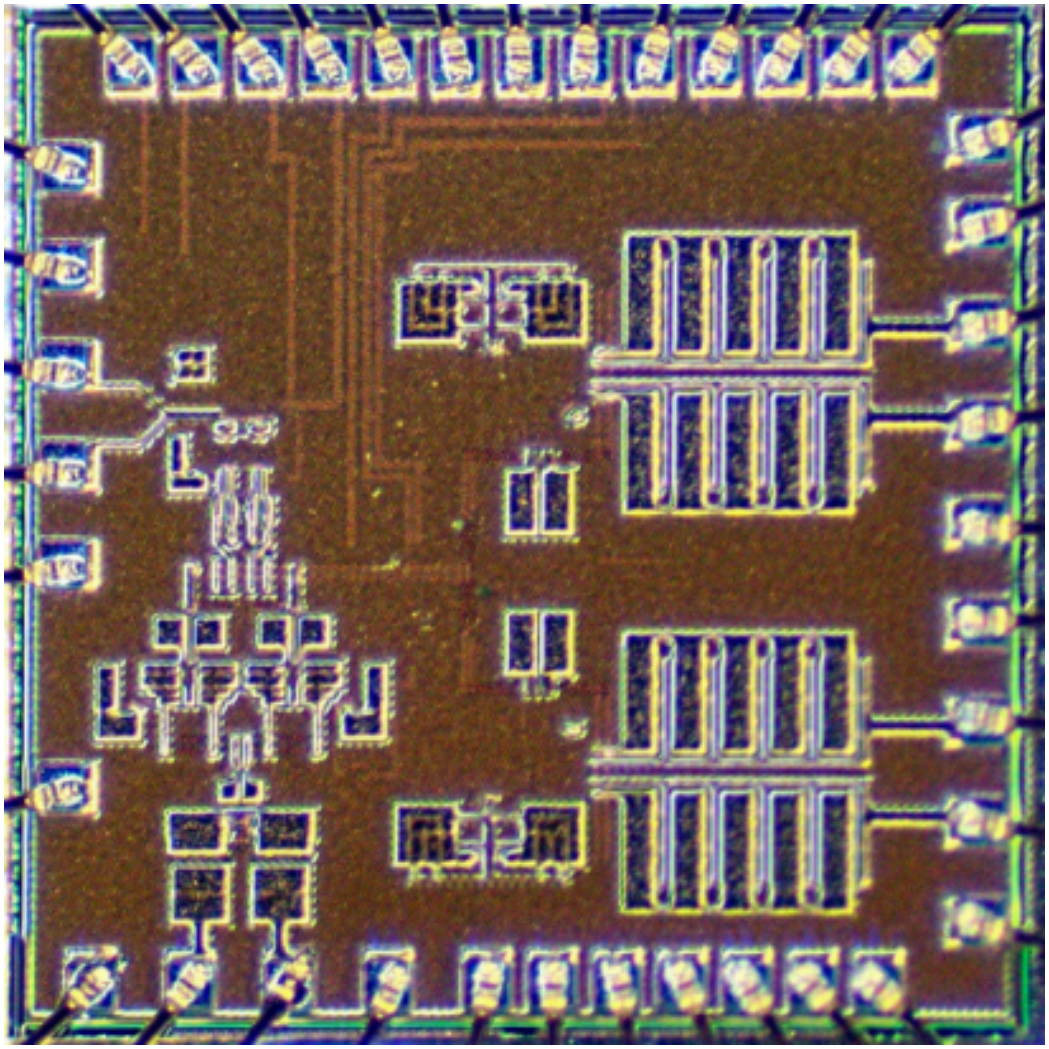

Figure 7.15 Die microphotograph

The chip consumes 32 mA at 0.5 GHz f_{LO} and 35 mA at 2.5 GHz f_{LO} from a 1.5 V voltage supply including all the currents drawn from bias circuitry. The $2f_{LO}$ signal needs to be -5 dBm at 1 GHz and 10 dBm at 5 GHz in order to maintain front-end functionality. These power levels are measured at the SMA connector inputs. The divider works up to 5.2 GHz (2.6 GHz output).

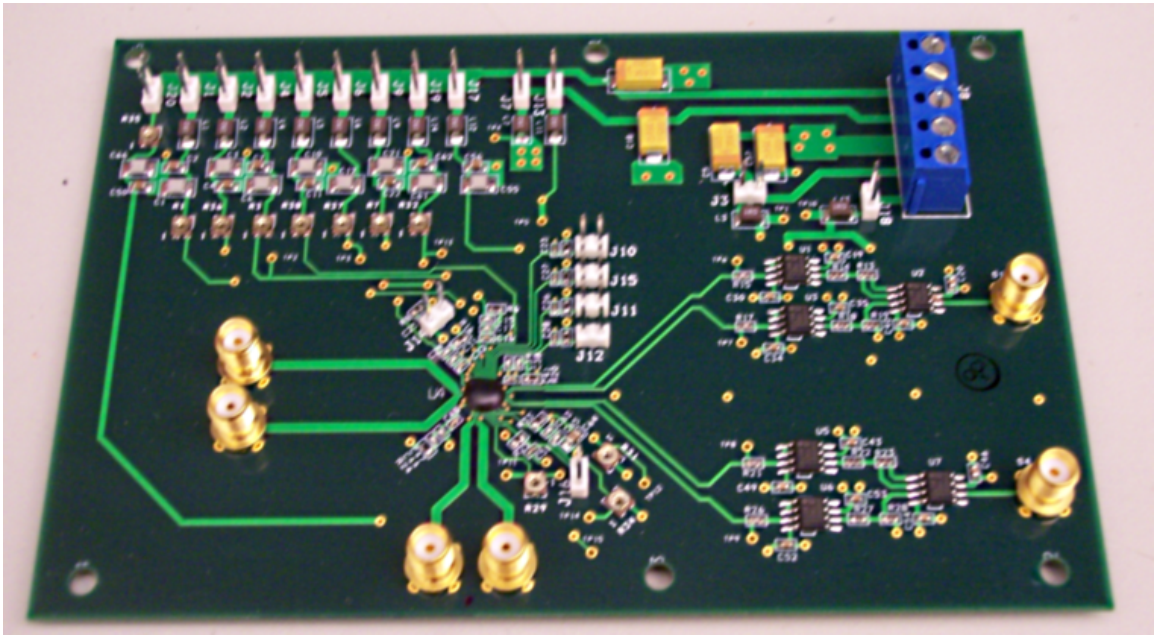

Figure 7.16 Assembled test board

Figure 7.17 shows plots of the input S_{11} referring to a 100 Ω differential source impedance. The S_{11} measurements were done in both high-gain and low-gain modes. For the high-gain mode, S_{11} matches better than -10 dB from 0.5 GHz to 3.8 GHz. In the low-gain mode, S_{11} matches better than -7 dB up to 3.6 GHz. The S_{11} results include parasitics due to the connector and test boards. The results suggest that the designed front-end would not need any off-chip matching components except a balun or a band-pass filter that are required for the intended application.

Figure 7.18 shows conversion gain (in high-gain mode) at a function of LO frequency for baseband frequencies of 1 MHz with a 3 dB bandwidth setting of 2 MHz. The results include variations due to impedance mismatches at the LNA inputs. The voltage gain of the front-end is approximately 3 dB lower than the power gain.

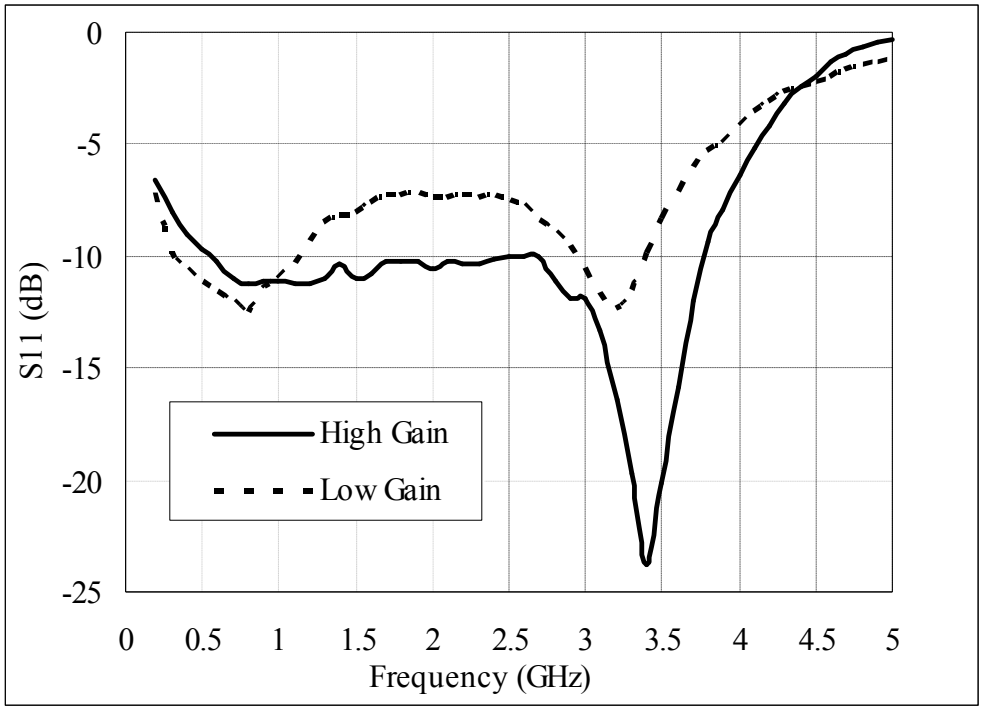

Figure 7.17 S_{11} of the receiver in both gain modes

Figure 7.19 shows conversion gain plots against baseband frequency at different bandwidth settings. The LO frequency in this measurement is fixed at 1.5 GHz, and the baseband 3-dB bandwidth can be tuned from 1 MHz to 5 MHz. In addition, harmonic mixing was measured with 2 GHz RF input signal while varying the LO frequency to have harmonics located at 2 GHz. The conversion gains of $3f_{LO}$, $5f_{LO}$, and $7f_{LO}$ are 9.5 dB, 14 dB, and 17 dB below the conversion gain at f_{LO}, respectively.

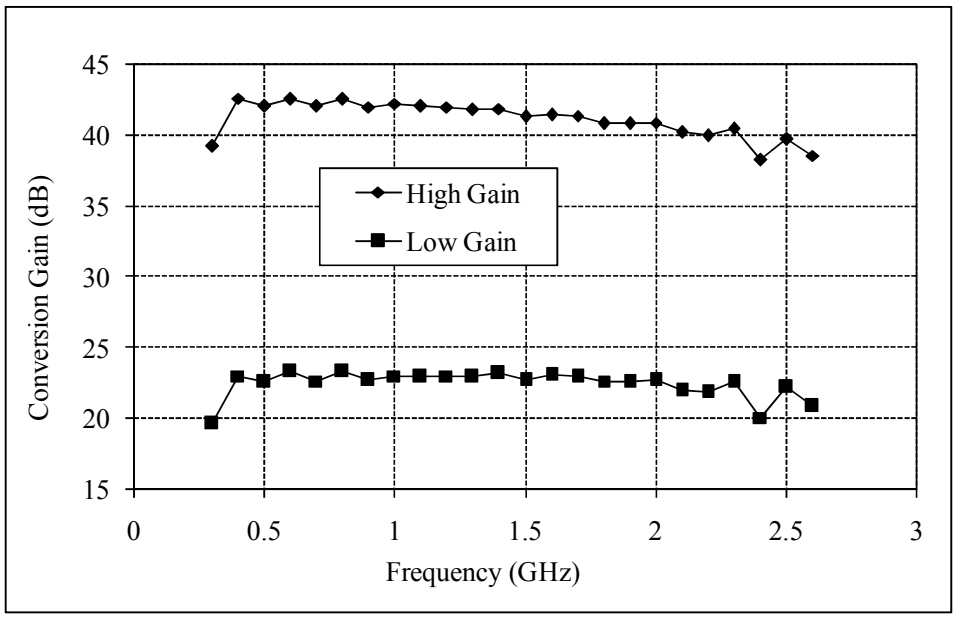

Figure 7.18 Conversion gain across LO frequencies.

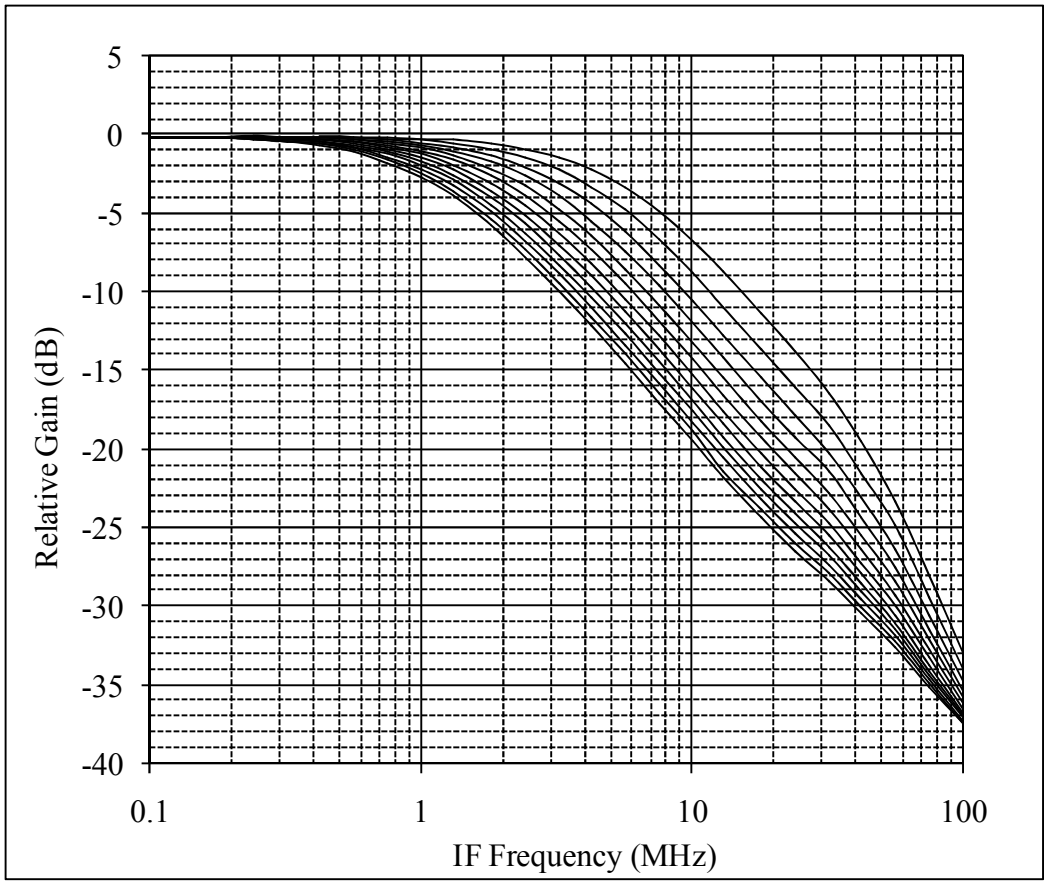

Figure 7.19 IF frequency response across various bandwidth settings

The in-band two-tone third-order input intercept point (IIP_3) was done with input tones at 330 kHz and 230 kHz offsets from f_{LO} of 1.5 GHz. The normal IIP_3 is -6.5 dBm while the tuned IIP_3 is +4 dBm as shown in figure 7.20. The out-of-band IIP_3 was measured with input tones at 4 MHz and 8.2 MHz, and the normal value is -7 dBm. In low-gain mode, the normal IIP_3 is +4 dBm for both in-band and out-of-band tones.

The measured in-band IIP_2 with the tones at 330 kHz and 230 kHz offsets is +48 dBm, while the out-of-band IIP_2 with the tones at 4 MHz and 4.2 MHz offsets is +60 dBm. IIP_2 in low-gain mode is higher than +80 dBm. The measurements become increasingly difficult as IIP_2 increases, due to limitations in the dynamic range of the test equipment. Also, it is possible that the measured in-band IIP_2 is limited by the on-board buffers or the spectrum analyzer.

Noise was measured at various LO and RF frequencies using a noise figure meter. At 1.5 GHz f_{LO} and 1 MHz baseband, the measured double-sideband noise figure (DSB NF) is 5.8 dB including all the balun, cable, board losses, and input mismatches. The estimated loss of the balun and cable (obtained from separate cable and balun measurements using a network analyzer) is 2.2 dB, and the de-embedded DSB NF is 5.8 dB – 2.2 dB = 3.6 dB. The 3.6 dB DSB NF still includes any board and SMA connector losses, since it is not possible to directly measure the loss on the PCB. Plots of de-embedded NF versus baseband for various RF bands are shown in figure 7.21. DSB NF is approximately 18 dB at 1.5 GHz RF and 1 MHz baseband offset in the low-gain mode.

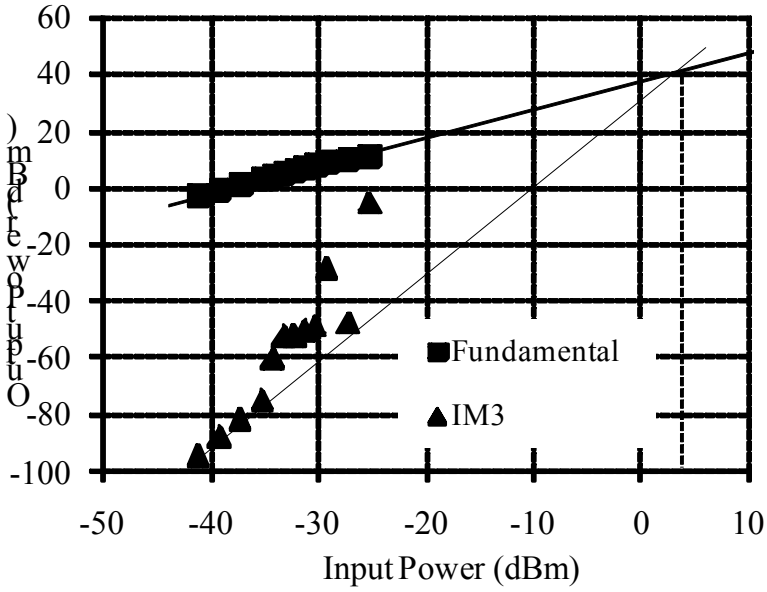

Figure 7.20 IM3 plot for IIP3 calculations of the circuit

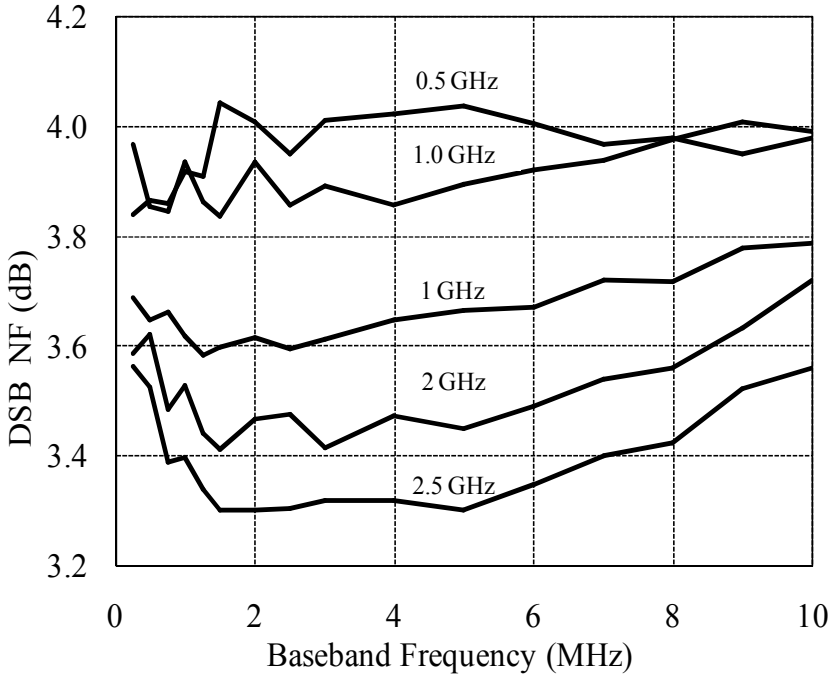

Figure 7.21 De-embedded DSB-NF at various frequencies

Figure 7.22 shows the plot of measured LO leakage at the RF port in high-gain mode, which is below -100 dBm for an entire operating frequency range. During the measurements, the LO leakage does not change with gain mode, implying that it is not dominated by the signal path isolation but rather by other mechanisms such as supply and ground coupling.

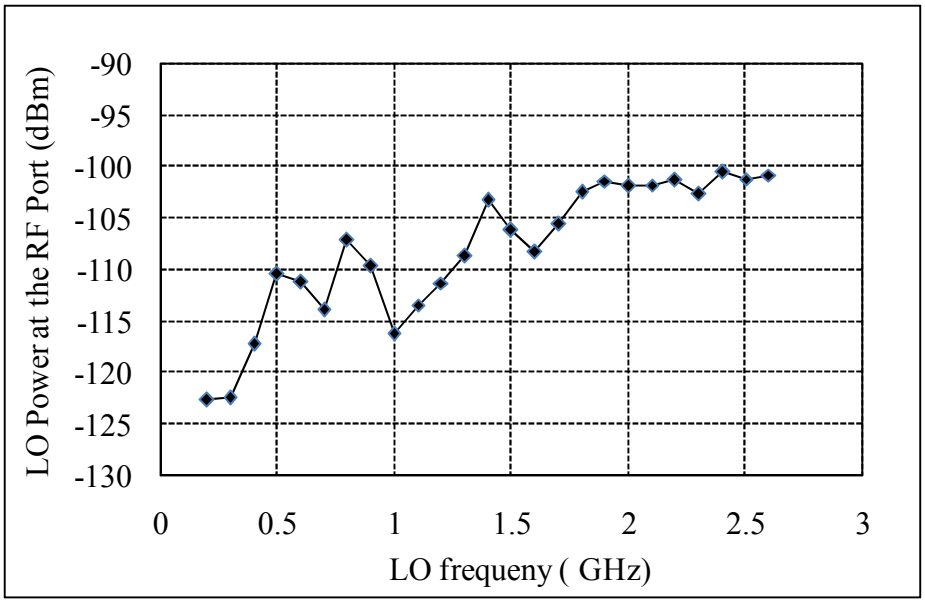

Figure 7.22 Measured LO-RF leakage at various frequencies.

7.5 References

[7.1] J.-H.C. Zhan and S.S. Taylor, "A 5GHz Resistive-Feedback CMOS LNA for Low-Cost Multi-Standard Applications," *ISSCC Dig. Tech. Papers*, pp. 200-201, Feb. 2006.

[7.2] S.C. Blaakmeer et al., "An Inductorless Wideband Balun-LNA in 65nm CMOS with balanced output, *Proc. ESSCIRC*, pp. 364-367, Sept., 2007.

[7.3] P. R. Gray, R.G. Meyer, P. J. Hurst, and S. H. Lewis. *Analysis and Design of Analog Integrated Circuits,* Fourth Edition, Wiley, New York, 2001.

[7.4] B. Kim, J.-S. Ko, and K. Lee, "A New Linearization Technique for MOSFET RF Amplifier Using Multiple Gated Transistors," *IEEE Microw. Guided Wave Lett.*, vol. 10, no. 9, pp. 371–373, Sep. 2000.

[7.5] T. Kim, B. Kim, and K. Lee, "Highly Linear Receiver Front-End Adopting MOSFET Transconductance Linearization by Multiple Gated Transistors," *IEEE J. Solid-State Circuits*, vol. 39, Jan. 2004, pp. 223-229.

[7.6] N. Poobuapheun, W-H. Chen, Z. Boos, A. M. Niknejad, "A 1.5 V 0.7-2.5GHz CMOS Quadrature Demodulator for Multi-Band Direct-Conversion Receivers," *IEEE J. Solid-State Circuits*, vol. 42, Aug. 2007, pp. 1669-1677.

[7.7] Ilku Nam, et al., "CMOS RF Amplifier and Mixer Circuits Utilizing Complementary Characteristics of Parallel Combined NMOS and PMOS Devices," *IEEE Transactions on Microwave Theory and Techniques*, vol. 53, Issue 5, pp. 1662-1671, May 2005.

[7.8] S. Navid, F. Behbahani, A. Hajimiri, R. Gaethke, and M. Delurio, "Level-Locked Loop, A Technique for Broadband Quadrature Signal Generation," in *Proc. IEEE Custom Integrated Circuits Conf.*, pp. 411-414, May 1997.

[7.9] http://www.analog.com/en/prod/0,,759_786_ADA4899%252D1,00.html

8

Conclusion

8.1 Introduction

This research focused on issues surrounding the design of a multi-band, multi-standard receiver, specifically, a wideband LNA and mixer designs that cover all frequency bands from 0.7–2.5 GHz. This chapter summarizes the work presented in this dissertation and concludes with a discussion of future research topics.

8.2 Summary and Contributions

In Chapter 2 we reviewed receiver fundamentals, starting with the concepts of selectivity and sensitivity, followed by a review of basic receiver architectures, including homodyne and heterodyne. We also compared several receiver architectures for multi-band receivers that use broadband front-ends. A promising way to implement such a receiver is with multiple broadband receiver front-ends, each of which covers a group of frequencies in an allocated sub-band. This yields a good compromise without using multiple narrow-band front-ends, which would occupy a large area; or using a broadband front-end, which would be susceptible to high levels of out-of-band interference. We also discussed requirements and estimated performance.

Chapter 3 reviewed noise sources, basic LNA architectures, and advanced architectures for multi-band operations. Chapter 4 presented the design of the broadband CMOS LNA, which was fabricated and measured in an IBM 0.18 μm technology process. The LNA achieves -3 dB bandwidth from 1–2 GHz with 16 mA bias current and 17 dB peak voltage gain. The noise figure is below 4 dB for the same input frequency range and bias current, with a minimum value of 2.7 dB around 1.2 GHz. The LNA has -10 dB or better input matching for the entire bandwidth range, even if the bias current varies from 2–16 mA. As a result, it is suitable for dynamic broadband operation in multi-band, multi-mode receivers.

We found some discrepancies between simulations and measurement results of the LNA. A major problem is the accuracy of noise modeling. Because the gate noise is not accurately modeled in the modeled transistor, its noise contribution could be considerably underestimated. In addition, the frequency response mismatches might result from unexpected parasitics causing narrow LNA bandwidth, as observed in the measurements. These problems can be solved by careful layout, modeling, and parasitic calculations.

In Chapter 5 we discussed basic concepts of the mixer, important mixer specifications, mixer implementations in CMOS technologies, and quadrature signal generation. The best way to implement a mixer is by using switches, which can be implemented easily using MOS transistors. Compared to its single-balanced counterpart, a double-balanced mixer (either passive or active) performs better in key areas such as port isolation and IM_2. However, a single-balance mixer is simpler, consumes less current, and should be used when the specifications can be met. In addition, because of

the high level of *1/f* noise in CMOS devices, a passive mixer has strong advantages for use in direct-conversion receivers.

Quadrature signal generation is essential in any receivers that use quadrature demodulation. There are several ways to obtain quadrature signals, including divide-by-two circuits, a quadrature-coupled oscillator, and polyphone filters. The choice is driven primarily by the process technology (device speed and process variations), operating frequency/frequencies, and power consumption requirements.

Chapter 6 presented an analysis and design of a low 1/*f* noise inductorless quadrature demodulator. We used a fully differential complementary pair to increase the efficiency of the transconductance. The circuit operates over a wide range of frequencies, including the 0.7–2.5 GHz frequency bands. Mixer gain can be reduced and linearity can be increased by reducing the feedback impedance of the transimpedance stage at the mixer output, at the cost of increasing the noise figure in the system. The feedback resistors and capacitors can be made programmable by using MOS switches, which also increases design flexibility.

Chapter 7 covered the design and analysis of a wideband receiver front-end in 0.13 μm CMOS technology. The front-end employs a wideband resistive feedback LNA with gain adjustments. A source-follower stage was inserted between the LNA and the mixer to increase electrical reverse isolation and reduce LO leakage from the mixer to the LNA input. The mixer architecture is similar to the one presented in Chapter 6, but uses multi-gated transistors at the mixer transconductance stage. The multi-gated topology permits tuning to increase front-end linearity without bias current penalties. The front-end operates from 0.3–2.6 GHz with a 1–5 MHz baseband bandwidth. The

chip employs no inductors and achieves a conversion voltage gain of 38 dB with a 3.6 dB DSB noise figure. The default IIP_3 of -6.5 dBm can be increased to +4 dBm in high-gain mode when the circuit is properly tuned. In addition, the circuit achieves +48 dBm IIP_2 in high-gain mode. The chip consumes 32–35 mA from a 1.5 V supply.

An important consideration when implementing an integrated front-end using the architecture presented in Chapters 6 and 7 is that in most receivers, the LO is generated with an integrated voltage-controlled oscillator (VCO), which must be designed properly to minimize LO leakage into other parts of the circuits; this could cause dynamic DC offsets. This issue can be alleviated by choosing a VCO running frequency that is not an integer multiple of f_{LO}, as shown in [8.1].

8.3 Future Research Opportunities

This research focuses on designing high-performance, front-end building blocks, including low-noise amplifiers (LNA) and downconversion mixers, and does not cover the implementation of a complete receiver. Challenges remain in designing a completely reconfigurable, low-cost, multi-band, multi-standard receiver chip, at both the system and circuit levels.

For example, such a receiver would require a highly reconfigurable frequency synthesizer that can be adjusted for different output frequencies, loop bandwidths, and phase noise levels. Designing such a synthesizer with the lowest possible cost in CMOS technologies would be an interesting research topic.

Another interesting topic for research would be the high-level implementation of a complete front-end to improve overall noise, linearity, and selectivity. For example,

the mixer presented in Chapters 6 and 7 exhibits a high level of harmonic conversion gain (from $3f_{LO}$, $5f_{LO}$, etc. down to near DC). This results in high output noise because of noise folding, and very high reciprocal mixing from a blocker at the harmonic frequency bands. In this case, the mixer architecture presented in [8.2] could be utilized to achieve harmonic rejection.

Finally, the front-end circuit presented in Chapter 7 has several tuning mechanisms in both analog and digital. However, all the tuning must be done manually by external control. A research topic on designing a low-cost, multi-band, mixed-signal front-end with digital interface and calibration would make significant contributions to this field of study.

8.4 References

[8.1] A. Behzad, et al., "Direct-conversion CMOS transceiver with automatic frequency control for 802.11a wireless LANs," in *IEEE Int. Solid-State Circuits Conf. Dig. Tech. Papers*, San Francisco, CA, Feb. 2003, pp. 356-499.

[8.2] J. Weldon, et al., "A 1.75-GHz highly integrated narrow-band CMOS transmitter with harmonic-rejection mixers," *IEEE J. Solid-State Circuits*, vol. 36, no. 12, pp. 2003-2015, December 2001.